UNSTABLE SYSTEMS OF VISCOUS AND ELASTIC POLYMER THIN FILMS

UNSTABLE SYSTEMS OF VISCOUS AND ELASTIC POLYMER THIN FILMS

By

JOHN F. NIVEN, B.Sc., M.Sc.

A Thesis
Submitted to the School of Graduate Studies
in Partial Fulfillment of the Requirements
for the Degree
Doctor of Philosophy

McMaster University

DOCTOR OF PHILOSOPHY (2020)
(Physics)

McMaster University
Hamilton, Ontario

TITLE: Unstable systems of viscous and elastic polymer thin films

AUTHOR: John F. Niven, B.Sc., M.Sc. (Dalhousie University)

SUPERVISOR: Dr. Kari Dalnoki-Veress

NUMBER OF PAGES: ix, 111

Abstract

The work presented in this thesis focuses on the study of viscous and elastic polymer thin films in initially unstable configurations. The systems are driven to flow viscously or deform elastically to minimize their free energy. Since these experiments take place on length scales at which gravity does not play a role, the physics is governed purely by surface tension and viscosity in the case of fluid films, or elasticity in the case of rigid films. It is also possible to combine hydrodynamics and elasticity, for example, a viscous film that flows in response to the bending energy of an elastic perturbation, or an elastic film deformed by the capillarity or flow of a fluid.

Viscous flow in thin polymer films is studied in a system which is free-standing in air, meaning it has two fluid-air interfaces. Cylindrical holes are formed part way through a nano-scale polymer film, creating an unstable geometry with dissimilar surface areas at the two interfaces. When heated above its glass transition temperature, surface tension drives the film to flow to minimize its total excess surface area. The evolution is first dominated by fast vertical flow, which equilibrates Laplace pressure through the film by forming symmetric holes at each interface. Slow horizontal flow then becomes dominant, which continually reduces excess surface area by filling in the holes. A novel atomic force microscopy method is developed to monitor the two interfaces of a film as they flow, allowing the total free energy evolution of the system to be measured. The results agree with a hydrodynamic model developed to describe both stages of flow.

Elastic instabilities, where a rigid film deforms in response to geometrical confinement, are studied in a free-standing bilayer system consisting of a thin film on a pre-strained elastic substrate. These instabilities include sinusoidal wrinkling of the capping film, or, since the entire bilayer is free-standing, global buckling, where the entire system deforms out-of-plane. The transition between wrinkling and buckling is found to depend on the thickness and moduli ratios of the films, as well as the pre-strain in the substrate. A simple model shows good agreement with experiments.

Finally, the interaction between elasticity and viscosity is studied by measuring the flow of a viscous fluid perturbation driven by the bending energy of a rigid capping film. The experimental scaling of the perturbation size is in agreement with the theoretical prediction in the large perturbation limit.

Acknowledgements

It feels like yesterday that I decided to leave my home town, move to a new university, and join a new research group. Looking back on all of the friendships and memories I've made in the years since then, I couldn't be happier with my decision. I have several people to thank for helping me get to this point.

The first thanks goes to my parents. My curiosity for the world comes from you. You taught me the value of education, opened countless doors for me, and have supported me unquestionably my entire life. I can never thank you enough for helping me get to where I am today.

The next thanks goes to Kari. Your enthusiasm for science and research was apparent from the moment I met you, and seems to have only grown since then. All of your students are so lucky to be part of a group where the experimental emphasis is on creativity, finding elegant solutions, and most importantly, having fun in the lab. Your remarkable experimental toolbox, physical intuition, and endless optimism continue to amaze me, and occasionally frustrate me when you immediately know how to solve an issue I've been struggling with. I appreciate all of the time we've spent together scheming and problem solving, and especially all of the time you have spent on evenings and weekends thinking about my projects. Your commitment to creating a positive and supportive research environment and your generosity outside of the lab are second to none. Thank you for everything.

A huge thank you to my labmates, current and former. Paul, thank you for all the time you spent teaching me about the lab. JC, thank you for all of the lunches and coffee breaks. Raffi, Adam, Carmen, BDP, Clementine, Lauren, Hamza, and Johnathan, thank you for helping to make being in ABB an enjoyable experience regardless of how my research was going. Never forget how fortunate you are to have been part of such a great group of people.

The final thanks goes to my wife, Katie. Thank you for being my inspiration, my motivation, my rock, and my best friend. You always help to put things into perspective, and I could never have done this without you. I can't wait to see where our journey goes from here.

Contents

Abstract . . . iii

Acknowledgements . . . v

1 Introduction **1**

1.1 Polymers . . . 3

1.1.1 Polymer viscosity . . . 8

1.2 Surface tension . . . 11

1.3 Thin film hydrodynamics . . . 15

1.3.1 Stability of liquid films: wetting and dewetting . . . 22

1.3.2 Rupture of free-standing viscous films . . . 25

1.3.3 Capillary levelling . . . 29

1.3.4 Fluid spreading on a solid surface . . . 31

1.4 Elasticity of solid films . . . 33

1.4.1 Bending versus compression . . . 34

1.4.2 Elastomeric materials . . . 36

1.4.3 Elastocapillarity and elastohydrodynamics . . . 38

1.5 Elastic instabilities . . . 40

1.5.1 Wrinkling . . . 41

1.5.2 High strain instabilities . . . 45

1.5.3 Instabilities in free-standing bilayers . . . 47

2 Experimental techniques **49**

2.1 Creating thin polymer films . . . 49

2.1.1 Materials 49
2.1.2 Spin coating thin films 51
2.2 Sample preparation 53
2.2.1 Creating free-standing holes 53
2.2.2 Controlling tension in thin films 54
2.2.3 Creating polymer fibres 56
2.3 Sample characterization 58
2.3.1 Ellipsometry 58
2.3.2 Optical microscopy 59
2.3.3 Atomic force microscopy 61

3 Papers **65**
3.1 Paper I 66
3.2 Paper II 73
3.3 Paper III 85

4 Conclusions **93**

A Other contributions **97**

Bibliography **98**

List of Figures

1.1 Schematic of a polymer chain 6

1.2 Temperature and molecular weight dependence of polystyrene viscosity 10

1.3 The molecular origins of surface tension and Laplace pressure 12

1.4 Capillary levelling of supported and free-standing films 16

1.5 Horizontal flow profiles with different hydrodynamic boundary conditions 19

1.6 Total and partial wetting of a liquid on a rigid solid 23

1.7 Dewetting of a liquid film off of a rigid solid 24

1.8 The change in surface area by nucleating a hole in a thin film 27

1.9 Capillary levelling of a supported step 30

1.10 Capillary symmetrization and levelling of a free-standing step 31

1.11 Bending and stretching of an elastic sheet 35

1.12 Physically cross-linked elastomers 37

1.13 Wrinkling of a thin rigid film on a soft substrate 42

1.14 Mechanical instabilities of a thin rigid film on a soft substrate 45

1.15 Phase diagram of mechanical instabilities 46

2.1 Schematic sample preparation of a free-standing film with holes . . . 54

2.2 Schematic of a strain stage 55

2.3 Schematic of a fluid fibre capped by a rigid film 57

2.4 Optical microscopy image of a fluid fibre spreading 60

2.5 Schematic of a free-standing AFM measurement 63

Chapter 1

Introduction

Thin polymer films, with thicknesses ranging from tens of nanometers to micrometers, are of scientific interest because of their prevalence in many areas of modern life, including lubricating coatings, adhesives, and electronic devices. Polymers are advantageous for many for these applications because of their highly tuneable chemistry and solution processability [1]. Also, interesting phenomena of fundamental scientific importance can occur when the sample dimensions become comparable to the equilibrium size of the polymer molecules [2], including deviations in glass transition temperature [3, 4], viscosity [5], surface chain mobility [6, 7], and mechanical properties [8] from their bulk values. Since technological applications continue to push for thinner films and coatings, deviations from bulk physical properties could significantly impact the performance of thin polymer films.

Viscous polymer thin films are a useful system for studying flow on length scales at which surface tension dominates gravity, since the viscosity of a polymer melt depends strongly on both the length of the polymer chains and temperature. Well controlled unstable configurations can be created using polymer films in the glassy state, which, when heated above their glassy transition temperature to become a viscous fluid, then flow and evolve to minimize their free energy. Using polymer films allows the flow rate of experiments to be controlled, and even stopped by quenching the film into the glassy state. Fluid polymer films are also non-volatile, and can be viscous enough that they remain stable while free-standing in air for days at a time, allowing experiments to be performed without the influence of a substrate [9].

Elastic instabilities can occur when a thin polymer film is compressed while adhered to a soft substrate. These instabilities create a variety of novel surface topographies, including sinusoidal wrinkling, folding, and ridging, and allow for reversible and tuneable surface patterning. These systems have inspired a variety of potential applications, from optical devices [10, 11], to stretchable solar panels [12], and adhesive films [13]. Elastic instabilities also impact flexible and stretchable electronic devices such as displays and sensors, whose ability to buckle and wrinkle allow them to be better integrated into everyday life [14, 15, 16, 17].

Polymer films are also useful as elastic membranes on length scales at which bending and stretching forces dominate gravity, and where the surface tension or viscous flow pressures of a fluid can cause deformations of the membrane. This interaction between capillarity, viscous forces, and elasticity is relevant to research areas ranging from biological [18] to geophysical [19]. These interactions can also be exploited for applications such as capillary origami [20, 21], lithography [22], and surface patterning [23].

The focus of the work discussed in this thesis is systems involving thin polymer films, both glassy and in the melt, that are in unstable configurations. The systems discussed include unstable fluid films, where the film is driven to flow by surface tension, or mechanical instabilities, where a rigid film deforms in response to geometric confinement. It is also possible to have unstable systems involving both elasticity and viscous flow, such as a fluid perturbation which is driven to flow by the bending energy of a capping elastic sheet. These instabilities are important to understand for thin film applications because they are either to be avoided, or to be exploited to assist in fabrication or improve physical properties.

This is a "sandwich" thesis containing the papers that have been published or submitted during my Ph. D. Each paper is presented with a brief summary in Chapter 3. The introductory chapter presents an overview of the physics of linear polymers and polymeric liquids in Section 1.1. Section 1.2 introduces the basic concepts of surface tension, which are relevant for Paper I. Section 1.3 gives an overview of the hydrodynamics of thin films, with an emphasis on polymeric fluids, relevant for Papers I and II. The impact of hydrodynamic boundary conditions on thin film flow is also discussed. Finally, elasticity is discussed in Section 1.5 in the context of mechanical instabilities that occur in thin films, relevant for Paper III. The details of the sample preparation and characterization techniques used in each experiment are described in Chapter 2, and general conclusions are discussed in Chapter 4.

1.1 Polymers

Polymers are large molecules consisting of hundreds to thousands of covalently bonded repeating structural units, called monomers. Humans have used naturally occurring biopolymers such as natural rubbers for centuries, and synthetic polymers (plastics) are ubiquitous throughout modern life. Many biological materials are also polymeric, including proteins and DNA. Despite the chemical differences between the monomers of different polymers, many polymers have universal physical properties that are characteristic of long, overlapping and interacting chain-like molecules which differ from the properties of simple monomeric liquids and solids. Many of these differences result from the fact that polymer chains cannot pass through themselves or other chains, which limits their motion and causes the chains to become entangled. For sufficiently long chains, these entanglements mean that polymeric liquids, known as polymer melts, are viscoelastic when perturbed, behaving as elastic solids at short times and as viscous liquids at longer times.

By covalently bonding monomers it is also possible to create complex, non-linear polymer architectures, and the type of structure can greatly impact the resulting physical properties of the bulk polymer system. For example, potential polymer architectures include dendritic, where chains split into multiple branches, or ring polymers, where the chain forms a complete loop. It is also possible to bond together chemically distinct monomers or chain segments, creating chains known as heteropolymers, which take on many structural forms. Heteropolymers can show interesting microphase separation behaviour, and have a variety of potential applications [24].

The work presented in this thesis focuses on *linear homopolymers*, meaning that the monomers are attached in a chain with a linear backbone, and that each monomer is chemically equivalent. These chains are characterized by the chemical structure of the monomer and the number of monomers in the chain, known as the degree of polymerization, n. For homopolymers, since each monomer is chemically identical, a chain can be described by its molecular weight, $M = m_0 n$, where m_0 is the molar mass of a constituent monomer.

For synthetic polymers, polymerization techniques produce collections of polymer chains with a distribution of molecular weights, or equivalently, a distribution in chain lengths. Since chain length greatly affects some physical properties of polymers, such as viscosity, it is important to quantify the molecular weight distribution, referred to as the polydispersity, in a given sample. The most common ways to quantify the polydispersity are the number- and weight-average molecular weights, M_n and M_w, two moments of the chain length distribution:

$$M_\mathrm{n} = \frac{\sum_i n_i M_i}{\sum_i n_i} \ , \tag{1.1}$$

$$M_\mathrm{w} = \frac{\sum_i n_i M_i^2}{\sum_i n_i M_i} \ ; \tag{1.2}$$

where n_i is the number of chains in the distribution with mass M_i. The weight-average molar mass is most relevant for quantifying the viscosity of a polymer melt since it emphasizes longer chains [25]. The polydispersity index, or PDI, is defined as the ratio of these two averages: $\mathrm{PDI} = M_\mathrm{w}/M_\mathrm{n}$. Monodisperse samples have a PDI of 1, whereas real samples of synthetic polymers have $\mathrm{PDI} > 1$, with larger values of PDI corresponding to broader chain length distributions. In the samples studied in this thesis, all polymers had $\mathrm{PDI} < 1.06$, which are experimentally considered “monodisperse” or “narrow distribution”.

For polymers in a bulk melt, it is important to know what conformations the chains are most likely to take. The first length scale to define for a linear polymer chain is the total contour length along its backbone: $R_\mathrm{max} = nl\cos(\theta/2)$, where n is the number of subunits, l is the bond length, and θ is the angle between neighbouring bonds, shown schematically in Fig. 1.1(a). For linear polymers with carbon-based backbones, the values of $l = 1.54$ Å and $\theta = 68\,^\circ$ are nearly constant [25].

Consider four neighbouring monomers along the backbone of a carbon-based polymer chain, labeled m_1 to m_4 in Fig. 1.1(a), which are connected by three bonds. The two bonds between first three monomers form a plane, however the final bond can rotate out of the plane by an amount ϕ, known as the torsion angle. Varying ϕ changes the intermonomeric spacing between monomers along the chain, which therefore changes energy and makes certain values of ϕ more probable than others. The lowest energy state, and hence the most probable, is $\phi = 0\,^\circ$, known as the *trans* state, meaning that the bond between m_3 and m_4 remains in the plane of the other bonds. Segments with bonds only in the *trans* state are therefore straight and rigid. The second most probable torsion angles are $\phi = \pm 120\,^\circ$, called the *gauche* states, which result in the third bond being out-of-plane of the others, and causes the chain to effectively be more flexible. The two possible *gauche* configurations are shown in red with dashed bonds in Fig. 1.1(a). In chains of polystyrene (PS) it has been shown that 68 % of bonds are in the *trans* state [26], meaning that the most likely configuration of bonds along the chain is consecutive *trans* bonds, forming a rigid segment, followed by a *gauche* bond which breaks the short-ranged correlation and increases flexibility. For most synthetic polymers there are fewer than 10 *trans* segments in a row, meaning short-ranged correlations die away quickly along the backbone, and overall the chain behaves as an uncorrelated random walk. Now consider a chain in a melt of identical chains. There will be short ranged repulsive interactions between nearby monomers, however a monomer cannot tell if it is interacting with another monomer of the same chain or on a different chain, meaning that a chain in the melt also behaves as a random walk.

For *real* polymer chains, there are short-ranged correlations between the bond angles of near-by monomers because of restricted bond angles and steric hindrance. Chains with large side groups, such as the benzene side groups of PS, sterically hinder bond rotations and therefore result in longer chains than predicted by the ideal chain model. However, flexible linear polymers have many universal physical properties that are independent of the chemical structure of their monomers. This universality allows the monomeric structure of a real chain to be renormalized as an *equivalent* chain with N "effective monomers" of length b, known as the Kuhn length. This renormalization is possible because, as discussed above, short-ranged correlations along the backbone do not change the random walk nature of the overall chain. The Kuhn length can be thought of as the length at which local correlations die away in real polymer chains. This renormalization allows any linear chain to be described as an effective ideal chain, since the chemical specifics of the monomers, such as steric hindrance and local stiffness, are contained within the Kuhn length.

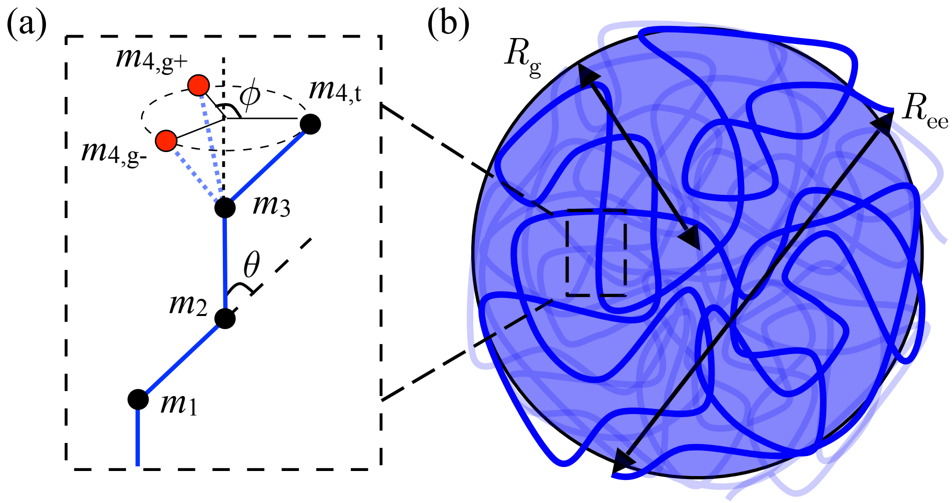

Figure 1.1: (a) Four successive monomers, m_1 to m_4, in a linear polymer chain with bond angle θ and torsion angle ϕ. The first three monomers are in the same plane, but m_4 has three possible positions: the lowest energy *trans* state with $\phi = 0^\circ$, or one of the two *gauche* states (shown in red) with $\phi = \pm 120^\circ$. (b) Schematic of a polystyrene chain in a melt of identical chains, showing the end-to-end distance, R_{ee}, and the radius of gyration, R_{g}.

The equilibrium size of a linear polymer chain can be described by the root mean-square end-to-end distance, defined as the ensemble average distance between the two ends of the chain, which can be written in terms of the Kuhn length as: $\langle R_{\mathrm{ee}}^2 \rangle = Nb^2$, where $\langle\rangle$ denotes the ensemble average [25]. Polystyrene, for example, has a Kuhn length of 18 Å [25].

An alternative length scale used to quantify the size of a polymer molecule of any architecture is its radius of gyration, R_{g}, defined as the root-mean-square distance between each monomer and the centre of mass of the chain. For an ideal linear polymer, the radius of gyration is related to the mean square end-to-end distance by:

$$\langle R_{\mathrm{g}}^2 \rangle = \frac{Nb^2}{6} = \frac{\langle R_{\mathrm{ee}}^2 \rangle}{6} \,. \tag{1.3}$$

Neutron scattering can be used to measure R_{g} for various molecular weights, and for PS it was found that [27]:

$$R_{\mathrm{g}} = \left(2.75 \times 10^{-2}\ \mathrm{nm} \cdot \mathrm{mol/g}\right) \cdot M_{\mathrm{w}}^{1/2} \,. \tag{1.4}$$

For typical samples used in this work $M_{\mathrm{w}} \approx 100 \times 10^3$ g/mol, meaning the chains have $R_{\mathrm{g}} \approx 9$ nm and $R_{\mathrm{ee}} \approx 22$ nm. If the chain length is increased to $M_{\mathrm{w}} \approx 1 \times 10^6$ g/mol, $R_{\mathrm{g}} \approx 28$ nm, which can be comparable to the thickness of a polymer film, meaning the chains are perturbed relative to their equilibrium size in the bulk. This perturbation is referred to as confinement, which, in thin polymer films, has been shown to cause a reduced glass transition temperature [3, 4, 28], decreased viscosity [5], and decreased elastic modulus [8], relative to their bulk values.

For an ideal chain it can be shown that in the limit of long chains the probability distribution of end-to-end vectors is Gaussian [25]:

$$P(\vec{R}_{\mathrm{ee}}, N) = \left(\frac{3}{2\pi N b^2}\right)^{3/2} \exp\left(-\frac{3\vec{R}_{\mathrm{ee}}^2}{2Nb^2}\right) . \tag{1.5}$$

This equation can be used to calculate the multiplicity of an ideal chain, Ω, which then allows the configurational entropy, S, of a chain to be calculated as a function of its elongation distance, $\vec{R}$:

$$S(\vec{R}) = k_{\mathrm{B}} \ln \Omega = -\frac{3k_{\mathrm{B}}\vec{R}^2}{2Nb^2} + C \ , \tag{1.6}$$

where k_{B} is Boltzmann's constant and C is a constant. This result shows that stretching a polymer chain lowers its entropy, since it now has fewer configurational degrees of freedom than in its unperturbed state, thus increasing the free energy by:

$$F_S(\vec{R}) = -TS(\vec{R}) = \frac{3k_{\mathrm{B}}T\vec{R}^2}{2Nb^2} + C \ . \tag{1.7}$$

This means that when a polymer chain is stretched there is an entropic restoring force which resists elongation. Since $F_S(\vec{R})$ is quadratic, the chain behaves like a Hookean spring with restoring force proportional to its elongation. This spring-like response of polymers plays a significant role in the mechanical properties of both viscoelastic melts and elastomeric materials, discussed in Section 1.4.2.

1.1.1 Polymer viscosity

Most polymers are glass formers when cooled from the melt because of the high entropic and enthalpic costs of forming crystalline regions. Polymer glasses have an identical level of order as in the melt, meaning that there is no long-range order, however the two phases differ significantly in that the glass has a finite shear modulus and an effectively infinite viscosity. This means that as a polymer melt is cooled, it eventually undergoes a glass transition, where the molecular motion and relaxation of the chains are slowed, and eventually become longer than experimental time scales. The glass transition is a universal phenomenon observed for a range of glass forming systems, however there is still no universal microscopic theory [7]. The glass transition occurs as a material is cooled below its glass transition temperature, T_g, the temperature at which the reorientations of molecules cannot equilibrate on the time scale at which the material is being cooled. This is a kinetic phase transition, since the measured value of T_g depends on the experimental cooling rate [29]. The glass transition temperature is most commonly measured from either the change in volume at T_g, measured using dilatometry for bulk samples or ellipsometry for thin films, or from the change in heat capacity, measured using calorimetry.

Consider a glass forming material with a characteristic structural relaxation time, τ, at a given temperature. For time scales less than τ there is not sufficient time for structural relaxation to occur, resulting in solid-like behaviour, whereas for $t > \tau$ relaxation can occur and the material is liquid-like. For all glass formers, the relaxation time increases with decreasing temperature, and the universal properties of the glass transition have inspired several theories. One simple model is based on the amount of free volume available for a particle to move in order to reorient and equilibrate [29]. As temperature is lowered, density increases, the amount of available free volume decreases, and the relaxation time increases. However, relaxation is still possible at low free volume if multiple particles move together, known as cooperative rearrangement. Theory and simulations have shown that cooperative rearrangement in glassy materials takes place through string-like motion [7, 30].

Since monomers in an ideal polymer melt are assumed to not interact with other near-by monomers, neighbouring chains are free to pass through one another. In real melts and solutions of long polymers, neighbouring chains impose topological constraints due to the fact that chains do interact, and therefore cannot cross one another. These constraints, known as entanglements, limit chain motion and significantly increase relaxation times. Entanglements greatly affect the viscosity of high M_w polymers and also give rise to the viscoelastic properties of entangled polymer melts at early times, since shortly after shearing a melt, chains will remain entangled, making further shear more difficult [25]. However, at later times the entanglements release and the melt can flow. The Doi-Edwards tube model of entanglements treats a given chain's motion as being restricted to a tube-shaped region formed by the topological constraints imposed by neighbouring chains [31]. Chain motion is unhindered parallel to the contour of the tube, but is restricted perpendicular to the tube because of the entanglements which form the tube. The size of the tube can be described by the number of Kuhn monomers in a strand equal to the tube diameter, N_e, or equivalently, the average molecular weight of the strand, M_e, known as the entanglement molecular weight. For PS, $M_\mathrm{e} = 18.1$ kg/mol, and $N_\mathrm{e} \approx 23$ [25], meaning that a polymer with $M_\mathrm{w} = 183$ kg/mol, such as that used in Paper I has, on average, 11 entanglements per chain in the melt. The reptation model, developed by de Gennes, assumes the chain motion is diffusive along the contour of the tube [32]. The time it takes a chain to diffuse out of its original tube is known as the reptation time, τ_rep. Reptation time is predicted to scale with molecular weight as $\tau_\mathrm{rep} \sim M^3$, which deviates from the experimentally observed scaling of $\tau_\mathrm{rep} \sim M^{3.4}$. This difference is mostly attributed to fluctuations in the length of the confining tube [33]. The value of τ_rep can range from milliseconds to hours depending on molecular weight and temperature while in the melt, and becomes infinite as the temperature approaches T_g.

If a melt of long chains is sheared, for $t < \tau_\mathrm{rep}$ entanglements act as topological constraints, or temporary physical cross-links between chains, and the melt will behave as an elastic solid with a non-zero modulus. For $t > \tau_\mathrm{rep}$ the initial entanglements are relaxed, and the melt will flow with viscosity η. Viscosity is a measure of friction between molecules in a liquid, and for polymer melts η depends strongly on both molecular weight and temperature. The scaling of viscosity with molecular weight changes depending on if the chains are long enough to be entangled, which is determined by a critical molecular weight, $M_\mathrm{c} \approx 2M_\mathrm{e}$ [25]. For unentangled chains

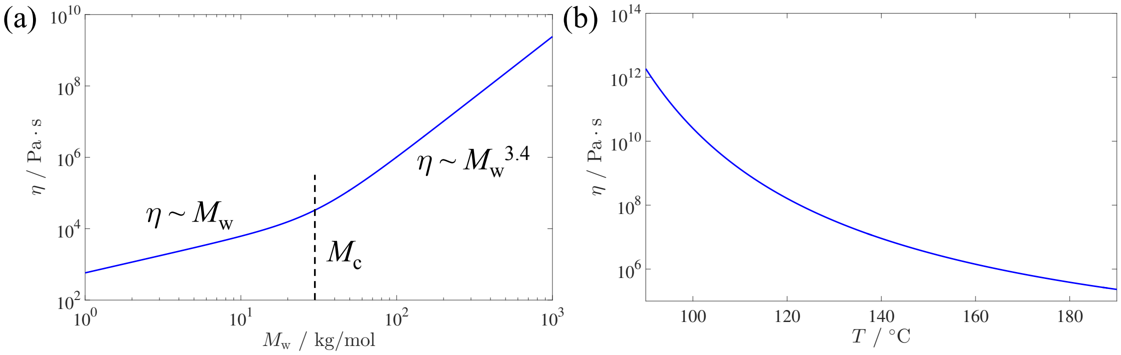

Figure 1.2: (a) The viscosity of polystyrene as a function of molecular weight (Eq. 1.8), showing an increase in viscosity scaling above the critical molecular weight M_c. (b) Polystyrene viscosity as a function of temperature (Eq. 1.9).

below this critical molar weight, $\eta \sim M$, and for entangled chains with $M_w > M_c$, reptation theory predicts that $\eta \sim M_w^3$. As with reptation time, experimentally it is found that $\eta \sim M_w^{3.4}$ [34], with the deviation again attributed to fluctuations in the contour length of the confining tube [33]. An empirical relationship describing the molecular weight dependence of viscosity for linear polymers is given by [34]:

$$\eta \propto M \left[1 + \left(\frac{M}{M_c} \right)^{2.4} \right] . \tag{1.8}$$

A plot of Eq. 1.8 for PS is shown in Fig. 1.2(a), with $M_c = 31.2$ kg/mol [35] and reference viscosity $\eta_0 = 9.1 \times 10^6$ Pa·s at $T_0 = 413$ K for $M_w = 192$ kg/mol [36].

For polymer melts, upon cooling, the glass transition results in a transformation from a viscous liquid to a rigid solid, and therefore the viscosity of a melt of linear polymer chains diverges sharply as the temperature approaches T_g. One of the most used models to describe the divergent temperature dependence of the viscosity of glass formers is the empirical Vogel-Fulcher-Tammann (VFT) equation:

$$\eta(T) = \eta_0 \exp\left(\frac{T_A}{T - T_v} \right) , \tag{1.9}$$

where η_0 is the reference viscosity at T_0, T_A is an activation temperature for chain motion, and T_v is the temperature at which η diverges to infinity. The VFT equation is mathematically equivalent to another viscosity model, the Williams-Landel-Ferry (WLF) equation. A plot of Eq. 1.9 for PS is shown in Fig. 1.2(b), with $T_A = 1250$ K, $T_v = 320$ K [37] and $\eta_0 = 9.1\times10^6$ Pa·s at $T_0 = 413$ K for $M_{\mathrm{w}} = 192$ kg/mol [36]. This plot shows that the viscosity of PS decreases by 6 orders of magnitude within an experimentally accessible temperature range, allowing for flow rate to be controlled in experiments, and completely stopped by quenching below T_{g}.

1.2 Surface tension

We are familiar with examples of surface tension in our every day lives: small insects can walk on the surface of water without sinking; oil droplets in water appear perfectly spherical; and a liquid climbs up the side of a glass to form a meniscus [38]. Surface tension can act as a driving force for fluid flow, and also governs the behaviour of liquids at small length scales, such as the flows discussed in Paper I. All of these examples of surface tension have microscopic origins in the intermolecular interactions between liquid molecules. This section will focus on fluid-fluid surface tension, such as that between a liquid and air, although interfacial tension exists between any two distinct phases.

The amount of work required to increase the surface area of a liquid by an infinitesimal amount dA is $\delta W = \gamma dA$, where γ is the liquid-vapour surface tension [39]. Surface tension can therefore be viewed as the energetic cost per unit area required to increase the area of a liquid interface, with typical units of mJ/m^2. Alternatively, surface tension can be viewed as a force per unit length acting parallel to the interface in the direction that tends to decrease the interfacial area, typically expressed in mN/m. The energy and force descriptions of surface tension are equally valid, and their use depends entirely on which is most convenient for a given problem.

The origins of surface tension are molecular in nature. In the liquid phase, molecules are disordered and experience short-range interactions with their neighbours. For non-polar molecules this interaction arises from van der Waals forces, whereas for water this interaction is primarily from hydrogen bonding. If we consider a liquid of non-polar molecules, short-range interactions occur because the molecules are polarizable, and the instantaneous dipole moments of neighbouring molecules can

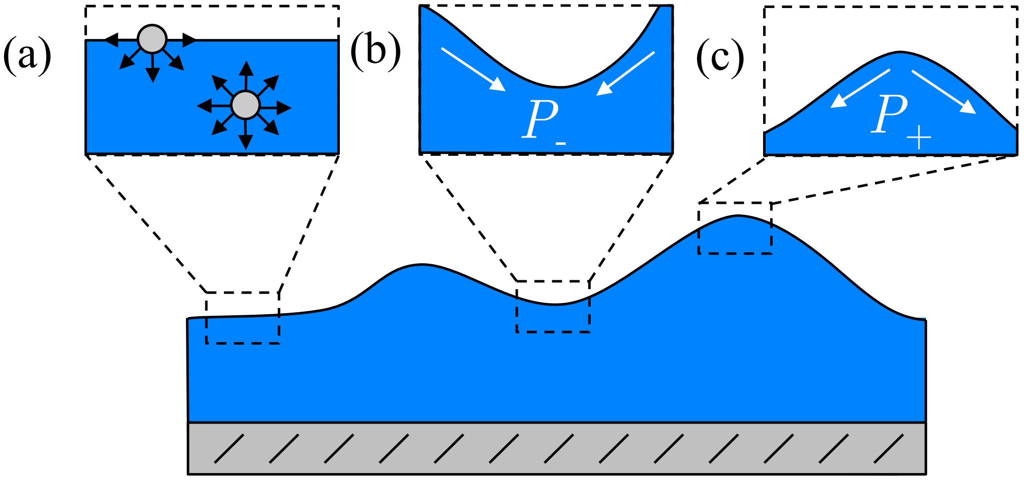

Figure 1.3: Schematic of a fluid film with non-constant curvature. (a) A molecule at the interface has fewer interactions with other molecules, and is therefore at a higher energy state than a liquid molecule in the bulk. The Laplace pressure in a liquid depends on the local curvature at the interface: (b) a region with negative curvature and negative Laplace pressure, and (c) a region of positive curvature and positive Laplace pressure.

attract [40]. This attractive interaction potential varies with the distance between molecules, r, as $U_A(r) \sim -1/r^6$. There is also a separation distance at which the electron clouds of neighbouring molecules begin to overlap, causing electrostatic repulsion. This repulsive interaction potential is often described empirically as $U_R(r) \sim 1/r^{12}$. The combined potential from these attractive and repulsive interactions results in a potential well of depth U_0, with the typical separation distance between two molecules in the liquid, r_0, at the minimum of the well. This means that molecules in a bulk liquid have, on average, U_0 potential energy per molecule binding them to neighbouring liquid molecules. Contrast this to a molecule at the liquid-vapour interface, shown schematically in Fig. 1.3(a), which has roughly half as many interactions with other liquid molecules on average in comparison with a molecule in the bulk, meaning that it is in a state with $\sim U_0/2$ higher energy. This excess free energy for molecules at the interface relative to the bulk is the origin of surface tension, and what drives a liquid to flow in order to minimize its excess surface area, thereby minimizing its excess surface energy, such as a spherical liquid droplet in air. This same argument holds for creating interface between two immiscible liquids, such as oil in water.

Molecular organic liquids like ethanol and acetone have liquid-vapour surface tensions of ∼20 mJ/m^2, whereas for water, with its strong hydrogen bonds, $\gamma = 72$ mJ/m^2. For polymeric liquids, surface tension depends on the chemical nature of the monomers, temperature, and molecular weight [41]. For most polymers the dependence of surface tension on temperature is well described empirically for experimentally relevant temperatures as [42]:

$$\gamma(T) = \gamma_0 + \frac{d\gamma}{dT} \cdot T \ , \tag{1.10}$$

where $\gamma_0 = \gamma(T = 0\,^\circ\mathrm{C})$ and $d\gamma/dT$ are constant for a given polymer [43]. For PS, $\gamma(T = 0\,^\circ\mathrm{C}) = 41.5$ mJ/m^2 and $d\gamma/dT =$ -0.068 mJ/(m$^2\cdot{}^\circ$C) [43]. This reduction in surface tension with increasing temperature results from weaker cohesion between molecules at higher temperatures. As will be shown in Section 1.3.3, the rate of viscous flow on small length scales is often quantified by the ratio of a liquid's surface tension and viscosity, γ/η, known as the capillary velocity. Using Eq. 1.10 for PS, an increase in temperature from 110 °C to 150 °C will decrease γ by 10 %. This change has negligible affect on the capillary velocity in comparison to the change in viscosity over the same temperature range (Eq. 1.9), which decreases by a factor of $\sim 3\times10^4$.

For polymeric liquids there is also an entropic contribution to surface tension that is dependent on molecular weight [41, 42]. This entropic contribution is dominated by the available free volume for chain segments. For the high molecular weight chains used in this thesis, the free volume changes with molecular weight because the density of chain ends changes. The molecular weight dependence of surface tension is well described by the functional form:

$$\gamma(M_\mathrm{n}) = \gamma_\infty \left(1 - \frac{K}{M_\mathrm{n}^\alpha}\right) \ , \tag{1.11}$$

where K is a constant for a given polymer, γ_∞ is the surface tension for infinite M_n, and $\alpha = 1$ for high molecular weights, or $\alpha = 2/3$ for low molecular weights [44]. For the molecular weight range typically used in experiments, $15 < M_\mathrm{n} < 1000$ kg/mol, γ changes by ∼3 %, while viscosity changes as $M_\mathrm{w}^{3.4}$, which again will clearly dominate the change in γ.

The surface tension of a thin liquid film, either supported or free-standing in air, is modified from its bulk value when the film's thickness becomes comparable to the length scale of molecular interactions. The amount by which γ is modified is called the effective interface potential, Φ, and its value depends on the type of fluid, the surface it is interacting with, and the thickness of the film. Consider two parallel infinite planar surfaces that are brought together to a separation distance d. If the materials only interact through van der Waals forces, there is a net attraction between the molecules of the two surfaces. The effective interface potential is the free energy of this interaction per unit area, given by [40]:

$$\Phi = \frac{-A}{12\pi d^2} \ , \tag{1.12}$$

where A is the Hamaker constant, which depends on the refractive indices of the two materials. For PS and silicon, $A = -2.2 \times 10^{19}$ J [45], whereas for PS and air, $A = 6.5 \times 10^{-20}$ J [40]. A negative value of A means a thin film will remain stable, whereas a positive value of A means the film is unstable [45]. The sign of A changes for silicon if there is an oxide layer present, meaning that films on oxidized silicon are unstable. It can be shown that the presence of the effective interface potential causes a pressure within the liquid, $P(x, y) = \Phi'(h(x, y))$, known as the disjoining pressure. As will be discussed in Section 1.3, the value and shape of $\Phi(h)$ are critical for determining the stability of thin fluid films against rupture.

For any curved liquid interface there is a pressure difference between the inside and outside of the liquid, known as the Laplace pressure. Consider the work, δW, required for an infinitesimal change in the radius, dR, of a spherical drop of liquid with volume V and surface tension γ [39]:

$$\delta W = -P_{\mathrm{o}} dV_{\mathrm{o}} - P_{\mathrm{i}} dV_{\mathrm{i}} + \gamma dA \ , \tag{1.13}$$

where subscripts 'i' and 'o' denote the inside and outside of the drop, respectively. The last term represents the energetic cost to increase the surface area of the drop. Since volume is conserved $dV_{\mathrm{o}} = -dV_{\mathrm{i}}$, and for a sphere $dV = 4\pi R^2 dR$ and $dA = 8\pi R dR$, the Laplace pressure change across the interface is found when $\delta W = 0$:

$$\Delta P = P_\mathrm{i} - P_\mathrm{o} = \frac{2\gamma}{R} \ . \tag{1.14}$$

This increased pressure in the droplet relative to its surroundings occurs to balance the net internal force of surface tension. The value of R can be interpreted as the radius of curvature of the interface. For a generalized interface between two fluids, A and B, with two principal radii of curvature, R_1 and R_2, the Laplace pressure is:

$$\Delta P = \gamma_\mathrm{AB}\left(R_1^{-1} + R_2^{-1}\right) = 2\gamma_\mathrm{AB} C \ , \tag{1.15}$$

where γ_AB is the interfacial tension between the two fluids and C is the mean curvature of the interface. For an interface whose topography is only dependent on x, such as that shown schematically in Fig. 1.3, and for the capillary levelling of a step discussed in Section 1.3.3, the mean curvature is given by [39]:

$$R^{-1} = \left| \frac{\partial_x^2 h}{\left[1 + (\partial_x h)^2\right]^{3/2}} \right| \ . \tag{1.16}$$

Since the denominator is always positive, regions that are concave up, such as Fig. 1.3(b), have lower pressure than regions that are concave down, such as Fig. 1.3(c). This means that an interface with a curvature gradient will also have a pressure gradient, which drives the fluid to flow from regions of positive pressure (positive curvature) to regions of negative pressure (negative curvature), with flow directions represented schematically by white arrows in Fig. 1.3. The net result is that surface tension will drive a fluid film with a non-uniform topography to evolve toward a flat film, thus reducing its excess surface energy with time.

1.3 Thin film hydrodynamics

This section builds on the previous to briefly describe how viscous fluids flow at small length scales, including the equations and physical assumptions required to derive the velocity profiles for thin viscous fluid films with initially non-uniform surface topographies. The focus will be on polymeric films with thickness on the order of hundreds of nanometers, although the results are applicable to any thin viscous film.

The derivation will be done for both films on solid substrates (Fig. 1.4(a)) or films that are "free-standing" in air, with two fluid-air interfaces (Fig. 1.4(b)) by changing the hydrodynamic boundary conditions. For a more detailed derivation see Refs. [39, 46, 47].

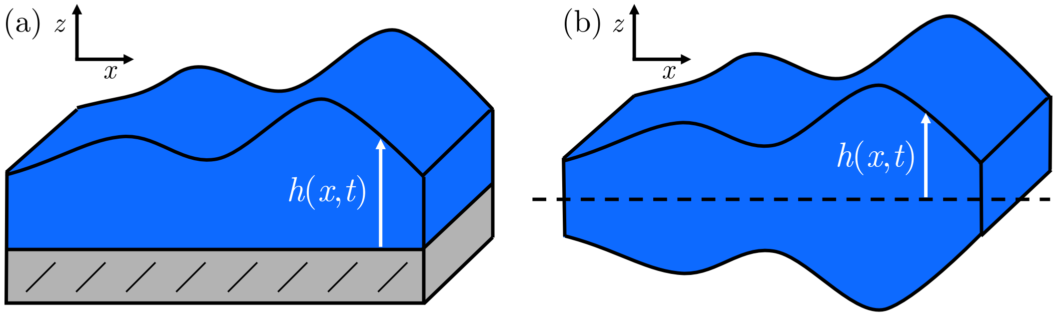

Figure 1.4: (a) A fluid film with a non-uniform surface topography on a solid substrate. (b) A free-standing film with interfaces that are symmetric about the mid-plane to equilibrate Laplace pressure through the film.

The dynamics of a rigid body, in which the entire object moves as a whole, are described by Newton's second law, which states that the vector sum of all forces acting on the object is equal to its mass multiplied by its acceleration, $\vec{F} = m\vec{a}$. Liquids are inherently not rigid bodies, since the small volume elements of a liquid are free to move independently of each other. The fundamental equation for the dynamics of a liquid is therefore:

$$\vec{F} = \rho \frac{d\vec{v}}{dt} \ , \tag{1.17}$$

where ρ is the fluid density, $\vec{v}$ is the velocity vector of a volume element, and $\vec{F}$ is the net force acting on the volume element [39]. Assuming the fluid is incompressible, there is the added constraint $\nabla \cdot \vec{v} = 0$. Equation 1.17 essentially describes a balance between the forces that drive flow, such as gravity and surface tension, and the force that opposes flow, viscosity. These driving forces manifest as pressure gradients in the fluid, either hydrostatic pressure or Laplace pressure, which drive flow from regions of high pressure towards regions of low pressure. The full form of Eq. 1.17 in three dimensions is known as the Navier-Stokes equation [39, 46]:

$$\rho\left(\frac{\partial\vec{v}}{\partial t}+\vec{v}\cdot\vec{\nabla}\vec{v}\right)=-\vec{\nabla}P+\eta\nabla^2\vec{v}+\rho g\ , \tag{1.18}$$

where P is the fluid pressure, $\vec{v}=(v_x,v_y,v_z)$ is the flow velocity and v_x, v_y, and v_z are the components of the velocity field in the $x-$, $y-$, and $z-$directions, respectively. This equation represents the conservation of momentum per unit volume of a liquid volume element. The left hand side is the temporal derivative of momentum per unit volume (the inertial component) and the right hand side is the sum of driving and mediating forces per unit volume. Solutions to this equation fully describe the flow field at any time and place within the fluid, however multiple assumptions and simplifications are required to produce analytical solutions.

First, it is necessary to understand which driving and mediating forces dominate at a given length scale in order to simplify the Navier-Stokes equations. The Bond number, Bo, gives the relative magnitude (per unit volume) of gravity and surface tension forces:

$$\mathrm{Bo}=\frac{\text{gravity}}{\text{surface tension}}=\frac{\rho g}{\gamma l/V}=\frac{\rho g l^2}{\gamma}\ . \tag{1.19}$$

The gravitational force is equal to the force of surface tension at a characteristic length scale, l_c, known as the capillary length:

$$l_\mathrm{c}=\sqrt{\frac{\gamma}{\rho g}}\ . \tag{1.20}$$

On length scales well below the capillary length gravity can be neglected relative to surface tension. For pure water, with $\gamma = 72$ mN/m and $\rho = 1$ g/cm^3, $l_\mathrm{c}\approx 3$ mm, comparable to the size of raindrops on a window, since gravity causes larger drops to slide down the glass. For a polymeric fluid such as PS, with $\gamma = 35$ mN/m and $\rho = 1$ g/cm^3, $l_\mathrm{c}\approx 2$ mm. This result shows that for experiments involving films of fluid polymer with thickness less than a micrometer, surface tension is the dominant driving force and gravity can be safely neglected. This simplification applies to experiments discussed in Paper I and Paper II, since the samples have vertical length scales between 100s of nanometers to micrometers.

The next simplification that can be made for viscous liquids involves the inertial term, the left side of Eq. 1.26. The Reynolds number, Re, gives the relative contribution (per unit volume) of inertial and viscous forces:

$$\mathrm{Re} = \frac{\text{inertial}}{\text{viscous}} = \frac{\rho l v}{\eta} = \frac{\rho l \gamma}{\eta^2} \ , \tag{1.21}$$

where l is a typical length scale of the flow, and $v = \gamma/\eta$ is the capillary velocity. For $\mathrm{Re} \gg 1$, flow is dominated by inertia, whereas for $\mathrm{Re} \ll 1$, flow will be dominated by viscosity. If $\mathrm{Re} = 1$, $l_{\mathrm{Re}} = \eta^2/\rho\gamma$ is the length scale below which viscous forces dominate inertia, and for flow on length scales well below l_{Re}, the inertial component of Eq. 1.18 can be safely neglected, greatly simplifying the equations. For PS, with $\eta \approx 1$ MPa/s, $l_{\mathrm{Re}} \approx 2 \times 10^{10}$ m, a length greater than the diameter of the sun, meaning that inertia can always be safely neglected for experiments involving high M_{w} polymeric liquids. Therefore, for thin films of liquid polymer, flow is driven by surface tension and mediated by the film's viscosity. This allows Eq. 1.18 to be simplified by removing the inertial term and the force of gravity, resulting in:

$$\nabla P + \eta \nabla^2 \vec{v} = 0 \ . \tag{1.22}$$

These are known as Stokes equations, and describe slow, viscous flow in thin films. Stokes equations are the basis of the hydrodynamic theory presented in Paper I.

The goal is now to use these equations to calculate the flow profile in the film, $\vec{v}$, however further simplifications are still required. We will assume the geometry of the film is invariant in y (see Fig. 1.4), meaning that $v_y = 0$, and all derivatives in y equal 0. We will also use the lubrication approximation, which assumes the horizontal length scales of the film (x-direction) are much larger than the thickness (z-direction), meaning that vertical flows are negligible in comparison to horizontal flows: $v_x \gg v_y$. Using these assumptions, Stokes equations simplify to:

$$-\frac{\partial P}{\partial x} + \eta \left(\frac{\partial^2 v_x}{\partial z^2} \right) = 0 \ . \tag{1.23}$$

We now need to consider the relevant hydrodynamic boundary conditions. For a film on a solid substrate, Fig. 1.4(a), there is a fluid-air interface at $z = h$ and a fluid-solid interface at $z = 0$. For a viscous fluid in air there is a *no-shear* boundary condition at the fluid-air interface: $\partial_z v_x|_{z=h} = 0$. This is because air, with its extremely low viscosity, cannot support a shear stress, $\eta\partial_z v_x$, at the interface. Therefore, in order for shear stress to be continuous across the interface it is required that for the fluid $\partial_z v_x|_{z=h} = 0$, meaning that the velocity profile is maximal at the fluid-air interface. If there is a strong attraction between the fluid and substrate, the fluid will remain stationary at the fluid-solid interface: $v_x(z = 0) = 0$. This is called a *no-slip* boundary, shown in Fig. 1.5(a). This no-slip condition applies to polymer fluids on bare silicon substrates, for example. Weaker attraction between the fluid and solid may allow the fluid to "slip" across the fluid-solid interface, shown in Fig. 1.5(b). The degree of slip is characterized by the slip length, b, defined as the length below the fluid-solid interface at which the tangent of $v_x(z = 0)$ extrapolates to zero: $b = [v_x/\partial_z v_x]_{z=0}$. Interfaces with a slip length less than the film thickness are referred to as "weak-slip", for example PS on Teflon flouropolymer coated silicon which has $b \approx 100$ nm [48]. The limit of $b \to \infty$ is known as "full-slip", shown in Fig. 1.5(c). Full-slip applies to flow in free-standing films, which have two fluid-air interfaces [9], such as the samples discussed in experiment in Paper I.

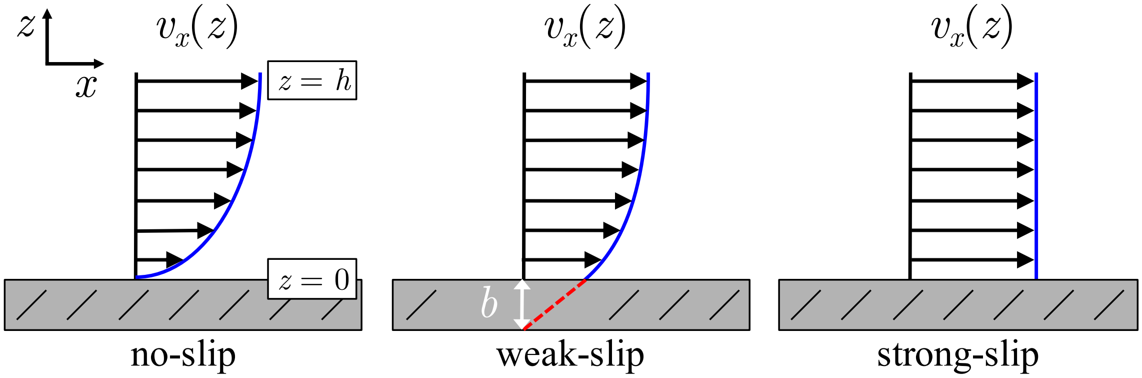

Figure 1.5: Fluid-solid hydrodynamic boundary conditions for flow on a solid substrate with a no-shear boundary condition at the fluid-air interface ($z = h$). From left to right: no-slip, resulting in Poiseuille flow; weak slip, where fluid can slip along the interface with slip length b; and strong slip ($b \to \infty$), resulting in Plug flow.

First consider a thin fluid film on a solid substrate with a no-slip boundary at the fluid-solid interface and a no-shear boundary at the fluid-air interface, shown schematically in Fig. 1.4(a). Integrating Eq. 1.23 once with respect to z and using the relevant boundary conditions gives the horizontal velocity profile:

$$v_x(z) = \frac{1}{2\eta}\frac{\partial P}{\partial x}\left(z^2 - 2zh\right) . \tag{1.24}$$

The velocity profile is parabolic in z because of the boundary conditions imposed by the interfaces, and is referred to as Poiseuille flow.

The pressure driving flow is the Laplace pressure, which comes from curvature gradients at the interface, as discussed in Section 1.2. For thin polymer films, we can simplify further by assuming small gradients in height at the interface ($\partial_x h \ll 1$), meaning that the curvature (Eq. 1.16) simplifies to $R^{-1} \approx -\partial_x^2 h$, and the resulting Laplace pressure is $P = -\gamma \partial_x^2 h$. We can now define the flow rate, Q, as the amount of fluid flowing through a cross-section of the film per unit time: $Q = \int_0^h v(z)dz$. Using conservation of volume:

$$\frac{\partial h}{\partial t} = -\frac{\partial Q}{\partial x} . \tag{1.25}$$

By integrating the flow rate through the thickness of the film we obtain the thin film equation for a 2-dimensional (2D) film on a supported substrate:

$$\frac{\partial h}{\partial t} + \frac{\gamma}{3\eta}\left(\frac{\partial}{\partial x}\left(h^3 \frac{\partial^3 h}{\partial x^3}\right)\right) = 0 . \tag{1.26}$$

This equation describes the flow of a thin viscous fluid film driven by surface tension and mediated by viscosity. This result is only valid for thin films with small height gradients because of the lubrication approximation. The 2D thin film equation has solutions $h(x,t)$ which are self-similar in $x/t^{1/4}$. Self-similarity means that the surface profile at time t_1 can be stretched horizontally to match the profile at a later time t_2: $h\left(x/t_1^{1/4}, t_1\right) = h\left(x/t_2^{1/4}, t_2\right)$. This means that comparisons between numerical solutions to Eq. 1.26 and experimental profiles allow the capillary velocity of the fluid, γ/η, to be extracted, as discussed further in Section 1.3.3.

Now if we consider flow in a 2D free-standing film of thickness $2h$ which has two fluid-air interfaces, shown schematically in Fig. 1.4(b), the hydrodynamic boundary conditions of the problem change and so does the resulting flow profile. The film is assumed to be thick enough such that disjoining pressure can be neglected, but thin enough that the lubrication approximation is valid. Returning to Eq. 1.23, we now have no-shear boundary conditions at the two fluid-air interfaces:

$$\frac{\partial v_x}{\partial z} = 0\,,\ \text{at}\, z\ =\ \pm\, h(x,t)\ . \tag{1.27}$$

Integrating Eq. 1.23 with respect to x gives

$$\eta \frac{\partial \vec{v}}{\partial x} = -\gamma \frac{\partial^2 h}{\partial x^2}\ , \tag{1.28}$$

and integrating again gives the horizontal velocity profile:

$$v_x = -\frac{\gamma}{\eta}\frac{\partial h}{\partial x}\ . \tag{1.29}$$

As was done in the supported case, this velocity can be integrated to find the fluid flux, and with conservation of volume yields the free-standing thin film equation:

$$\frac{\partial h}{\partial t} = \frac{\gamma}{\eta}\frac{\partial}{\partial x}\left(h\frac{\partial h}{\partial x}\right)\ . \tag{1.30}$$

This equation also has self-similar solutions, this time in the variable $x/t^{1/2}$. This self-similar behaviour was confirmed experimentally by studying flow in thin free-standing polymer films, discussed further in Section 1.3.3 [9]. For free-standing films, there is the added requirement that the Laplace pressure is balanced at the two fluid-air interfaces. This means that a free-standing film with significantly different curvatures at its two interface will flow vertically to equilibrate pressures, resulting in a film which is symmetric about its mid-plane, as shown in Fig. 1.4(b). This effect was observed experimentally for free-standing liquid polymer films with an initially sharp step at one interface [9].

1.3.1 Stability of liquid films: wetting and dewetting

When a liquid droplet is placed on a solid surface, it can either take the form of a spherical cap-shaped droplet, such as water on plastic, or spread horizontally and "wet" the surface, such as water on glass [39]. Alternatively, a thin liquid film on a surface can either retain a uniform thickness or "dewet" from the surface and break up into droplets. Wetting and dewetting are of significant importance to a variety of applications such as paints, inks, waterproof textiles, thin film surface coatings, as well as in biological systems [39]. The stability of a thin film is governed by the interaction between the fluid and substrate and the thickness of the film. Having an understanding of the parameters that control wetting allows a surface to be physically or chemically modified to tailor wetting properties. The following section will briefly discuss the stability of thin viscous liquid films, for which gravity and inertia can be ignored, either on solid substrates or free-standing, and the dynamics of a viscous liquid spreading on a solid surface. For more information the reader is referred to Refs. [39, 49, 50].

Wetting refers to the way in which a liquid spreads or recedes when placed on a solid surface or an immiscible liquid [39, 49]. Wetting behaviour can be separated into two main categories: total wetting, where the liquid spreads across the solid to maximize the amount of solid-liquid interface; or partial wetting, where the liquid forms a spherical cap, characterized by the equilibrium contact angle θ_e at the liquid-solid-vapour triple line, referred to as the contact line. These two types of wetting are shown schematically in Fig. 1.6. As discussed previously, surface tension can be considered a force per unit length, so for a droplet in mechanical equilibrium with a rigid solid, the static contact angle can be calculated using a horizontal force balance at the contact line. Since there are three phases present, three surface tensions need to be considered, resulting in [39]:

$$\gamma \cos\theta_\mathrm{e} = \gamma_\mathrm{sv} - \gamma_\mathrm{sl} \ , \tag{1.31}$$

where γ_sv, γ_sl, and γ are the solid-vapour, solid-liquid, and liquid-vapour interfacial tensions, respectively. This equation is known as the Young-Dupré law, and is only valid when the solid is undeformed by the vertical component of γ. In the case of a soft solid, such as the elastomers discussed in Section 1.4.2, this assumption no longer holds, and the vertical force balance between capillarity and the elasticity of the solid must also considered. This is known as elastocapillarity, and the capillary force can be large enough to deform the solid, creating a “capillary ridge”. Elastocapillarity is discussed further in Section 1.4.3.

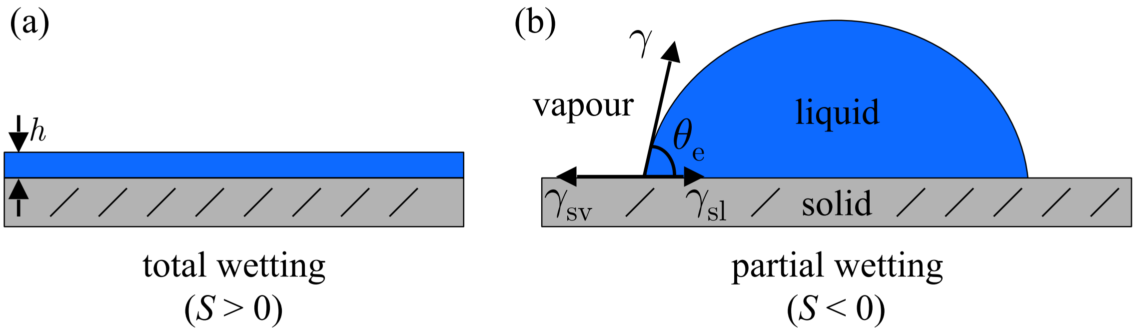

Figure 1.6: Wetting of a liquid on a rigid solid substrate: (a) total wetting, in which the liquid spreads across the substrate and retains an equilibrium height h, and (b) partial wetting, where the liquid forms a droplet with the shape of a spherical cap, characterized by the equilibrium contact angle θ_{e}.

To distinguish between these two forms of wetting we define the spreading parameter, S, which is the difference between the surface energy per unit area of the substrate before and after it is wet by the liquid [39]:

$$S = E_{\mathrm{dry}} - E_{\mathrm{wet}} = \gamma_{\mathrm{sv}} - (\gamma_{\mathrm{sl}} + \gamma)\,. \tag{1.32}$$

If $S > 0$, the surface energy of the dry solid is greater than that of the wetted solid, meaning that the liquid will spontaneously spread to cover the surface, leading to total wetting (Fig. 1.6(a)). This results in a thin liquid film, meaning that there is no solid-liquid contact line, and therefore the equilibrium contact angle, θ_{e}, is zero. Alternatively, when $S < 0$, it is energetically favourable for the liquid to dewet from the surface, eventually forming droplets with equilibrium contact angle $\theta_{\mathrm{e}} > 0$, (Fig. 1.6(b)), known as partial wetting. These droplets have the shape of a spherical cap in order to maintain constant curvature, and therefore constant Laplace pressure, at the liquid-vapour interface. In the partial wetting regime the droplet is also surrounded by a nanoscopically thin film, known as a precursor film, which is discussed further in Section 1.3.4.

If a fluid film of uniform thickness is formed on a solid surface for which $S < 0$, below a critical thickness, h_c, the film will break up and form droplets and expose dry solid-vapour interface in order to minimize surface energy. The critical film thickness is governed by the fluid's capillary length and its equilibrium contact angle. This process is known as dewetting, and is a special case of fluid film rupture. Although often avoided in applications, dewetting can be a useful tool for removing dust particles while drying a surface, or for measuring various flow properties on small length scales [39]. Thin fluid films can be either metastable or unstable depending on their initial thickness, the thickness dependence of their effective interface potential (Eq. 1.12), $\Phi(h)$, and the presence of defect sites. For an ultra-thin ($h \lesssim 10$ nm) PS film on a silicon oxide substrate, for example, long-range interactions between the film and substrate become significant. It can be shown that a film with an initially uniform thickness can lower its free energy by creating thin and thick regions, thus causing the film to spontaneously dewet, even in the absence of defects [51]. This process is called spinodal dewetting, and results in droplets which form on a characteristic time scale and length scale throughout the film. Thicker PS films are metastable, and spinodal dewetting does not occur. However, since it is still energetically favourable to form thinner regions, dewetting of thick films can still occur by nucleation and growth of dry regions on impurities such as dust particles or surface defects, or through thermal fluctuations in the film's thickness [51]. These nucleation sites allow the free energy barrier set by the effective interface potential to be overcome.

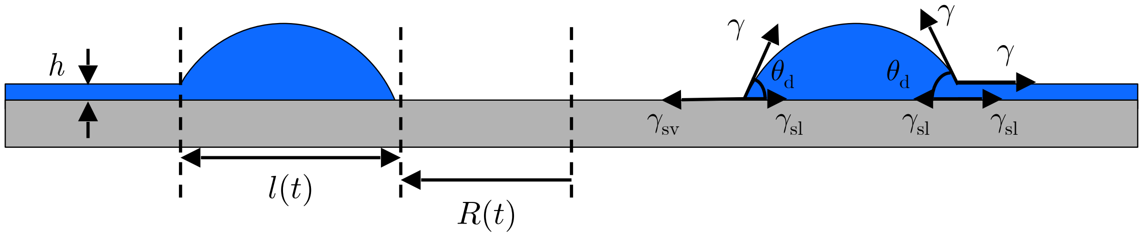

Figure 1.7: Schematic side-view snapshot of the dewetting of a thin viscous liquid on a rigid solid surface at an intermediate time point.

A schematic side profile of a thin viscous film during nucleated dewetting is shown in Fig. 1.7, where $R(t)$ is the radius of the dewet hole at time t, $l(t)$ is the width of the dewetting ridge, and θ_d is the dynamic contact angle. The dewetting ridge forms surrounding the hole in order to collect excess fluid from the now dry region. The rim has a circular cross-section because Laplace pressure requires that the rim has constant curvature, meaning that the two dynamic contact angles of the ridge are roughly equal. The dynamics of dewetting can be modelled by considering the driving and mediating forces acting on the rim, and are discussed in detail in Refs. [49] and [50]. The driving force for dewetting is given by the sum of the interfacial tensions acting on the rim, which are constant with time, and points radially outward from the centre of the hole. In order for the hole to grow there must be a non-zero driving force, and therefore it is required that $\theta_\mathrm{d} < \theta_\mathrm{e}$. For viscous dewetting this driving force is balanced by viscous dissipation in the region of the contact line, which is proportional to the rim velocity. Balancing the driving and mediating forces and assuming conservation of volume gives a hole growth speed, v, of:

$$v \propto \frac{\gamma\theta_\mathrm{e}^3}{\eta} \ . \tag{1.33}$$

This result is well supported by experiments [52], and shows that for viscous dewetting on a solid surface the radius of a hole growths linearly with time.

1.3.2 Rupture of free-standing viscous films

Analogous to the dewetting of liquid films on solid surfaces, free-standing viscous liquid films with two liquid-air interfaces are prone to form holes throughout the thickness of the film, and subsequently rupture. However, the addition of a second no-shear boundary means that the physics of free-standing rupture differs from that of supported dewetting. For high Reynold's number films such as soap bubbles, the rate of change in surface energy is balanced by the rate of change in inertial kinetic energy, resulting in a linear growth of the hole's radius, R, with time: $R(t) \sim t$ [53, 54]. For low Reynold's number hole growth, such as the polymer films discussed in Paper I, the rate of change of surface energy is balanced by viscous dissipation. This results in exponential growth: $R(t) = R_0 \exp(t/\tau)$, where τ is a characteristic growth time. This exponential behaviour has been confirmed by a variety of experiments [55, 56, 57].

As with supported dewetting, there are two possible mechanisms for creating holes in a free-standing viscous thin film: spontaneously, in a process analogous to spinodal dewetting, or by nucleation on impurities in the film [57]. In the case of spontaneous rupture, thermal fluctuations at the interface can be amplified by attractive dispersion interactions through the film [58]. For defect-free films there is a critical length scale, λ_c, corresponding to the fastest growing amplitude, meaning that all of the holes form on a similar time scale and with the same average spacing throughout the film. The growth rate and length scale of spontaneous hole formation can be calculated for a free-standing film with initially sinusoidal surface undulations using Stokes equations and by balancing the Laplace pressure and disjoining pressure at the surface [40]. The critical length scale is [59]:

$$q_\mathrm{c} = \frac{2\pi}{\lambda_\mathrm{c}} > \sqrt{\frac{A}{\pi\gamma h_0^4}} \ , \tag{1.34}$$

where A is the Hamaker constant of the fluid in air. For PS in air $A = 6.5 \times 10^{-20}$ J [40]. Perturbations with length scales larger than λ_c are unstable, and will grow with time, with the time scale of the fastest growing mode given by:

$$\tau_\mathrm{min} \approx \frac{\eta h_0^3}{A} \ , \tag{1.35}$$

where η is the fluid viscosity. For the material parameters of the polymer used in Paper I: M_w = 183 kg/mol, T = 130 °C, $\eta \sim 10^9$ Pa·s, h_0 = 80 nm, which gives $\tau_\mathrm{min} = 10^8$ s, orders of magnitude larger than the experimentally observed time scale of hole nucleation, which is typically on the order of seconds to minutes (see Paper I, for example). This result shows that experimental hole formation in these films is driven by nucleation on defects instead of spontaneous formation due to thermal fluctuations.

For the nucleation and growth mechanism there is an energy barrier due to the creation of excess surface area upon the formation of a hole. Consider a hole of radius R nucleated in a film of thickness h with liquid-air surface tension γ, shown schematically in Fig. 1.8. The total liquid-air surface area lost at the two interfaces (top and bottom) is $A_{\mathrm{lost}} = 2 \times \pi R^2$ (Fig. 1.8(a)), and the liquid-air surface area created is $A_{\mathrm{gained}} = 2\pi Rh$ (Fig. 1.8(b)). The change in surface energy by nucleating a hole is therefore:

$$\Delta E = \gamma \left(A_{\mathrm{gained}} - A_{\mathrm{lost}}\right) = \gamma \left(2\pi Rh - 2\pi R^2\right) . \tag{1.36}$$

This is the energy barrier required to nucleate a hole in a free-standing film. There is a critical hole size, R_{c}, required to be nucleated in order for growth to occur, which can be found by minimizing the nucleation energy with respect to R:

$$\begin{aligned} \frac{\partial \Delta E}{\partial R} &= 2\pi\gamma \left(h - 2R\right) = 0 , & (1.37) \\ \Rightarrow R_{\mathrm{c}} &= h/2 . & (1.38) \end{aligned}$$

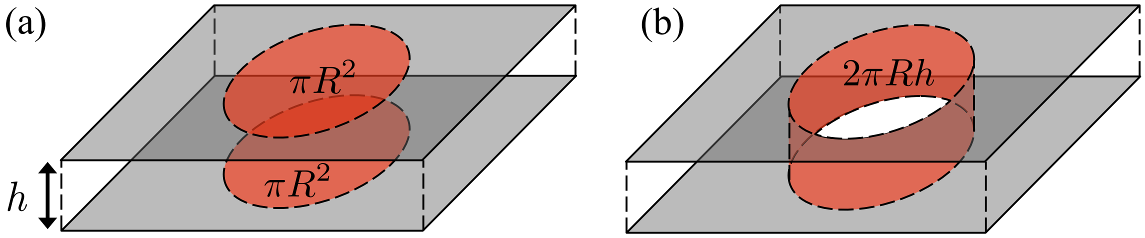

Figure 1.8: The change in surface area (and therefore surface energy) by nucleating a hole in a thin film: (a) in red is the initial surface area before nucleating a hole, and (b) in red is the surface area after nucleating a hole. Adapted from Ref. [60].

The energy required to overcome the nucleation barrier comes from defect sites such as small dust particles or solvent impurities ($\sim 0.2\,\mu$m) [56, 57]. It has also been suggested that air pockets in films could cause density inhomogeneities which could nucleate holes [45].

After a hole is nucleated, it will continue to grow because surface tension creates a force acting radially outward at the contact line around the rim of the hole at both interfaces. The net force acting on the edge of the hole is therefore $2 \cdot \gamma 2\pi R$, which acts on the inside of the hole with an area of $2\pi R \cdot h$. This results in a constant stress of $\sigma = 2\gamma/h$ acting on the hole. By considering a fluid element near the edge of the hole it can be shown that the shear strain rate is $\dot{\gamma} = 2\dot{R}/R$, where $\dot{R} = dR/dt$. The fluid-air interfaces cannot support a shear stress, and therefore there is full slip of the fluid at the surfaces, leading to a constant velocity profile across the thickness of the film as the hole grows (plug flow, Fig. 1.5(c)). This results in radial flow whose magnitude depends only on the radial distance from the centre of the hole, r:

$$v(r) = \frac{\dot{R}R}{r} \ . \tag{1.39}$$

The growth rate of a hole in a low Reynolds number film can be calculated by balancing the viscous dissipation rate with the rate at which surface energy is gained. For a film with viscosity η and thickness h, the viscous dissipation rate for plug flow is [55]:

$$\dot{E}_\eta(r) = 2\eta \int_R^\infty 2\pi r h \left[\left(\frac{\partial v}{\partial r} \right)^2 + \left(\frac{v}{r} \right)^2 \right] dr = 4\pi\eta h \dot{R}^2 \ . \tag{1.40}$$

The surface energy gained as the hole grows is $E_\gamma = 2\gamma \cdot \pi R^2$, and therefore the surface energy gained per unit time is:

$$\dot{E}_\gamma = 2\gamma \cdot 2\pi R\dot{R} \ . \tag{1.41}$$

Balancing Eqs. 1.40 and 1.41 gives:

$$\frac{\dot{R}}{R} = \frac{\gamma}{\eta h} \ , \tag{1.42}$$

and therefore the radius of the hole grows exponentially with time:

$$R(t) = R_0 \exp\left(\frac{t}{\tau} \right) \ , \tag{1.43}$$

where the characteristic growth time $\tau = \eta h/\gamma$ contains material parameters. For free-standing films it is found that the rim of the film thickens uniformly because of long-range contraction of the film, unlike in supported dewetting where a ridge forms around the hole [50]. Th absence of a rim during rupture has been confirmed by atomic force microscopy measurements [61, 62]. Since h and γ can be measured independently, the growth rate of holes in thin polymer films allows for the viscosity of the film to be calculated [56]. However, the edges of the holes have very high strain rates, and the film can be strongly shear thinning in the region of a hole. Initially, films are highly entangled, and the high shear strain rate at edge of hole results in a decrease in entanglements and therefore a reduced viscosity. In order to obtain an accurate measurement of η, $R(t)$ must be measured at later times when shear-thinning is not significant [56, 57].

1.3.3 Capillary levelling

Studying viscous behaviour in bulk systems is fairly straightforward thanks to rheometry, however measuring flow on small length scales is much more challenging. Measuring dewetting speed is one option, but the film is inherently out of equilibrium and is therefore highly dependent on the model used in order to extract accurate information. Spreading of a fluid on a surface can also be used, but often has the added complication of a contact line [50].

Alternatively, a polymer film with thickness on the order of hundreds of nanometers can be prepared in the glassy state such that its surface has a well controlled initial geometry with significant excess surface area relative to a flat film. Since the thickness is well below the capillary length, flow is driven by surface tension and mediated by viscosity. When heated above T_g, gradients in Laplace pressure at the surface drive the film to flow to lower its excess surface area, and therefore reduces its excess surface energy. One such geometry is a sharp vertical step on the surface, created by stacking two films, shown schematically in Fig. 1.9(a) [36, 63]. As the step is annealed it can be monitored optically or using atomic force microscopy [63], and is found to flow and broaden with time, shown schematically in Fig. 1.9(b). If the step is on a no-slip solid substrate, such as PS on silicon, late time surface profiles broaden as $t^{1/4}$, and are self-similar in $x/t^{1/4}$, as discussed in Section 1.3. By comparing these self-similar profiles to numerical results of the thin film equation (Eq. 1.26), the capillary velocity, γ/η, can be extracted, providing a robust measurement of flow in thin polymer films [64].

Other initial geometries can be used, including trenches [65], or micrometer diameter cylindrical holes with depths part way through the film [62]. In the case of capillary levelling of cylindrical holes, two self-similar regimes are found: a $t^{-1/4}$ scal-

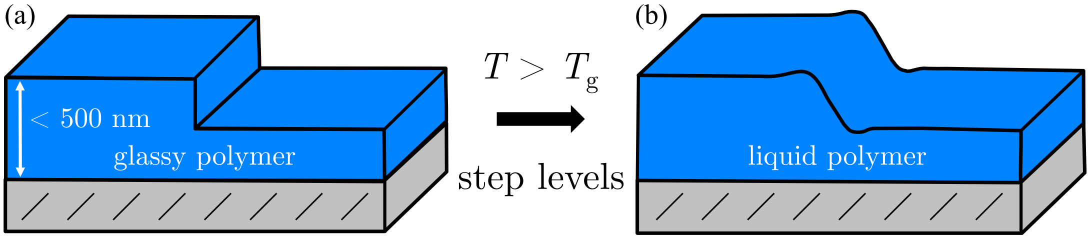

Figure 1.9: (a) A nano-scale polymer film with a stepped polymer-air interface on a solid substrate. (b) When the film is heated above T_{g} gradients in Laplace pressure drive flow, causing the step to level and broaden with time.

ing at early times when the edges of the hole flow independently, and a t^{-1} scaling regime at late times as the hole fills in. The late time scaling is significantly faster than that of supported steps because the film is able to flow azimuthally to fill in the hole. Capillary levelling can be used as a tool to study more exotic systems such as two films with inhomogeneous molecular weight [66]. Levelling experiments have also been used to show enhanced surface mobility below the glass transition temperature [67]. The hydrodynamic boundary conditions of the system can be changed, for example by using a strong-slip substrate [48], a soft substrate [68], or a film which is free-standing in air [9].

Laplace pressure will drive the curvature of a free-standing fluid film to become symmetric with respect to its midplane. Capillary levelling experiments with free-standing steps were performed with films prepared in a similar way to steps on supported substrate, but were instead held on metallic washers [9]. The films were only held around the edge of the washer, like a drumhead, meaning that the film had two fluid-air interfaces. Initially there are large curvature gradients in the region of the step, while the underside of the film is flat. This means there is a large driving force to balance the Laplace pressures at the two interfaces, which causes the film to rapidly symmetrize, however, it was found that this symmetrization occurred on a time scale which was not accessible experimentally. The free-standing step profiles showed self-similarity at late times in $x/t^{1/2}$, as predicted by Eq. 1.30. Again, comparing these self-similar profiles to numerical solutions of Eq. 1.30 allowed the capillary velocity of the polymer to be extracted, which showed good agreement with values measured for supported steps [9].

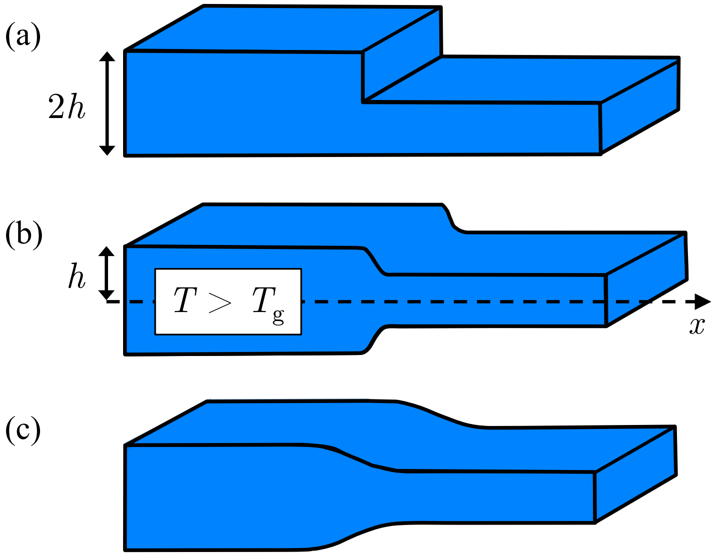

Figure 1.10: (a) A free-standing polymer step with two polymer-air interfaces at $T < T_{\mathrm{g}}$. (b) When the step is heated above T_{g}, Laplace pressure drives vertical flow and the formation of symmetric interfaces. (c) Upon continued annealing the film flows and the step broadens with self-similar scaling in $x/t^{1/2}$.

Paper I discusses the dynamics of the symmetrization of cylindrical holes in free-standing films. The hole geometry allows for the use of higher M_{w} films, because the nucleation of holes is not limited by molecular weight, whereas sharp steps are difficult to create for films with $M_{\mathrm{w}} > 50$ kg/mol. By using higher molecular weights, symmetrization in this geometry is significantly slower than for free-standing steps, making the dynamics experimentally accessible.

1.3.4 Fluid spreading on a solid surface

If a droplet of a non-volatile viscous liquid is placed on a clean solid surface such that its contact angle greater than its equilibrium contact angle, the droplet will spread on the surface and flow towards its equilibrium state. We can define the capillary number, Ca, as the ratio between viscous and surface tension force: $\mathrm{Ca} = \eta v/\gamma$, where v is the speed of the wetting front. For 3-dimensional flow, the shape of the droplet during spreading can be approximated as a spherical cap if the capillary number is low. For typical wetting experiments Ca $\sim 10^{-5} - 10^{-3}$, meaning that surface tension dominates viscosity and that the spherical cap approximation is valid. If the liquid fully wets the solid ($S > 0$, $\theta_\mathrm{e} = 0$) and the size of the droplet is below the capillary length (meaning gravity plays no role), the dynamics of the spreading are universally described by Tanner's law [69], which describes the dynamic contact angle of a droplet of volume V_0 as a function of time:

$$\theta_\mathrm{d} \propto (t/\tau)^{-3/10} \ , \tag{1.44}$$

where $\tau = V_0^{1/3}\eta/\gamma$ is the relaxation time. Alternatively, this equation can be rewritten to describe the dynamics of the droplet radius, $R(t) \propto t^{1/10}$, or height, $h(t) \propto t^{-1/5}$. This result is only dependent on properties of the fluid and is independent of S as long as $S > 0$. The derivation of this spreading rate is based on viscous wedge dissipation at the contact line, and uses the lubrication approximation, volume conservation, and the assumption that the droplet profiles are self-similar with time [39]. This result is in agreement with many experiments performed using a variety of liquids and solid substrates [70, 71].

The universality of Tanner's law is somewhat surprising given that it appears intuitively that for any increase in the radius of the droplet should decrease the surface energy by πSR^2, meaning that the spreading rate would be dependent on the magnitude of the wettability parameter, S. In practice, spreading takes place in two stages, beginning with the formation of a microscopic precursor film which spreads ahead of the macroscopic contact line [49]. This precursor film has a macroscopic lateral extent and a thickness ranging from a few molecules to ∼100 Å [50]. The existence of a precursor film means that $S = 0$ on the time scale of the macroscopic spreading. The surface energy of the spherical cap relative to the dry substrate is:

$$F_\mathrm{s} = \frac{4V_0^2\gamma}{\pi R^4} - \pi SR^2 \ , \tag{1.45}$$

where the first term is the liquid-air interfacial energy and the second is the liquid-solid interfacial energy. If $S = 0$ and R is large, there is little reduction in surface energy by increasing R, meaning that for a droplet of any liquid that completely wets a substrate, spreading occurs slowly and the spreading rate is independent of S. For total wetting the droplet continues to spread until it reaches a final thickness determined by the effective interface potential. Tanner's law breaks down as h becomes comparable to the range of the effective interaction between the solid surface and the liquid-vapour interface.

In real fluids there is a stochastic contribution to the velocity field because of thermal fluctuations in the distribution of molecular velocities [72]. Thermal fluctuations can become significant in spreading experiments because of the small length scales of the wetting edge and the precursor film. The addition of thermal fluctuations at the wetting edge to hydrodynamic theories of fluid spreading increases the rate of spreading in comparison to Tanner's law [72]. For example, Tanner's law for a droplet spreading purely due to capillarity in 2D predicts the radius of the droplet scales as $t^{1/7}$, whereas the addition of thermal fluctuations increases the spreading rate to $t^{1/5}$ [73]. Thermal fluctuations also decrease the equilibrium contact angle and increase the precursor film thickness, meaning that the droplet height decreases due to conservation of volume [73]. The influence of thermal fluctuations on the spreading of a liquid driven by the deformation of a rigid film is discussed in Paper II.

1.4 Elasticity of solid films

We now move from fluids to a brief discussion of the theory of linear elasticity of solids, relevant for Paper II and Paper III. This section will focus on scalar deformations of compliant solids, either soft solids or slender rigid structures such as thin films. For a full tensor treatment of elasticity the reader is referred to Refs. [74] and [75].

A material is said to behave elastically if it maintains its original shape after the application and removal of any small deformation. If the shape changes permanently the material has undergone plastic deformation. When a stress σ is applied to a cube with sides of length l_{i}, the deformation of an elastic solid is described by its strain, $\epsilon = (l_{\mathrm{f}} - l_{\mathrm{i}})/l_{\mathrm{i}}$, where l_{f} is the resulting length parallel to the applied stress. The relationship between stress and strain for an elastic solid is known as Hooke's law: $\sigma = E\epsilon$, where E is the Youngs modulus, which quantifies the stiffness of the material. When an elastic material is stretched (or compressed) in one direction it contracts (or expands) in the two perpendicular directions. This effect is quantified by the material's Poisson's ratio, ν. Most materials have $0 < \nu < 0.5$, with $\nu \approx 0.3$ for glassy polymers [37], and the upper limit of $\nu = 0.5$ being a perfectly incompressible material which conserves volume upon deformation, such as the elastomeric materials described in Section 1.4.2.

The solid materials discussed in this thesis take the form of thin plates or films, where the lateral dimensions are orders of magnitude larger than the thickness. These slender films allow for simplifications of the elastic equations. One important simplification is "plane stress": if the film is in xy-plane all elastic stresses occur within the plane of the film, with no stress components in z.

1.4.1 Bending versus compression

When a rigid slender film with elastic modulus E_f and thickness h is compressed laterally, it can undergo two possible deformation modes: in-plane compression or out-of-plane bending, shown schematically in Fig. 1.11(b) and (c). These modes can both be present in a given system, although one generally dominates over the other. For small lateral loads pure compression occurs, where the in-plane strain has no gradient across the film's thickness. At higher strain the film becomes more geometrically confined, and eventually will spontaneously deform into a buckle of amplitude w in order to accommodate its excess length, as shown in Fig. 1.11(c). This buckle occurs with a length scale comparable to the total sample length, and disappears when the applied strain is removed. The length along the mid-plane of the film is preserved, meaning that the side of the film with the concave surface is under compression, while the other side is stretched and therefore under tension.

The relative importance of bending and compression for a particular sample can be found by considering how their energies scale with the sample's geometrical parameters. The elastic energy of a film of length L is the sum of the compressive energy, U_c, and bending energy, U_b, and scales as [74]:

$$U = U_\mathrm{c} + U_\mathrm{b} \sim Eh\left(\frac{w}{L}\right)^4 + Eh^3\left(\frac{w}{L^2}\right)^2 . \qquad (1.46)$$

The ratio of bending and compressive energies scales as $U_\mathrm{b}/U_\mathrm{c} \sim h^2/w^2$, meaning that for thin films with $h \ll w$, $U_\mathrm{c} \gg U_\mathrm{b}$, and the film will prefer to buckle upon compression. The fact that bending dominates compression for thin films becomes immediately clear when trying to compress a sheet of paper.

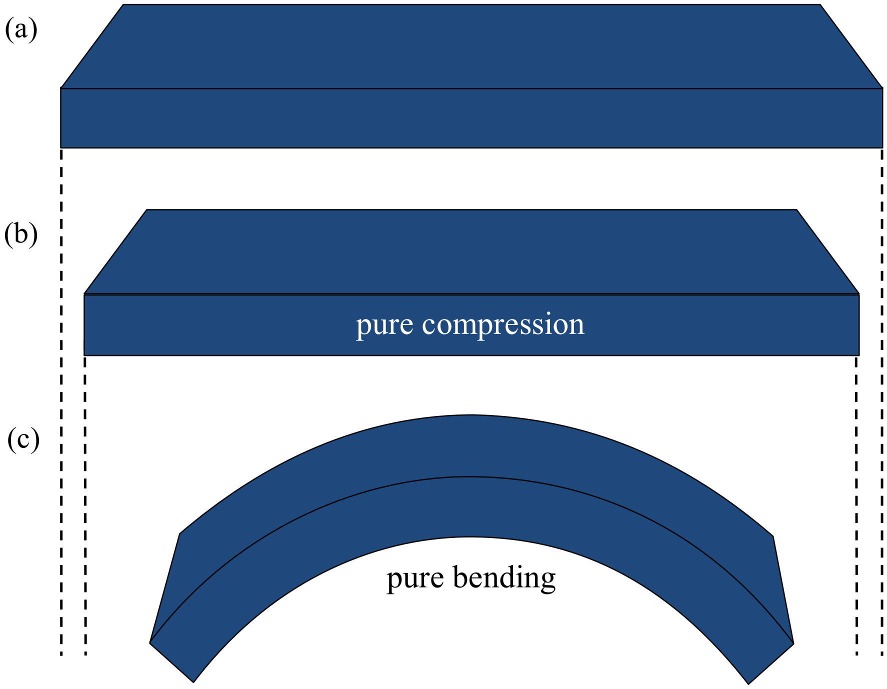

Figure 1.11: Schematics showing (a) an undeformed elastic film, (b) pure compression, and (c) pure bending.

The Föppl–von Kármán (FvK) equation gives a quantitative description of the deformation of a film subject to a compressive load, P, and includes both bending and stretching [74]. Analytic solutions to the FvK equation often only exist in limiting cases where either bending or stretching dominate. For a thin film where bending is dominant, the differential equation governing the deflection of the film is:

$$B\left(\frac{\partial^4 w}{\partial x^4}+2\frac{\partial^4 w}{\partial x^2\partial y^2}+\frac{\partial^4 w}{\partial y^4}\right)=P\ , \tag{1.47}$$

where $B = Eh^3/12(1-\nu^2)$ is the bending rigidity of the film. If the deformation is invariant in y, the equation is simplified further to:

$$B\frac{\partial^4 w}{\partial x^4}=P\ . \tag{1.48}$$

A modified version of the bending dominant FvK is used again is Section 1.5.1 to calculate the wrinkling wavelength of a rigid film on a soft substrate.

1.4.2 Elastomeric materials

Many applications require materials that can remain elastic under large tensile strains. Glassy polymer materials typically have moduli on the order of 1 GPa, and only remain elastic when strained up to ∼10 % [37]. When strained further, glassy materials begin to deform plastically before eventually failing. For example, a thin entangled polymer film strained just before the point of failure can undergo a strain localization process called crazing, in which regions of the film thin significantly while other regions retain their original thickness [76]. On the molecular level crazes occur because individual polymer chains become stretched, which causes the film to thin.

Polymeric solids can be made more elastic by creating a macroscopic network of polymer chains in the melt which are bonded together at fixed points called cross-links. These materials are known as elastomers, and the nature of the cross-links can be either chemical or physical [29]. Chain segments in the regions between cross-links remain locally liquid-like when above their respective T_g, but the cross-links mean that the network is not free to flow on long length scales, resulting in a macroscopic material that behaves mechanically as a solid. As discussed earlier, there is an entropic restoring force that acts to return a chain to its equilibrium size when it is deformed. Therefore, if a bulk elastomeric material is strained and then released, each of the soft liquid-like regions is entropically driven to relax back to the equilibrium size of the chains, meaning that the elastomer is restored to its initial size, and thus behaves elastically. Because of these soft regions, elastomers can be strained to much higher values than typical glassy materials, however, the stress-strain behaviour becomes non-linear with increasing strains [29].

Chemical cross-linking creates permanent covalent bonds between chains, as is the case for rubbers. Elastomers can also be made by forming physical cross-links, which create a network consisting of “hard” and “soft” regions. If the chains are capable of forming microcrystalline regions upon cooling, multiple chains can become physically bonded, shown is Fig. 1.12(a). An example of this is Elastollan (used in Paper III), which is a polyurathane multiblock copolymer [77]. Each chain consists of

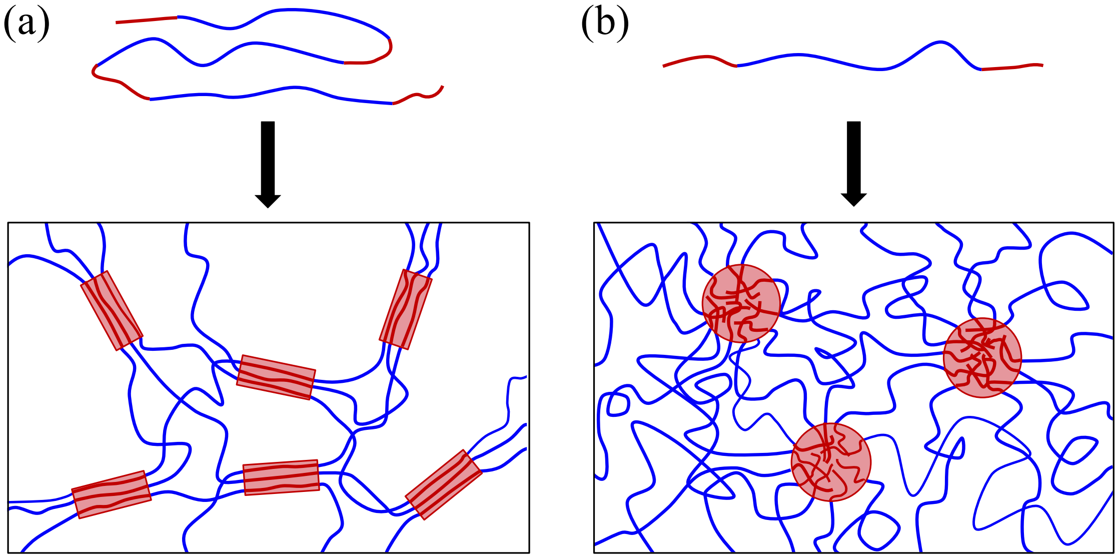

Figure 1.12: Thermoplastic elastomer materials with hard chain segments ($T < T_\mathrm{g}$) shown in red and soft segments ($T > T_\mathrm{g}$) shown in blue. (a) A multiblock copolymer, such as Elastollan, with alternating hard and soft segments, in which the hard segments form crystalline regions (red boxes) which act as physical cross-links. (b) A triblock copolymer, such as styrene-isoprene-styrene, which micro-phase separates to form glassy regions (red circles) which act as physical cross-links, while the soft segments remain locally liquid-like.

alternating hard and soft segments. When cooled, the hard segments from multiple chains form microcrystalline regions which act as physical cross-links and create a network of soft chains. Similarly, elastomers can be formed using a triblock copolymer of two chemically distinct polymers, A and B, of the form A-B-A, such as styrene-isoprene-styrene (SIS) copolymer. When cooled to room temperature, the PS sections of the copolymer micro-phase separate to form spherical domains which are glassy below 100 °C, while the polyisoprene segments remain locally liquid-like, since $T_\mathrm{g} = -60$ °C for polyisoprene. These micro-phase separated regions tether the liquid chains together, creating physical cross-links and a macroscopic elastomer network. Elastomers with physical cross-links are known as "thermoplastic" elastomers because the cross-links break up at high temperatures, allowing the elastomer to be reshaped and then reformed upon cooling.

1.4.3 Elastocapillarity and elastohydrodynamics

Fluids and soft or slender solids can interact with one another, coupling elasticity and capillarity or elasticity and hydrodynamics. These interactions can be used as a form of self-assembly, or for creating complex microstructures [78]. The capillary force of a liquid can produce deformations in a highly compliant elastic material, known as elastocapillarity [79]. High compliance can mean either soft solids, such as elastomers, or slender structures such as thin films or fibres. For liquid droplets on a soft surface this causes a deformation at the contact line, where the solid-liquid surface tensions pulls the substrate upward to balance vertical forces, resulting in a wetting ridge [80]. This ridge dissipates elastic energy, affecting the shape of the rim during the dewetting of a liquid off of a soft solid, and also changing the dewetting rate from that on a rigid solid [81, 82]. Also, anisotropic tension in the film alters the shape of dewetting holes [82] or sessile droplets [83, 84], which could have micropatterning applications. Capillarity can also deform slender rods, causing them to wrap around droplets or coagulate like wet hair [85], and has self-assembly applications by bundling micropillars [22, 86]. Similarly, thin films are subject to elastocapillarity, wrapping around liquids to create capillary origami [20, 21, 87], or deforming due to the surface tension of a droplet [83], which allows the mechanical tension in thin membranes to be measured [88]. A characteristic length scale arises from a balance of surface tension and elasticity, known as the elastocapillary length:

$$L_{\mathrm{EC}} = \frac{E}{\gamma}\ , \tag{1.49}$$

where E is the elastic modulus of the solid. Below this length capillary forces become significant and are likely to deform the solid. For rigid solids with $E \sim$ GPa, $L_{\mathrm{EC}} \sim 10^{-12}$ m, meaning that the solid does not deform and no wetting ridge is formed. However, for soft solids with $E \sim$ kPa – MPa, L_{EC} can be on the order of $\sim$100 nm for elastomers or $\sim$100 μm for soft gels, meaning the elastocapillary deformation of the solid at the wetting ridge is easily observable with optical microscopy or atomic force microscopy [82, 89].

The coupling of an elastic force, fluid flow pressure, and gravity is known as elastohydrodynamics. The bending or stretching energy of an elastic film with non-spontaneous curvature can drive flow in a viscous fluid, or alternatively, fluid flow pressure can deform an elastic film. Examples of elastohydrodynamics exist on length scales ranging from geophysical, such as magma intrusion under rock [19], to physiological, such as the formation and growth of blisters [90] and arterial pumping [18, 91]. Analogous to the capillary length, Eq. 1.20, a characteristic length scale can be defined at which bending stress and gravity contribute equally, known as the elastogravity length:

$$L_{\mathrm{EG}} = \left(\frac{B}{\rho g}\right)^{1/4} , \tag{1.50}$$

where B is the bending rigidity of the film and ρ is the density of the fluid. For experimental lengths below L_{EG} gravity can be neglected.

Building on the discussion of capillary-driven spreading of a fluid in Section 1.3.4, one could imagine a situation in which a fluid perturbation is capped by a thin elastic sheet. The bending energy of the sheet can drive flow, causing the fluid to spread and the height of the perturbation to decrease. Most experiments done to study elastohydrodynamic spreading involve the pumping of a fluid under an initially flat elastic film, creating a “blister”. For perturbations with vertical length scales below the elastogravity length gravity can be safely neglected. Analogous to the contact line in Tanner’s law, the dynamics of the spreading of a fluid under an elastic film is dominated by a balance of viscous and elastic forces at the edge of the fluid, known as the peeling front. Paper II discusses the elastohydrodyanmic spreading of a viscous fluid capped by a rigid thin film.

1.5 Elastic instabilities

Elastic instabilities at surfaces and interfaces can form under compressive loading, and are ubiquitous in nature on a variety of length scales ranging from the wrinkles on human skin ($l \sim \mu$m) [92], to the growth patterns formed on many fruits and vegetables [93], to geological structures ($l \sim$ m – km) [94]. Evolution has also taken advantage of mechanical instabilities, such as wrinkling and folding in the human brain, which triples the effective surface area and allows for significantly increased information storage and mental functioning [95], or wrinkles on shark skin ($l \sim 100\,\mu$m) which prevent the growth of microbes and create a boundary layer that reduces drag while swimming [96, 97]. Many of these examples of elastic instabilities can be idealized as a bilayer system in which a relatively thin, stiff film is compressed while adhered to a relatively thick, soft substrate. Compression of the bilayer can occur as a result of differential growth, drying of the soft layer, or mechanical confinement [98]. As discussed in Section 1.4.1, it is energetically favourable for a thin film to bend rather than stretching or compressing, however, in this case bending of the capping film causes elastic deformation of the substrate since the two layers are adhered. It is the competition between these two mechanisms, the bending of the film and the stretching of the substrate, discussed in detail in Section 1.5.1, that determines the resulting behaviour of the system in response to compression.

Early research of surface wrinkling and buckling was done to understand the critical buckling stresses for aerospace panels so that mechanical instabilities could be avoided, not utilized [99]. More recently, bilayer stiff film/soft substrate systems have been seen as potentially useful for a variety of applications, including as a facile method for fabricating tuneable and scalable ordered surface structures [23, 100], flexible and stretchable electronics [14, 15, 16], or flexible biomedical sensors [101]. Surface wrinkling can also be used as a metrology to extrapolate the mechanical properties of nano-scale thin films, such as the modulus, which can be difficult to measure accurately using more traditional techniques [102, 103, 104].

The majority of wrinkling experiments done to date involve a thick planar substrate ($H \sim$ mm – cm), often a soft elastomer such as polydimethylsiloxane or a viscous fluid, capped by a relatively thin rigid layer, such as a metallic or polymeric film ($h \sim$ nm – μm). The thickness ratio of the two layers is usually such that the thickness of the substrate is assumed to be semi-infinite relative to the capping film. This assumption greatly simplifies the derivation of wrinkling wavelength.

There are a variety of mechanisms used to generate a compressive strain in the bilayer. Chemical swelling can be used to create differential expansion at the film/substrate interface, which can cause wrinkling [10, 105, 106, 107]. Differential thermal expansion between the film and substrate can also be used to generate strain in the capping film [108]. These two methods are of narrow research interest because they are impractical for many applications and are limited to generating small, isotropic strains, and therefore isotropic wrinkling patterns. The magnitude of strains created is also difficult to control or quantify.

A more versatile wrinkling methodology is to mechanically compress the capping film, either by applying a force to the sides of the bilayer, or by pre-straining a soft, stretchable substrate using a strain stage, and then capping it with a rigid film. Upon release of the pre-strain the rigid film is compressed and can wrinkle. This method gives more control over the magnitude of applied strain and allows for anisotropic stains to be generated, which can generate more complex morphologies [109]. A strain stage was used in Paper III to compress bilayer films, with the experimental details discussed in Section 2.2.2. An overview of some theories and experimental results for the finite substrate regime are discussed in Section 1.5.3.

1.5.1 Wrinkling

Consider a thin rigid film with thickness h and modulus $E_\mathrm{f} \sim$ GPa that is well adhered to a much softer, thicker, elastic substrate with thickness H and modulus $E_\mathrm{s} \sim$ MPa, shown schematically in Fig. 1.13. These bilayers are created, for example, by capping the substrate with a rigid polymeric or metallic film, either by transferring a pre-prepared film [110], depositing a film from vapour [102, 111, 112], or by oxidizing the surface of an elastomeric substrate to create a thin rigid crust [113, 114].

When the bilayer is subjected to an applied compressive force, F, either by pushing on the sides of the bilayer or by relaxing the pre-strained substrate, there is a force balance between the bending of the rigid film and the deformation of the substrate. Above a critical force this results in the sinusoidal wrinkling of the top surface, with a characteristic wavelength λ and amplitude A [23]. If the substrate thickness is taken

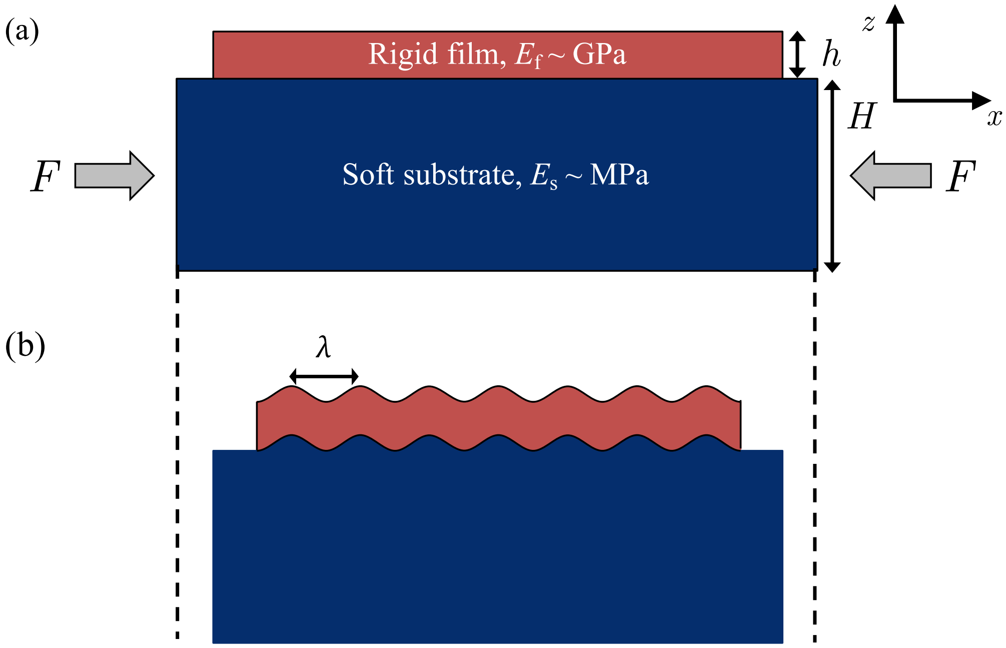

Figure 1.13: (a) A soft planar substrate of thickness H that is capped by a rigid film of thickness h, with $H \gg h$. (b) Compression of the rigid film causes wrinkling with a characteristic wavelength λ because of the trade-off between the bending energy of the film and stretching energy of the substrate.

to be semi-infinite with respect to the thickness of the capping film, the deformation of the bilayer can be calculated quantitatively [74, 115]. Taking the coordinate system to be such that the bilayer is compressed in the x-direction and the deformation occurs in the z-direction, and assuming perfect adhesion between the layers, the system can be described by [74, 112]:

$$\bar{E}_{\mathrm{f}} I \frac{d^4 z}{dx^4} + kz + F\frac{d^2 z}{dx^2} = 0 \ , \tag{1.51}$$

where $\bar{E}_{\mathrm{f}} = E_{\mathrm{f}}/(1-\nu_{\mathrm{f}}^2)$ is the plane strain modulus of the capping film, ν_{f} is the Poisson's ratio, I is the inertial moment of the film, and k is the Winkler modulus of the substrate. In the case of a film of thickness h and width w, $I = wh^3/12$, and for a semi-infinite substrate $k = \bar{E}_{\mathrm{s}} w\pi/\lambda$ [115], where $\bar{E}_{\mathrm{s}}$ is the plane strain modulus of the substrate.

The first term of Eq. 1.51 comes from the bending dominated FvK equation, Eq. 1.48, and the second term describes the elastic response of the substrate by treating it as a series of equivalent springs [115]. Bending favours longer wavelengths, whereas stretching favours shorter wavelengths, and the balance between these two forces determines the resulting characteristic wavelength of the system. Since wrinkling causes a sinusoidal deflection of the surface,

$$z = A \sin\left(\frac{2\pi x}{\lambda}\right) \ , \tag{1.52}$$

and substituting this into Eq. 1.51, it follows that:

$$F = \frac{h^3 \pi^2 w \bar{E}_\mathrm{f}}{3\lambda^2} + \frac{\lambda w \bar{E}_\mathrm{s}}{4\pi} \ . \tag{1.53}$$

This equation describes how the applied force affects the resulting wrinkling pattern. Minimizing Eq. 1.53 with respect to λ gives the critical force required to cause wrinkling:

$$F_\mathrm{c} = \bar{E}_\mathrm{f}^{1/3} \left(3\bar{E}_\mathrm{s}\right)^{2/3} hw/4 \ . \tag{1.54}$$

Substituting this critical force back into Eq. 1.53, the corresponding characteristic wrinkling wavelength is therefore:

$$\lambda = 2\pi h \left(\frac{\bar{E}_f}{3\bar{E}_s}\right)^{1/3} \ . \tag{1.55}$$

This equation suggests that for a relatively stiff capping film ($E_\mathrm{f} \gg E_\mathrm{s}$) the buckling force dominates, favouring a long wavelength, whereas for a relatively stiff substrate ($E_\mathrm{f} \approx E_\mathrm{s}$) the stretching force dominates, favouring a small wavelength. It is also important to note that this equation does not depend of the substrate thickness, H, which was taken to be semi-infinite. Experimental results for a variety of systems show excellent agreement with Eq. 1.55, meaning that surface wrinkling can be used as a metrology to measure E_f, E_s, or h, if two of the other parameters are known [102, 103, 104].

The force applied to a sample is often not well known experimentally, whereas the applied strain is easily observable by measuring the change in the lateral dimensions of the sample upon compression. The applied strain is related to the compressive force by:

$$\epsilon = \frac{\sigma_\mathrm{c}}{\bar{E}_\mathrm{f}} = \frac{F_\mathrm{c}}{hw\bar{E}_\mathrm{f}} \,. \tag{1.56}$$

The critical applied strain required for wrinkling, or equivalently the critical pre-strain in the substrate, can then be found by substituting this into Eq. 1.54:

$$\epsilon_\mathrm{c} = \frac{1}{4}\left(\frac{3\bar{E}_\mathrm{s}}{\bar{E}_\mathrm{f}}\right)^{2/3} . \tag{1.57}$$

This result shows that for stiffer films or soft substrates, the bending term dominates, causing the onset of wrinkling to occur at lower applied strains. For typical experimental systems, such as that discussed in Paper III with $E_\mathrm{f} \approx$ GPa and $E_\mathrm{s} \approx$ MPa, the critical strain is on the order of 0.5 % [110, 116].

A similar result can be derived for the wrinkling of stiff thin films on viscous substrates [98]. The substrate modulus, E_s, is replaced by an effective substrate stiffness ρg, where ρ is the density of the fluid. The resulting equation for the critical wrinkling wavelength is:

$$\lambda = 2\pi\left(\frac{B}{\rho g}\right)^{1/4} . \tag{1.58}$$

where B is the bending stiffness of the film. Wrinkling on a viscous substrate can be used to measure dynamic properties of the fluid by observing how the wrinkling wavelength and amplitude change with time. For example, wrinkling caused by differential thermal expansion between a thin rigid film and a viscous polymer substrate has been used to measure viscoelastic properties of thin polymer films, such as the rubbery plateau modulus [117].

1.5.2 High strain instabilities

At strains beyond the critical wrinkling strain, the capping film becomes more mechanically confined, and strain localization modes and surface failures can occur which break the symmetry of the sinusoidally wrinkled surface. High strain localization modes of soft solids are found in many biological tissues and organs [118], and these instabilities have also been suggested as potentially useful for applications such as surface patterning [119]. The various possible localization modes are shown schematically in Fig. 1.14 and discussed further below. Figure 1.15 shows a phase diagram of mechanical instabilities for a rigid film on a semi-infinite soft substrate as a function of modulus ratio, strain mismatch, and adhesion, calculated using finite element simulations [119]. This phase diagram suggests that the type of instability observed in a given system is most strongly dependent on the modulus ratio of the two films. The adhesion between the layers is also an important factor, but is generally more difficult to control in experiments. This information allows particular instabilities to be either selected or avoided for a given application by tuning the parameters of the sample.

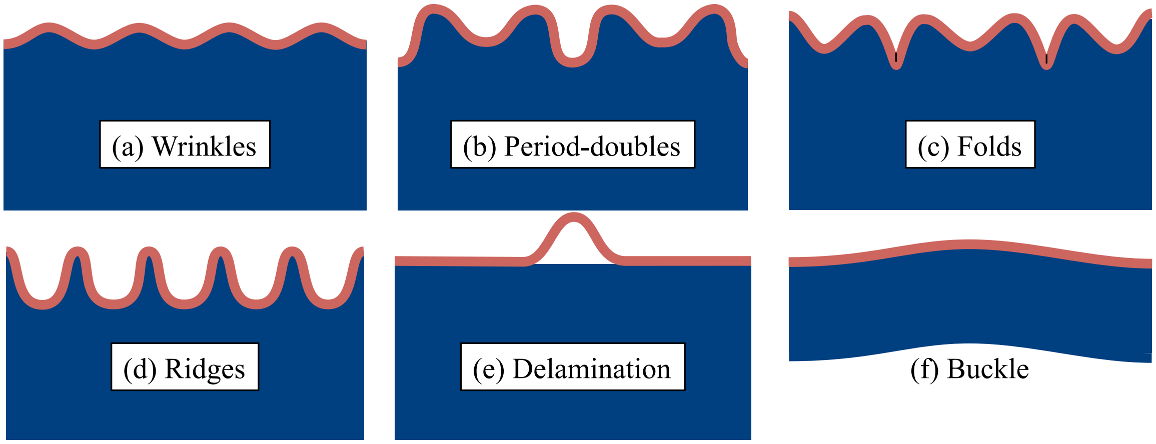

Figure 1.14: Schematic of high strain mechanical instabilities observed in thin film bilayers: (a) wrinkles (b) period-doubling (c) folds (d) ridges (e) delamination (f) buckling.

Localization modes are discontinuities in the surface structure associated with non-linear contributions to the elastic response of the substrate [120]. Essentially, localization of strain on the wrinkled surface causes a bifurcation of the wrinkle amplitude: one wrinkle grows in height at the cost of its neighbours. The bifurcation of wrinkling amplitude can result in period doubling (Fig. 1.14(b)) [121], where the surface transitions from sinusoidal wrinkling to a pattern with twice the period. Upon further compression of relatively soft films and substrates with low pre-strain, folding (Fig. 1.14(c)) can occur, where the film bends into the substrate, creating regions of self-contact [120]. For stiffer substrates ridging can occur (Fig. 1.14(d)), creating high aspect-ratio, non-sinusoidal surface patterns [122]. Surface failures can occur at higher strains, including delamination (Fig. 1.14(e)), where adhesion between the layers is lost and a void is formed [123, 124]. At very high compression plastic failure of the capping film are also possible, including crazing and cracking [110].

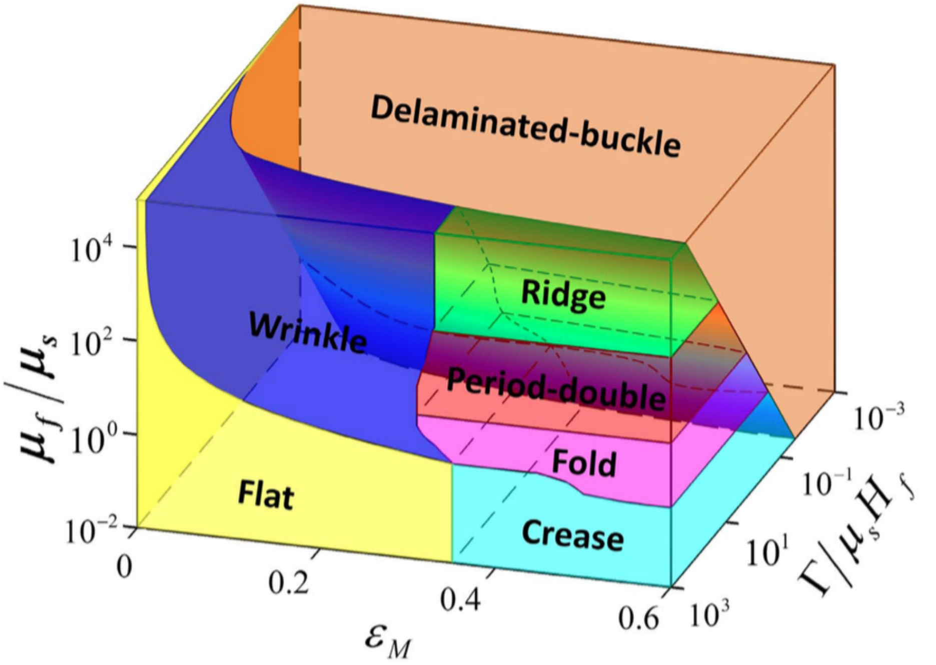

Figure 1.15: A phase diagram of surface instabilities of a bilayer film. The axes represent the strain mismatch between the layers, ϵ_M, the modulus ratio of the film and substrate, μ_f/μ_s, and the adhesion energy between the layers, $\Gamma/\mu_\mathrm{s}H_\mathrm{f}$. Reproduced with permission from Ref. [119].

1.5.3 Instabilities in free-standing bilayers

The above discussion of mechanical instabilities focused on the regime where the soft substrate was assumed to have semi-infinite thickness relative to that of the capping film. This assumption means the deformation of the capping film only affects the stress in the substrate to a depth on the order of the size of the surface structure, while the bottom of the substrate remains flat and stress free. The semi-infinite substrate assumption greatly simplifies the mathematics used to describe mechanical instabilities, but is expected to eventually break down as the relative thickness of the substrate is decreased, or the bending stiffness of the capping film is increased.

Several theories [125, 126, 127] and some experimental results [128] have suggested that in the finite-substrate regime the observed wrinkling wavelength and critical prestrain for wrinkling deviate from the semi-infinite predictions, Eqs. 1.55 and 1.57. The semi-infinite theory also cannot account for the possibility of the entire bilayer undergoing global out-of-plane buckling on a length scale comparable to the total sample length, shown schematically in Fig. 1.14(f), since the bottom of the substrate is assumed to remain flat. Technology continues to push for thinner bilayer structures, and many applications, such as flexible electronics and biomedical devices, require bilayers that can buckle globally. Understanding the critical material and geometrical parameters which govern global buckling is therefore important for designing new technology. Some global buckling experiments have been performed in the context of flexible electronics, but these have used macroscopic samples ($H \sim$ cm) and there is limited experimental data [126, 129]. Models of wrinkling and buckling in the finite substrate regime are also typically more mathematically complex than the semi-infinite case derived above [99]. Paper III discusses experiments studying the transition between local wrinkling and global buckling in thin free-standing bilayers, and presents a basic model based on modifications to the semi-infinite theory presented in Section 1.5.1.

Chapter 2

Experimental techniques

The experimental techniques used in each paper discussed in Chapter 3 are summarized concisely in the paper's text. This chapter provides supplemental information on the main sample preparation and characterization methods used in this work. The materials and techniques involved in creating thin polymeric films, both free-standing or on solid substrates, are discussed in Section 2.1. Section 2.2 discusses specific sample preparation techniques using for each project: the creation of cylindrical holes in free-standing films for Paper I is discussed in Section 2.2.1; the free-standing polymer/elastomer bilayer films from Paper III are discussed in Section 2.2.2; and the creation of cylindrical polymer fibres for Paper II are discussed in Section 2.2.3. Sample characterization techniques used include ellipsometry (Section 2.3.1), optical microscopy (Section 2.3.2), and atomic force microscopy (Section 2.3.3).

2.1 Creating thin polymer films

2.1.1 Materials

Paper I and Paper III used atactic polystyrene (PS) with $M_\mathrm{w} = 183$ kg/mol (Polymer Source, Inc), PDI = 1.06, and $T_{\mathrm{g,\ PS}} = 100$ °C [37]. Thin PS films were prepared by spin coating from dilute toluene solutions with concentrations between 2 % and 10 % (Fisher Scientific, Optima grade), discussed below in Section 2.1.2, resulting in films with thickness between 80 nm and 900 nm. This molecular weight was chosen for Paper I because the viscosity of the film was low enough for significant flow to occur on an experimentally accessible time scale, while being high enough that the fluid film remained stable against rupture on the time scale of the experiment. The mechanical properties of PS were taken from literature to be $E_\mathrm{f} = 3.3$ GPa and $\nu_\mathrm{f} = 0.33$ [130]. It is noted that previous work has suggested the elastic modulus of a PS film begins to decrease from its bulk value as the thickness becomes comparable to the size of the polymer molecules [104], however not all experiments have measured this effect [131]. For Paper III the thinnest film used was 83 nm, or about $7R_\mathrm{g}$ (see Eq. 1.4), meaning that the moduli of the PS films used are assumed to remain at their bulk value.

Paper II used PS fibres and thin films with $M_\mathrm{w} = 15.8$ kg/mol (Polymer Source Inc., Canada), PDI = 1.05, index of refraction $n_\mathrm{PS} = 1.53$ [37], and film thicknesses ranging from 25 nm to 380 nm. The method used to create PS fibres is discussed in Section 2.2.3. Polysulfone (PSU) thin films with $M_\mathrm{n} = 22.0$ kg/mol (Aldrich), and index of refraction $n_\mathrm{PSU} = 1.61$ [37], were prepared by spin coating from dilute cyclohexanone solutions (Sigma-Aldrich, puriss p.a. $> 99.5\%$). PSU was chosen for its high glass transition temperature of $T_\mathrm{g,\,PSU} = 180$ °C [37], allowing experiments to be performed at $T_\mathrm{g,\,PS} < T < T_\mathrm{g,\,PSU}$, such that the PS was a viscous fluid while the PSU remained an elastic solid.

Paper III used two different elastomeric films: pre-prepared Elastosil films (Wacker Chemie AG) with thicknesses of $H = \{20.9 \pm 0.4$ (measured here), 51 ± 1, 104 ± 2, 213 ± 7, or $258 \pm 2\}$ μm [132], and Elastollan TPU 1185A (BASF). Elastollan films were prepared by spin coating from dilute cyclohexanone solutions to create films with thickness between 100 nm and 1 μm.

Two different substrates were used during the sample preparation process. Freshly cleaved mica sheets (Ted Pella, Inc.) were used to spin coat 3×3 cm thin films. Mica was chosen because it provides a clean, flat surface, and allows films of relatively large area to be easily floated onto water surfaces and subsequently transferred to a metal washer (Paper I), another substrate (Paper II), or to a straining stage (Paper III), discussed further below. Silicon wafers (University Wafer) were cleaved into $1{\times}1$ cm substrates and used as a rigid substrate. These silicon wafers are reflective, allowing for ellipsometry to be used to measure film thickness, and for an optical interferometric technique to be used to measure the surface profiles for thin polymer films in Paper III. Stainless steel washers (0.1 mm thick, Accugroup, UK) were used in Paper I to create free-standing PS films which were supported only at the edges of the washer.

2.1.2 Spin coating thin films

Creating films with uniform thickness below 10 μm has been of importance for decades in both research and industry. The most common techniques include dip coating [133], flow coating [134], and spin coating [135]. All of the nano-scale polymer films used in this thesis were all created using spin coating.

Spin coating is used to create polymer films with thickness ranging between 10s of nm to 10s of μm on solid substrates. During the spin coating process, the substrate, in this case mica or silicon, is first attached to a motor via a spin coating chuck. The substrate is then coated with a few drops of a dilute solution of the polymer in a volatile solvent. The motor then accelerates the substrate at $\sim$5000 rpm/s to angular speeds between 2000 rpm and 5000 rpm. As the substrate is accelerated, solvent is quickly ejected radially from the droplet, causing the solution to spread and flatten, creating a uniform film of concentrated solution with a thickness of 10s of μm. As the film continues to spin, solvent evaporates and the polymer chains become less mobile, eventually resulting in a vitrified film of uniform thickness for glassy polymers such as PS and PSU, or an elastomeric film for Elastollan. The film thickness can be controlled by changing the spin speed, and thus the amount of solution that gets ejected, or the concentration of the solution used, with higher concentrations resulting in thicker films [135]. All spin coating done in this thesis was performed with a commercial spin coater (Headway Research Inc., Model PWM32). Solutions in toluene were spun for 20 seconds, whereas solutions made with cyclohexanone were spun for 60 seconds because cyclohexanone is less volatile than toluene.

The polymer chains in films created by spin coating are initially far from equilibrium, and thus need to be annealed above T_{g} prior to use. Annealing also removes residual solvent that may be remaining from the spin coating process. The glassy polymer films used in this work were annealed for multiple hours in a vacuum oven at 10^{-5} mbar and tens of degrees above their respective T_{g}. The ovens consisted of a heating pad in a stainless steel and aluminum chamber with a thermocouple to measure the temperature of the pad. Samples were covered with an aluminum hood and clamped tightly to maintain uniform heat, and the oven was closed with an aluminum lid on a rubber o-ring. Elastollan films were annealed at 150 °C, a temperature at which the film remains physically crosslinked and does not deteriorate.

As done previously by many experiments in the Dalnoki-Veress lab [9, 62, 63], all projects in this work used a "water transfer" method to create freely floating thin films which could then be transferred to other substrates or apparatuses. Films were spun on freshly cleaved mica substrates in order to be floated onto a bath of ultrapure water (18.2 MΩ·cm, Pall, Cascada, LS) in a crystallization dish. All glassware was cleaned thoroughly with Sparkleen 1 (Fisherbrand) and rinsed multiple times with ultrapure water prior to use. Before floating, the films were cut with a scalpel blade ∼1 mm from the edges. Very little pressure was used to avoid creating excess mica dust, which greatly impacts the stability of thin liquid films in Paper I. For the thin Elastollan films used in Paper III, the edges were removed with a cotton swab dipped in acetone. This was done because cutting Elastollan films with a scalpel often caused the films to remain pinned to the mica substrate while attempting to float the film off of the substrate. Glassy thin films can also be cut into smaller pieces using a scalpel blade depending on their intended use. The mica substrate and film were then slowly dipped into the water bath at a ∼45° angle. Since the polymer film is hydrophobic and mica is hydrophilic, water easily penetrates between the film and substrate, and the film is eventually released from the mica, and remains floating freely on the water surface. Small pieces of film or dust were cleaned from the water surface using a suction pump. The pieces of film could then be floated onto a metal washer to create a free-standing film, onto a sample on a silicon wafer, or re-floated back onto the mica substrate. After floating back onto mica, a layer of water remains between the mica and film, which allows the film to be transferred to a straining stage, discussed in Section 2.2.2. Thicker films of PS up to 2 μm were made for Paper III by floating a full PS film onto another film on mica, annealing above $T_{\text{g, PS}}$ to heal the interface between the two films, and then floating off of the mica substrate as usual.

2.2 Sample preparation

2.2.1 Creating free-standing holes

Paper I discusses the capillary levelling of a free-standing PS film which initially has micrometer diameter cylindrical holes part way through the film, shown schematically in Fig. 2.1. The film was made using $M_{\mathrm{w}} = 183$ kg/mol PS, with hole depths of $h_1 =$ 80 nm and a total film thickness $h_1 + h_2 = 610$ nm. After the two films were floated onto the water bath they were picked up from below onto stainless steel washers in order to create free-standing films. The thinner film (h_1) was floated onto a washer with an inner diameter of 5 mm, and the thicker film (h_2) was floated onto a washer with an inner diameter of 3 mm. After floating onto the washers the films were left to dry in a laminar flow hood and then inspected using optical microscopy to check for dust particles, tears in the film, or other visible defects. The free-standing films on washers were initially wrinkled after the floating process. To relax the wrinkles the films were placed on a hot stage (Linkam, UK) and heated at 100 °C/min to slightly above $T_{\mathrm{g,\ PS}}$. When the temperature passes above $T_{\mathrm{g,\ PS}}$, surface tension pulls the film taut and removes the wrinkles. The film remains taut and wrinkle free when quenched back to room temperature. Small pieces of silicon wafer were used to separate the washer and film from the surface of the hot stage in order to prevent impurities from contacting the film surface.

Holes were nucleated in the 80 nm film by rapidly heating further to $T \approx T_{\mathrm{g}} + 20$ °C on a hot stage while under an optical microscope. Imaging was done in either bright field or dark field mode using a 20× or 50× objective in order to observe nucleation and growth of holes in the film. As discussed in Section 1.3.2, holes were nucleated on randomly distributed defects in the film, and generally formed in less than a minute. The holes were monitored as they grew, and when they reached the desired size of 1 – 10 μm diameter, the washer was removed from the hot stage using self-closing tweezers and the film was quenched to room temperature in air. It was found that holes could only be nucleated with this technique in films with $h < 100$ nm. The final sample was made by carefully placing the two films on washers in direct contact, transferring the thinner film with holes onto the thicker film on a 3 mm, shown schematically in Fig. 2.1. The smaller washer is used for the final sample because the reduced area decreases the likelihood of defects causing the bilayer film rupturing at later times.

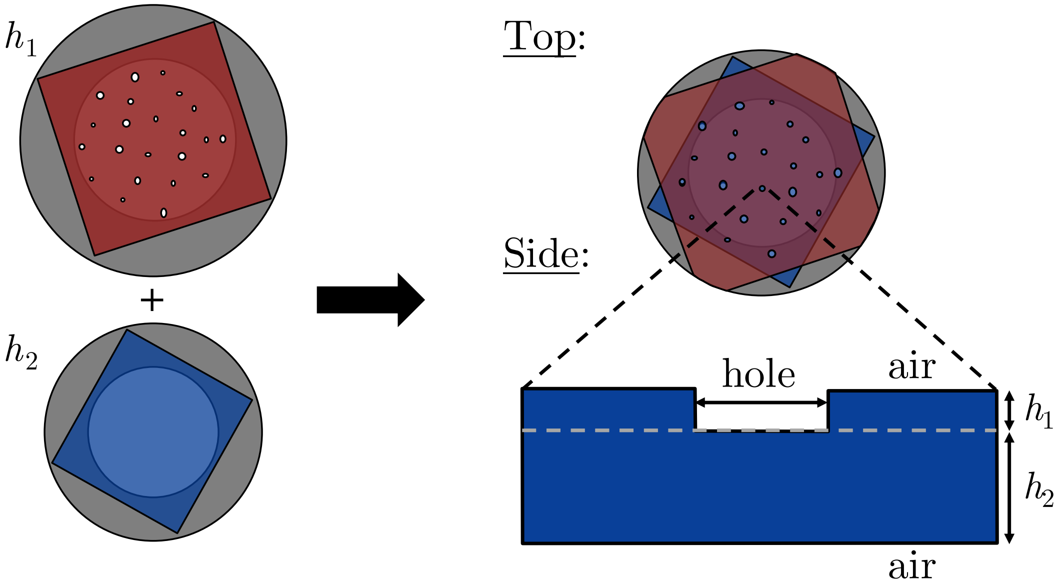

Figure 2.1: Schematic of the sample preparation of a free-standing film with cylindrical holes in the top layer. Holes are nucleated in a film of thickness h_1 on a washer, and combined with a second film of thickness h_2 to create a free-standing film of total thickness $h_1 + h_2$.

The initial sample geometry has cylindrical holes at the "top" polymer-air interface while the "bottom" interface remains flat. The surface profiles of the two polymer-air interfaces were measured using atomic force microscopy, discussed in detail in Section 2.3.3, after various annealing times as the film flowed and evolved. The film was annealed at 130 °C on a hot stage with the washer placed inside a metal ring while supported on small pieces of silicon wafer, and covered with a glass cover slip to ensure uniform heating of the film.

2.2.2 Controlling tension in thin films

Applying a well controlled tension to thin films is a challenging experimental problem. Two home-made strain stages were used in this thesis, shown schematically in Figure

2.2(a), to strain elastomeric films (Paper III) and to create free-standing glassy films with no in-plane tension (Paper II). Both stages were based on a substrate of 250 μm thick Elastosil elastic sheet, which was cut into a rounded plus-shape with a circular hole in the middle. Each leg of the plus shape was clamped to a post on a translation stage, which allowed a film covering the hole to be strained either uniaxially or biaxially by moving the posts independently. A portable strain stage with a 1 cm diameter hole was used in Paper III for bilayer wrinkling experiments, while a second was a larger strain stage with a 2 cm diameter hole, used in Paper II to relax the tension in full mica sheets of PSU.

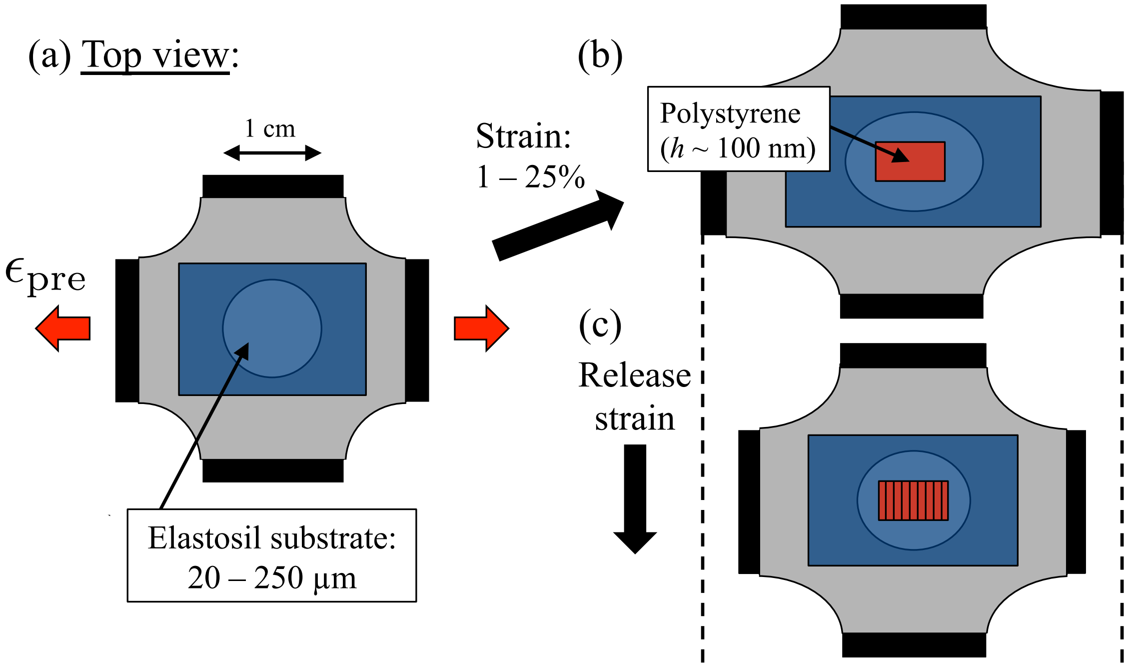

Figure 2.2: (a) A strain stage consisting of a 250 μm thick Elastosil sheet cut into a round plus-shape with a hole in the middle. Each leg of the plus-shape is attached to a post on an optics rail and can be moved independently. The hole is covered with a second film, in this case another Elastosil film. (b) By moving the posts the pre-strain, ϵ_{pre}, in the central Elastosil film can be adjusted, and the Elasosil can then be capped with a thin PS film to create a bilayer. (c) When the pre-strain is released the bilayer is compressed and can undergo a range of mechanical instabilities.

For the bilayer wrinkling experiments discussed in Paper 3, a variety of Elastosil films with thickness between 20 μm and 250 μm were used to cover the hole in the straining stage and act as the substrate. Approximately 3 cm × 3 cm pieces of Elastosil were cut from larger rolls of material, and carefully transferred by hand using tweezers to cover the hole in the strain stage. The zero-tension state of the substrate was found by adjusting the posts of the strain stage just to the point before wrinkles began to appear in the substrate. Other substrate thicknesses could be produced by repeating this process and attaching a second sheet of Elastosil. These double-layer substrates were found to always remain in good contact for the strains used. The substrate was then placed under an optical microscope and strained biaxially by moving two of the posts outward while leaving the other posts fixed in place. The value of pre-strain was measured optically using $\epsilon_{\mathrm{pre}} = (d_{\mathrm{f}} - d_{\mathrm{i}})/d_{\mathrm{i}}$, where d_{i} and d_{f} are the distances between two defects in the substrate aligned parallel to the high strain direction measured before and after straining, respectively. This technique was used to strain Elastosil films by up to 25 %.

A ∼3 mm × 3 mm piece of polystyrene with thickness between 80 nm and 1900 nm was then transferred on top of the pre-strained Elastosil substrate, creating a free-standing bilayer sample such as that shown in Fig. 2.2(c). As discussed in detail in Section 1.5, when the pre-strain was released by moving slowly the two posts back together, a compressive force is applied to the thin capping film, which can then undergo a mechanical instability such as wrinkling or buckling. By observing the surface using optical microscopy, the type of instability could be observed and imaged. By changing the relative thickness of the film and substrate and the applied pre-strain, wrinkling/buckling phase diagrams were produced. The wrinkling wavelength was measured using ImageJ and averaged across the wrinkled region.

2.2.3 Creating polymer fibres

Paper II discusses the bending-driven spreading dynamics of a viscous PS fibre on a silicon substrate pre-wet by a PS thin film of the same M_{w} and capped by a sheet of rigid PSU, shown schematically in Fig. 2.3. Polymeric fibres with diameters of ∼5 μm can be pulled directly from the melt. Small amounts of polystyrene were placed on a silicon wafer on a hot stage and heated to between 150 °C and 180 °C, well above

$T_{\mathrm{g,\,PS}}$. Glass micropipettes were pulled using a commercial pipette puller (Narishige PN-30), to create a pipette that had a ∼5 μm diameter at the tip. This pipette was then dipped into the viscous PS melt and pulled by hand quickly upward. Because of its high viscosity, the melt is entrained and gets pulled along with the pipette, quickly cooling below T_{g} to form a cylindrical glassy fibre. This technique can be used to produce ∼1 m of fibre at a time.

Capped fibre samples were produced by spin coating PS films on silicon wafers, then placing a PS fibre across the width of the film and annealing for a short period of time above $T_{\mathrm{g,\,PS}}$ to allow the fibre to spread to its initial approximately hemi-cylindrical profile. PSU thin films were then created by spin coating on mica substrates and transferred to the 2 cm diameter strain stage, discussed in Section 2.2.2. The zero-tension state was found by moving the posts just to the point before wrinkles began to appear in the film. The silicon substrate with the PS fibre was brought up from below the PSU film until the two films came in contact and adhered. The edges of the PSU film were then removed using a scalpel blade to allow the PSU film to freely slide at the boundaries, creating the sample shown schematically in Fig. 2.3. The freely sliding boundaries mean that the bending of the film will dominate tension.

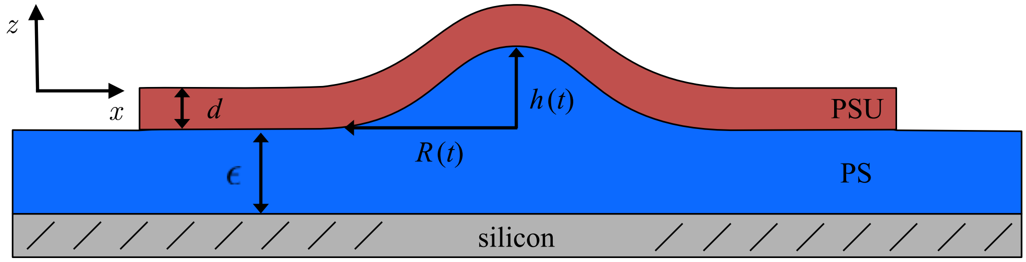

Figure 2.3: Schematic of a viscous PS perturbation of height $h(t)$ and radius $R(t)$ on a pre-wet PS thin film of thickness ϵ on a silicon wafer, capped by a rigid PSU sheet of thickness d. The surface profile is a bump that is invariant in the y-direction. Far away from the region of the bump the elastic film is free to slide on the viscous thin film. As the sample is annealed, the bending energy of the sheet will drive the fluid to flow, and the bump will level and spread with time.

The sample was then heated on a hot stage to $T_{\mathrm{g,\,PS}} < 130\ ^\circ\mathrm{C} < T_{\mathrm{g,\,PSU}}$, meaning that the PS was a viscous liquid while the PSU remained an elastic solid. The bending energy of the elastic sheet drives the fluid to spread and broaden with time, causing the height to decrease and the width to increase. The fibre profile was measured as a function of time during annealing using an optical microscopy technique discussed in detail in Section 2.3.2.

2.3 Sample characterization

2.3.1 Ellipsometry

Accurate film thickness measurements were vital for all projects presented in this thesis. After annealing, the thicknesses of films on silicon substrates were measured using nulling ellipsometry (Accurion, EP3). Ellipsometry is an optical technique used the measure the thickness, h, and index of refraction, n, of thin transparent films [136]. Thickness values can be measured with a precision of ∼0.1 nm. In this work ellipsometry was only done for films on reflective substrates, however ellipsometry can also be performed with free-standing films [4].

Ellipsometry measurements are based on the fact that the polarization of light changes as is passes through a film and is reflected off the substrate. Measuring the change in polarization after reflection can provide information about the sample by comparing the results to models for a given sample geometry [136]. In the case of nulling ellipsometry, monochromatic laser light passes through a variable linear polarizer to create linearly polarized light with angle P. The light then passes through a variable quarter wave plate, known as the compensator, which creates elliptically polarized light. The polarizer and compensator are adjusted such that the light reflected from the sample is linearly polarized. The reflected light passes through a second polarizer, called the analyzer, which only passes light with polarization angle A, and the intensity is measured by a CCD detector. In nulling ellipsometry the analyzer angle is typically held fixed while the polarizer and compensator combination are adjusted to give a minimum in intensity (a null) at the detector, meaning that the light is 90° out of phase with the analyzer. The angles of the polarizer and compensator at the null intensity are unique for a given combination of h and n, allowing the values to be calculated using the ellipsometry equations with initial guesses for h and n.

2.3.2 Optical microscopy

Optical microscopy (OM) was used in each experiment for sample preparation, and also for sample characterization in Papers II and III. In each case the optical microscope used was an Olympus BX51 with 5×, 10×, 20×, and 50× objectives. Images were acquired with a QIMAGING 16 bit CCD camera with capture settings controlled using Image Pro Plus.

In Paper II, the sample surface profile, shown schematically in Fig. 2.3, was measured using an optical interferometric technique. When a transparent thin film on a reflective substrate (such as PS on silicon) is viewed from above using OM with monochromatic light of wavelength λ, the observed intensity is proportional to the reflectance, which changes with the film thickness, h, as [137]:

$$R(h) = \frac{A - B + C\cos\left(4\pi n_{\mathrm{p}} h/\lambda\right)}{A + B + C\cos\left(4\pi n_{\mathrm{p}} h/\lambda\right)}\ , \tag{2.1}$$

where n_{p} is the index of refraction of the film and A, B, and C are constants which depend on n_{p} and the index of refraction of the substrate. This equation is periodic because of the interference of light reflected off of the top surface and that reflected off of the substrate, repeating every $\lambda/2n_{\mathrm{p}}$. Therefore, a change from one intensity extrema to the next opposite extrema corresponds to a change in film height of $\lambda/4n_{\mathrm{p}}$ [63]. If the surface height profile is known to change monotonically in a certain region, the locations of the extrema can be used to recreate the profile. This technique is useful if the symmetry of the sample is well understood, such as a spherical cap [138] or the 2D fibres discussed in Paper II, since it is known that h decreases monotonically from the centre of the fibre toward the two edges.

Figure 2.4 shows typical optical microscopy images of a fibre spreading experiment at three different times, taken with a red laser line filter ($\lambda = 632.8$ nm, Newport, USA). The interferences fringes parallel to the length of the fibre are clearly visible. Analysis of these images was performed using MATLAB. A section of the fibre was selected (the dashed red box) and the intensity profile was averaged along the length of the section, shown in Fig. 2.4(b). The intensity extrema are marked with red dots in Fig. 2.4(b), with the height difference between successive maxima/minima equal to $\Delta h = \lambda/4n = 100$ nm, where $n = 1.57$ is the average index of refraction of

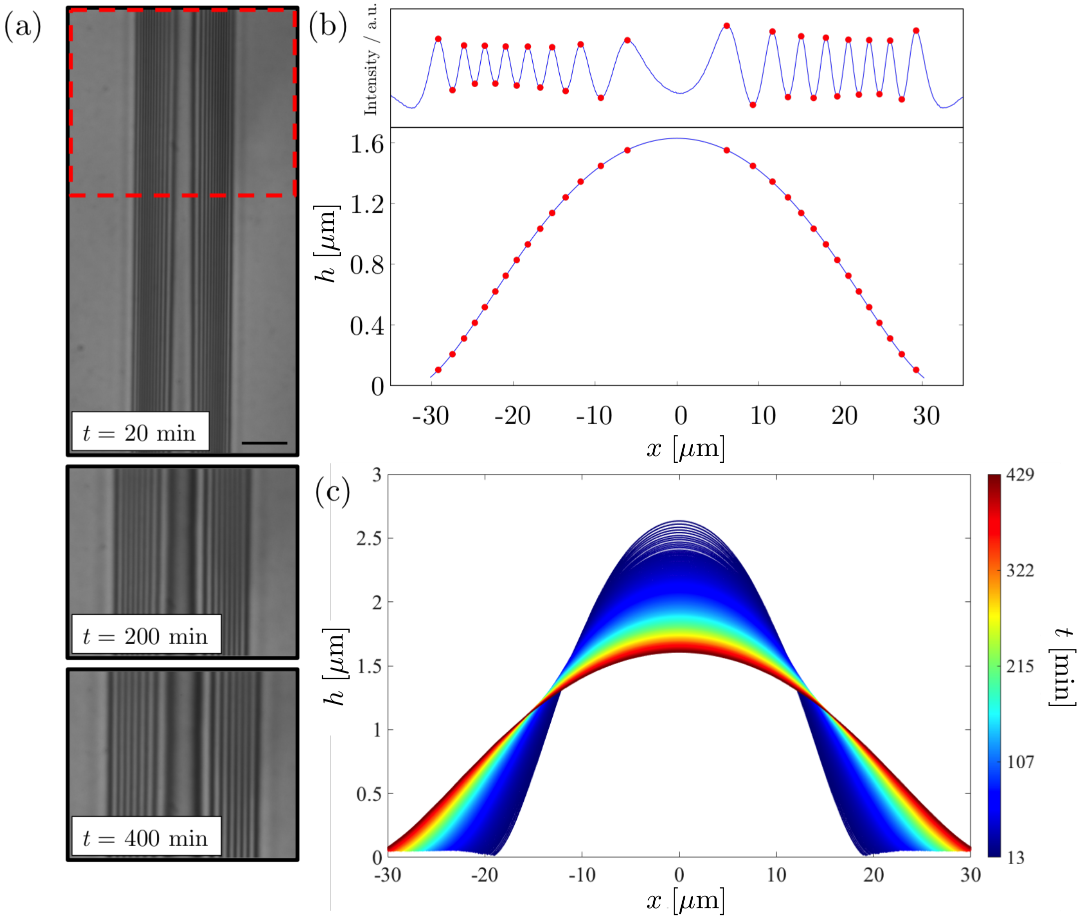

Figure 2.4: (a) Optical microscopy images of a fluid fibre capped by a rigid sheet as the bending energy of the sheet drives the fibre to flow. Imaging with a red filter creates interference fringes in the intensity. (b) The location of the interference fringes can be used to recreate the fibre profile. (c) Imaging as a function of time shows the evolution of the fibre profile.

PS and PSU. Since the fibre is symmetric about the middle and the height increases monotonically from the edge, the averaged height profile could be recreated, shown in Fig. 2.4(c). Atomic force microscopy was used for some samples to confirm the accuracy of the optical technique, and the two methods were shown to be in good agreement. This optical interference technique is somewhat limited in the length scales and height gradients at which it can be used. For films with $h < \lambda/2n$, no fringes will be observed, and for regions with high curvature, such as at early times for the fibre spreading experiment, fringes are so close together that they cannot be resolved accurately.

2.3.3 Atomic force microscopy

Atomic force microscopy (AFM) was used to some degree in each project in this thesis, but most significantly in Paper I to study the surface profiles of cylindrical holes in free-standing polymer films as they underwent capillary levelling. The basics of AFM will be discussed in this Section, with more detail available in Ref. [139].

AFM is a scanning probe microscopy technique used to produce 3-dimensional topographies of samples with vertical length scales under 5 μm. Vertical resolution is on the order of 0.1 nm, far below the resolution attainable with optical microscopy. A sharp tip, typically made of silicon or silicon nitride, with an end diameter of ∼5 nm and a height of a few micrometers is placed on the end of a ∼100 μm long flexible cantilever, which is raster scanned relative to the sample surface using a piezoelectric scanner [139]. Modern AFM scanners typically consist of multiple piezoelectric elements combined into a tube-shaped scanner which can expand or contract independently in $x-$, $y-$, and $z-$directions proportional to an applied voltage. A laser shines off of the reflectively coated back of the cantilever and onto a position-sensitive photodetector. As the tip is scanned across the surface, if it reaches a change in height the cantilever will be deflected and the position of the laser on the photo-detector will change. This change in the position of the laser can be converted into height data, allowing the topography of the surface to be mapped as the tip is scanned across the sample.

The two most common forms of AFM are contact mode and tapping mode. In contact mode the tip remains in continual contact as it is scanned across the surface, with the amount of deflection of the tip kept constant. Because of this continual contact there can be large lateral forces which can damage both the sample and tip. With tapping mode AFM the tip is oscillated by a piezoelectric element near the resonant frequency of the cantilever (∼100 kHz), meaning that contact between the tip and surface is intermittent and wear on the tip is reduced. The driving signal is a sine wave with constant frequency and an amplitude of ∼100 nm. When the tip interacts with the surface, the amplitude of the oscillation of the reflected beam measured by the photo-detector is damped relative to the driving signal, which provides information on the sample height and modulus.

The AFM used in this work was a Bruker Multimode 8, which uses PeakForce Tapping® mode with ScanAsyst®. PeakForce Tapping mode is similar to tapping mode, however the cantilever is driven at ∼2 kHz, well below its resonant frequency. With this AFM, the sample is placed at the top of a tube-shaped 3-axis piezoelectric scanner which moves the sample, while the horizontal position of the tip and cantilever remain fixed. Position-force curves are measured at each pixel and are used as feedback to control the maximal interaction force between the tip and sample, typically on the order of pN, below that of normal tapping mode. The sample and cantilever are viewed from above using a 10x objective and colour CCD camera to find the specific region of interest on the sample surface.

To measure the surface profiles of a free-standing thin film on a washer with AFM in Paper I, the washer was first attached to a magnetic AFM puck using double-sided tape in order to reduce vibration and to make it easier to find a specific location on the film. The region of interest was found using the optical microscope, and the sample was moved by hand using tweezers. Small adjustments to the sample position were then made by moving the piezoelectric scanner manually using micrometers. The centre of the scan was then adjusted electronically by moving the scanner until the hole was in the centre of the scan area. This process was repeated for three holes in the same film, with scan sizes ranging from 20 μm to 40 μm and scan rates of ∼30 μm/s.

Extra care was taken for free-standing AFM measurements. At early times, the sides of the hole are steep, as shown in Fig. 2.5(b), which can be challenging given the relatively large size of the AFM tip. This can result in tip convolution artifacts, where the edges of the hole in the AFM scan appear less sharp than in reality. When the tip moves from the flat region to the edge of the hole, the ScanAsyst feedback loop compensates for the steep edge by increasing the tapping force in order to better track the surface. During experiments, the tapping force was allowed to increased until the trace and retrace scans looked similar, suggesting no tip artifacts were present, and then the peak force value was locked to prevent possible feedback or damage to the sample and tip. After the “top” surface (with the initial holes) was scanned, a novel

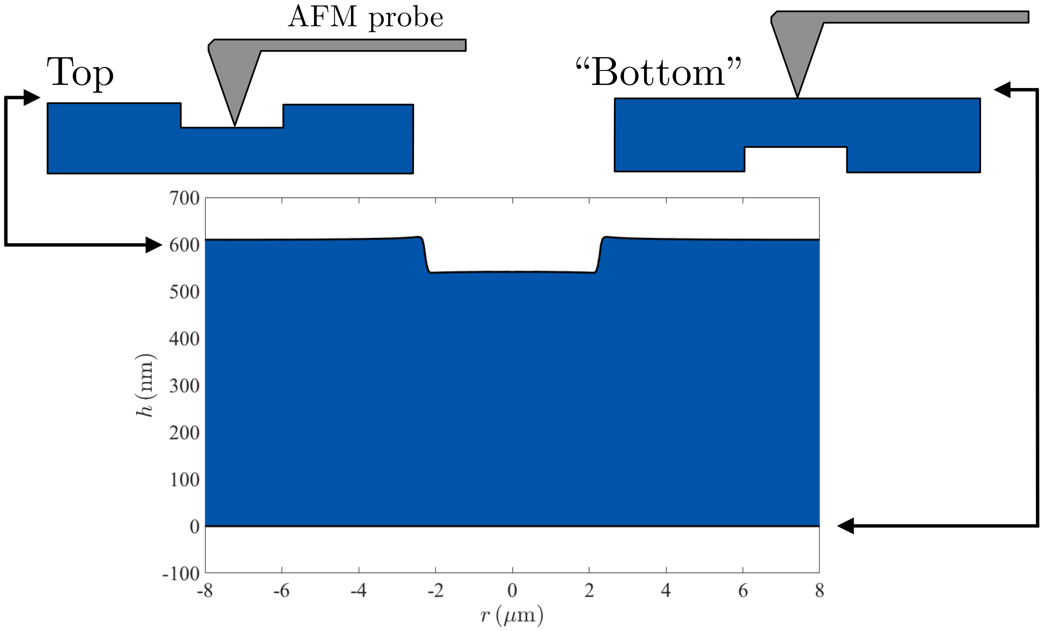

Figure 2.5: (a) Schematic of an AFM measurement of the “top” and “bottom” polymer-air interfaces of a free-standing film. (b) A reconstructed side view of the angularly averaged profiles of a free-standing hole showing both interfaces.

technique was used: the washer was carefully removed from the AFM puck, flipped, and reattached to the double-sided tape. This technique of flipping a free-standing sample to make AFM measurements of both interfaces was only made possible by using 0.1 mm thick washers, because thicker washers interfered with the cantilever. The undersides of the same holes were then found by comparing to images of the top surface, with dust particles and other defects were used as landmarks. By angularly averaging these two profiles, they can be combined to give a side-view of the film after each annealing step, as shown schematically in Figure 2.5. This process was repeated for each hole after various annealing times up to 2000 minutes. As the film evolved, a symmetrization process occurred to equilibrate the Laplace pressures at the two interfaces. The depth of the initial hole was decreased while a second hole was formed on the bottom interface, with this process continuing until the two holes were symmetric about the mid-plane of the film.

The first step of the analysis of the AFM scans was done using Gwyddion. The hole was masked with a circle, and the area outside of the hole was levelled using a 3rd order polynomial to remove the scan parabola. This was then saved as a matrix and opened in MATLAB. The upper profile was angularly averaged about the middle of the hole using code written in MATLAB to give the average profile $h(r)$ as a function of the distance from the centre of the hole, r. The excess surface area, S, of the two surfaces with respect to a flat film was calculated after each time step using:

$$S = 2\pi \int_0^\infty r dr \left(\sqrt{1 + (\partial_r h(r))^2} - 1 \right) \ , \tag{2.2}$$

where r is the distance from the centre of the hole.

Chapter 3

Papers

This chapter contains the main papers discussed within this thesis. Each paper is prefaced by a brief summary of the project, the results, and main conclusions. My contribution to each paper is also stated. A paper for which I was not the primary contributor is included in Appendix A.

3.1 Paper I

Symmetrization of Thin Free-Standing Liquid Films via Capillary-Driven Flow

Vincent Bertin*, John F. Niven*, Howard A. Stone, Thomas Salez, Elie Raphaël, and Kari Dalnoki-Veress (*shared first authorship). Submitted to *Physical Review Letters*, December 2019. Manuscript ID: LM16839.

In this project we continued the use of capillary levelling to study flow in thin polymer films with varying initial geometries. This work was motivated in part by a previous project done in the Dalnoki-Veress lab studying the capillary levelling of sharp steps in polystyrene films which were free-standing in air [9]. It was found that the steps flowed vertically at early times to equilibrate the Laplace pressures at the two fluid-air interfaces, resulting in a film that was symmetric about its mid-plane. However, this symmetrization was found to occur on a time scale that was not accessible experimentally, meaning that the dynamics of the symmetrization process could not be studied.

In this paper, we studied the capillary levelling of cylindrical holes part way through polystyrene films which were free-standing in air. The sample geometry and preparation were similar to that used to study capillary levelling of cylindrical holes on a solid substrate [62], however special care was required because of the free-standing geometry in order to prevent contamination or rupture. As with the free-standing step, the initial geometry of a free-standing hole creates two fluid-air interfaces with significantly dissimilar excess surface areas. Since flow in this system is driven purely by surface tension, the excess surface area is proportional to the total free energy. By monitoring the two interfaces during flow using atomic force microscopy, the free energy evolution of the system could be measured. A novel AFM technique was developed in order to measure both of the interfaces of a free-standing film on the same sample.

It was found that the film underwent a vertical symmetrization process similar to that found for free-standing steps, however in this case the dynamics were slow enough that they could be well resolved on an experimental time scale. This allowed the free energy of the system to be monitored throughout the symmetrization process, as well as at later times when the film flowed horizontally to fill in the holes, with the $t^{1/2}$ scaling predicted for plug flow. The experimental results are in agreement with a full-Stokes hydrodynamic model developed by Vincent Bertin. The model shows that the symmetrization time depends only on the capillary velocity and the total film thickness while it is independent of the hole size. The comparison between theory and experiment allows for an estimate of the capillary velocity to be extracted, which compares well to values measured using capillary levelling of supported films of comparable M_{w} [36].

I developed preliminary versions of the sample preparation process with the help of Paul Fowler and under the supervision of Dr. Kari Dalnoki-Veress. I developed the final version of the experiment, including the ability to make AFM measurements of both interfaces of the same film, and performed all data collection and analysis. Data analysis was done using Gwyddion and MATLAB. Vincent Bertin developed the theory and performed numerical calculations. I wrote the original version of the manuscript in collaboration with Vincent Bertin and contributed to subsequent versions.

Symmetrization of Thin Free-Standing Liquid Films via Capillary-Driven Flow

Vincent Bertin,[1, 2, *] John F. Niven,[3, *] Howard A. Stone,[4]
Thomas Salez,[1, 5] Elie Raphaël,[2] and Kari Dalnoki-Veress[2, 3, †]

[1]*Univ. Bordeaux, CNRS, LOMA, UMR 5798, 33405 Talence, France.*
[2]*UMR CNRS Gulliver 7083, ESPCI Paris, PSL Research University, 75005 Paris, France.*
[3]*Department of Physics & Astronomy, McMaster University, Hamilton, Ontario L8S 4M1, Canada.*
[4]*Department of Mechanical and Aerospace Engineering,*
Princeton University, Princeton, New Jersey 08544, USA
[5]*Global Station for Soft Matter, Global Institution for Collaborative Research and Education,*
Hokkaido University, Sapporo, Hokkaido 060-0808, Japan.

We present experiments to study the relaxation of a nano-scale cylindrical perturbation at one of the two interfaces of a thin viscous free-standing polymeric film. Driven by capillarity, the film flows and evolves towards equilibrium by first symmetrizing the perturbation between the two interfaces, and eventually broadening the perturbation. A full-Stokes hydrodynamic model is presented which accounts for both the vertical and lateral flows, and which highlights the symmetry in the system. The symmetrization time is found to depend on the membrane thickness, surface tension, and viscosity.

Surface tension will smooth out small interfacial perturbations on a thin liquid film, as the curvature of the perturbation profile induces a Laplace pressure that drives a viscous flow. This capillary-driven levelling causes the brush strokes on paint to flatten, or the spray of small droplets to result in a uniform film. Such flows have been studied in great detail and much of the theoretical framework is provided by the lubrication approximation, whereby one can assume that the flow in the plane of the film dominates, and that the velocity vanishes at the solid-liquid interface [1, 2]. In contrast, for a free-standing liquid film there is no shear-stress at both liquid-air interfaces which modifies the boundary conditions and results in a different phenomenology [1]. These boundary conditions can arise in a variety of situations such as biological membranes [3], soap films [4–9], liquid-crystal films [10–12], fragmentation processes [13], or energy-harvesting technologies [14].

The dynamics of liquid sheets has been studied in great detail in the past decades [15, 16], and shows similarities with the mechanics of elastic plates. The evolution can be described with two dominant modes, which are the stretching and bending modes associated with momentum and torque balances. At macroscopic scales, a viscous sheet experiences bending instabilities such as wrinkling [17–20], and folding [21] when submitted to compressive forces. Such viscous buckling phenomena occur in various contexts, like tectonic-plate dynamics [22, 23] and industrial float-glass processes [24–26].

In thin free-standing films, surface tension is dominant and stabilizes the interfaces against buckling [15]. Most theoretical models in this context assume that the interfaces are mirror-symmetric, and thus focus on the stretching mode, also called the symmetric mode. This approach is employed to study the rupture dynamics of films in the presence of disjoining forces that destabilize long waves in thin film [27–34]. Recently, using nanometric free-standing polystyrene (PS) films, Ilton *et al.* observed that a film with initially asymmetric interfaces symmetrized over short time scales [35]. This symmetrization was attributed to flow perpendicular to the film, but the dynamics was not accessible experimentally.

In this Letter we study the viscocapillary relaxation dynamics of a nanoscale cylindrical perturbation initially present on one of the two interfaces of a thin free-standing PS film. Both the symmetric (viscous stretching) and antisymmetric (viscous bending) modes are probed with experiments (see Fig. 1a-b). Atomic force microscopy (AFM) is used to obtain the profiles of the top and bottom interfaces. A full-Stokes flow linear hydrodynamic model is developed to characterize the relaxation dynamics of the two modes. To provide an intuitive understanding of the energy dissipation as the film relaxes, we turn to the schematic plot of the excess surface energy as a function of time, shown in Fig. 1(c). Initially, the top interfacial profile, denoted h_+, has a high excess energy due to the additional interface that forms the hole, while the bottom interfacial profile h_- is flat and hence has no excess surface energy. The excess free energy resulting from the perturbation drives a flow that is mediated by viscosity, η. As the film evolves, the total energy dissipates as the excess interface decreases. Apart from that global energy dissipation, the symmetrization process requires some energy transfer from the top interface to the bottom one – a coupling that is dominated by vertical flow. Once both interfaces are mirror-symmetric, they relax in tandem dominated by lateral flow. Remarkably, the temporal evolution of the interfacial profiles, when appropriately decomposed into their symmetric and antisymmetric components is found to obey power laws.

Thin films of PS are prepared using a method similar to that previously described [35, 36]. PS with molecular weight M_w = 183 kg/mol (Polymer Source Inc., polydispersity index = 1.06) is dissolved in toluene (Fisher Scientific, Optima grade) with concentrations of 2 % and

---

[*] These two authors contributed equally
[†] dalnoki@mcmaster.ca

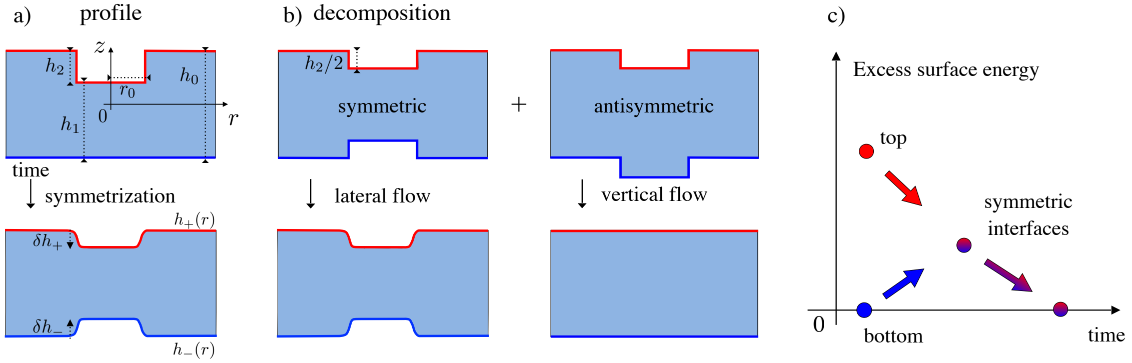

Figure 1. (a) Schematic of an initial cylindrical hole of depth h_2 and radius r_0, on one side of a polystyrene free-standing film, which evolves towards symmetric. (b) Symmetric-asymmetric decomposition of the interfacial profiles. A symmetric profile leads to lateral flow, while an antisymmetric one leads to vertical flow. (c) Schematic of the evolution of the excess surface energy. The top and bottom surface energies equalize rapidly before vanishing in tandem on larger time scales.

7.5 % by weight. Thin films are prepared by spin coating from solution onto freshly cleaved mica sheets (Ted Pella), and annealed at 130 °C in vacuum ($1{\times}10^{-5}$ mbar) for 24 hours. The films have thicknesses $h_1 = 530$ nm and $h_2 = 80$ nm, as measured using ellipsometry (Accurion, EP3). The free-standing films are then prepared in a two-step process inspired by the work of Backholm *et al.* [36]. Films are floated from the mica substrates, onto the surface of ultrapure water (18.2 MΩ·cm) and picked up on a thin circular stainless steel washer (thickness = 0.1 mm, AccuGroup, UK), creating a free-standing thin film supported only at the edges of the washer. The thicker film, with $h_1 = 530$ nm, is picked up on a washer with an internal diameter of 3 mm, and heated above the glass-transition temperature of PS, $T_\mathrm{g} \approx 100$ °C, on a hot stage (Linkam, UK). Similarly, the thinner film with $h_2 = 80$ nm, is transferred from the water to a washer with an internal diameter of 5 mm. This film is rapidly heated (100 °C/min) on a hot stage to 125 °C for several seconds under the view of an optical microscope. During the heating, cylindrical holes are nucleated in the film, and their radii grow exponentially with time [33, 37–39]. When the holes become visible, the film is quenched to room temperature, resulting in a free-standing film with holes of diameter 1 − 10 μm randomly distributed throughout. The two films are then placed in direct contact and adhere through van der Waals forces, and the larger diameter washer can be removed. This process results in a free-standing film of thickness $h_0 = h_1 + h_2$, with cylindrical holes of depth h_2 [see Fig. 1(a, top)].

The free-standing films are annealed on a hot stage at $T = 130$ °C and covered with a glass coverslip to ensure a uniform temperature. After a given amount of annealing time the film is temporarily quenched to room temperature, thus returning to the glassy state where flow becomes arrested. The surface profiles of three holes in the same film are then measured after each annealing step using AFM (Bruker Multimode). Since the film is free-standing and has two polymer-air interfaces, both the top and bottom profiles can be measured. The angular-averaged profiles of the top and bottom interfaces are extracted at each time step to provide a cross-section of the film as it evolves, as shown in Fig. 2.

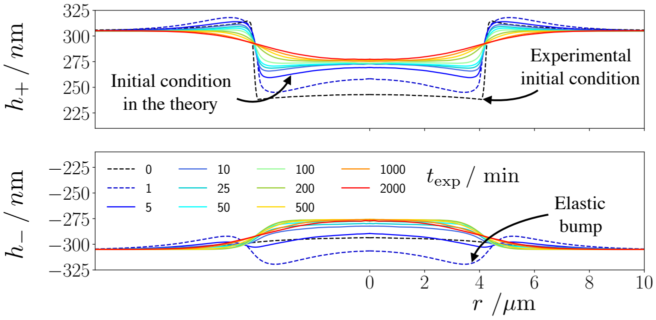

Figure 2. AFM profiles of the top and bottom interfaces of a free-standing hole with $h_2 = 80$ nm, $h_0 = 610$ nm, and $r_0 = 4.2$ μm (see Fig. 1), at various annealing times t_exp as indicated. An "elastic bump" is seen at $t_\mathrm{exp} = 1$ min due to the residual stresses in the film from the sample preparation. The viscous model takes the profiles at 5 min as initial profiles, in order to ignore any prior elastic effect.

Initially, in the region of the hole, the film has significantly different curvature gradients at the top and bottom interfaces, resulting in pressure gradients in both the vertical and lateral directions throughout the film. The initial response of the film in the region of the hole is for the bottom interface to buckle downward, forming a small (∼ 10 nm) "elastic bump". This feature is not a result of the simple polymeric viscoelastic response to interfacial forces [40], as this response would rather generate an opposite inward motion. Instead, while still being related to a viscoelastic process, it is likely a short-term experimental artifact due to the residual stresses associated with sample preparation [38, 39]. As the film is annealed further, the elastic bump relaxes on a time scale ∼ 5 min, which is on the order of the macromolecular relaxation time scale for PS (the reptation time for the PS at the given temperature is ∼ 13 min [41]).

After relaxation of the elastic bump, the flow results from capillarity and viscosity only. First, there is vertical flow to equilibrate the Laplace pressures of the two interfaces, which results in the symmetrization process. Indeed, two symmetric interfacial profiles at the top and bottom of the film are observed at times larger than $\sim$ 200 min. Subsequently, the symmetrized interfacial profiles evolve jointly through lateral uniform flow in order to dissipate the excess surface energy [29]. The film is annealed for $\sim$ 2000 min before rupturing.

We now turn to a theoretical description. The polymer is assumed to be a Newtonian fluid with viscosity η. Given the axial symmetry of the problem, we introduce cylindrical coordinates (r, z), as well as the Hankel transforms [42] of the velocity field $\vec{u}(r, z, t) = (u_r, u_z)$, and of the interfacial profiles $h_\pm(r, t)$: $\tilde{u}_r(k, z, t) = \int_0^\infty \mathrm{d}r\, r\, u_r(r, z, t)\, J_1(kr)$, $\tilde{u}_z(k, z, t) = \int_0^\infty \mathrm{d}r\, r\, u_z(r, z, t)\, J_0(kr)$, and $\tilde{h}_\pm(k, t) = \int_0^\infty \mathrm{d}r\, r\, h_\pm(r, t)\, J_0(kr)$, where t is time, and the J_i are the Bessel functions of the first kind with indices $i = 0, 1$. Injecting these forms into the steady Stokes equations, we find: $\partial_z^3 \tilde{u}_r + k\partial_z^2 \tilde{u}_z - k^2 \partial_z \tilde{u}_r - k^3 \tilde{u}_z = 0$ and $\partial_z \tilde{u}_z + k\tilde{u}_r = 0$, which result in the general solution:

$$\begin{aligned}\tilde{u}_r = &-\frac{1}{k}\left(kA + kzC + D\right)\sinh(kz)\\ &-\frac{1}{k}\left(kB + kzD + C\right)\cosh(kz)\ ,\end{aligned} \tag{1a}$$

$$\tilde{u}_z = \left(A + zC\right)\cosh(kz) + \left(B + zD\right)\sinh(kz)\ , \tag{1b}$$

where $A(t)$, $B(t)$, $C(t)$ and $D(t)$ are integration constants. The depth of the hole is assumed to be small in comparison with the total thickness of the film, which is valid for the experiments, so that we can linearize the problem by writing the profiles as $h_\pm = \pm h_0/2 + \delta h_\pm$, where the perturbations $\delta h_\pm$ are small compared to the film thickness h_0 at rest. We assume no-shear-stress boundary conditions at both fluid-air interfaces, and neglect the nonlinearities from the scalar projections of the normal and tangential vectors to the interface, which gives:

$$\begin{aligned}&(\pm kA + C\frac{kh_0}{2})\sinh(\frac{kh_0}{2})\\ &+(kB \pm D\frac{kh_0}{2})\cosh(\frac{kh_0}{2}) = \pm\frac{\gamma k^2}{2\eta}\delta\tilde{h}_\pm,\end{aligned} \tag{2a}$$

$$\begin{aligned}&\left(kA \pm C\frac{kh_0}{2} + D\right)\cosh\left(\frac{kh_0}{2}\right)\\ &+\left(\pm kB + D\frac{kh_0}{2} \pm C\right)\sinh\left(\frac{kh_0}{2}\right) = 0\ ,\end{aligned} \tag{2b}$$

where γ is the fluid-air interfacial tension. Finally, we invoke the linearized kinematic conditions, $\partial_t \tilde{h}_\pm = \tilde{u}_z(k, z = \pm h_0/2, t)$, and obtain a set of coupled linear differential equations. The symmetric-antisymmetric decomposition, through $\tilde{h}_{\mathrm{sym}} = \delta\tilde{h}_+ - \delta\tilde{h}_-$ and $\tilde{h}_{\mathrm{anti}} = \delta\tilde{h}_+ + \delta\tilde{h}_-$ [see Fig. 1(b)], appears as the natural modal decomposition for this system. These two modes relax independently to equilibrium, with distinct decay rates λ_{sym} and λ_{anti}, since:

$$\partial_t \tilde{h}_{\mathrm{sym}} = -\frac{\gamma k}{\eta}\,\frac{\sinh^2(\frac{kh_0}{2})}{\sinh(kh_0) + kh_0}\tilde{h}_{\mathrm{sym}} = -\lambda_{\mathrm{sym}}\tilde{h}_{\mathrm{sym}}\ , \tag{3a}$$

$$\partial_t \tilde{h}_{\mathrm{anti}} = -\frac{\gamma k}{\eta}\,\frac{\cosh^2(\frac{kh_0}{2})}{\sinh(kh_0) - kh_0}\tilde{h}_{\mathrm{anti}} = -\lambda_{\mathrm{anti}}\tilde{h}_{\mathrm{anti}}\ . \tag{3b}$$

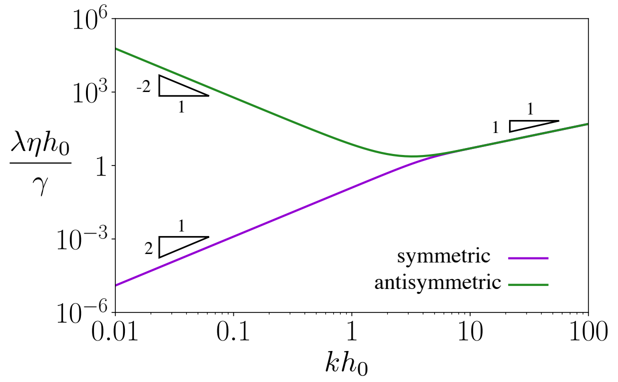

Figure 3. Dimensionless decay rates of the symmetric and antisymmetric modes (Eqs. (3a) and (3b)) as a function of the dimensionless wave number. The slope-triangles indicate power-law exponents.

The dimensionless decay rates are plotted in Fig. 3 as a function of the dimensionless wave number kh_0. For each rate, two asymptotic behaviors can be distinguished. At large kh_0, both rates exhibit the same limit: $\lim_{k\to\infty}\lambda(k) = \frac{\gamma k}{\eta}$. At small kh_0, the symmetric rate becomes identical to the one in the symmetric long-wave free-standing film model: $\lim_{k\to 0}\lambda_{\mathrm{sym}} = \frac{\gamma h_0 k^2}{8\eta}$ [29, 35], and thus Eq. (3a) reduces to a heat-like equation in Hankel space, with a diffusion coefficient $\frac{\gamma h_0}{8\eta}$. In the same limit, the antisymmetric rate has a different scaling law: $\lim_{k\to 0}\lambda_{\mathrm{anti}} = \frac{6\gamma}{\eta h_0^3 k^2}$. Therefore, long waves are quickly damped for the antisymmetric mode. We note that λ_{anti} has a minimum at $k \simeq 3.28/h_0$, corresponding to a slowest mode, which sets the relaxation dynamics.

The model relies on the assumption of a Newtonian fluid. As such, it must be compared to experimental profiles corresponding to annealing times longer than the polymeric relaxation time. Thus, we take the experimental profiles at $t_{\mathrm{exp}} = 5$ min as the initial conditions for the model (see Fig. 2). Equations (3a) and (3b) are

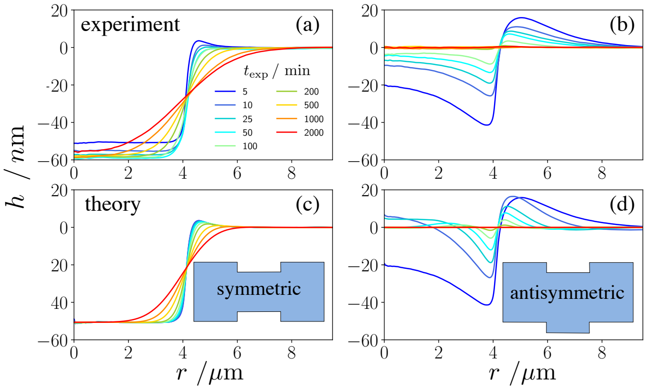

Figure 4. Symmetric (a) and antisymmetric (b) modes of the experimental (angular averaged) profiles for various times. The colors correspond to the same times as in Fig 2. Symmetric (c) and antisymmetric (d) modes of the theoretical profiles, according to Eq. (4), for various times, and with the experimental profiles at $t_{\rm exp} = 5$ min as the initial conditions ($t = 0$).

then solved, yielding:

$$\tilde{h}_{\rm sym/anti}(k,t) = \tilde{h}_{\rm sym/anti}(k,0)\,\exp\left[-\lambda_{\rm sym/anti}(k)t\right] , \tag{4}$$

where $t = t_{\rm exp} - 5$ min. The symmetric and antisymmetric modes for the experimental and theoretical profiles are shown in Fig. 4. There is a qualitative agreement between theory and experiments. Notably, the symmetric mode exhibits a self-similar behavior when plotted (not shown) as a function of the variable $(r - r_0)/t^{1/2}$. This result for free-standing films is to be compared to the capillary levelling of a cylindrical hole in a film supported on a substrate, that shows a self-similar behaviour in $(r - r_0)/t^{1/4}$ [36]. In contrast, the antisymmetric mode vanishes rapidly, on a time scale on the order of ~ 200 min, meaning that the top and bottom interfacial profiles become perfectly mirror-symmetric, as observed in Fig. 2. The long waves appeared to be damped more quickly than the short ones, in agreement with the limiting scaling behaviors of $\lambda_{\rm anti}(k)$ (see Fig. 3).

A measure of the distance to equilibrium lies in the excess capillary energy, which is proportional to the excess surface area with respect to a flat film, $S_i = 2\pi\int_0^\infty {\rm d}r\, r(\sqrt{1 + (\partial_r h_i)^2} - 1)$, where the index i can refer to $+$, $-$, sym, or anti, depending on the profile/mode in question. The excess surface area reduces to $S_i \simeq \pi\int_0^\infty {\rm d}r\, r(\partial_r h_i)^2$ in the small-slope limit (valid at $t_{\rm exp} > 5$ min). Figure 5(a) shows the excess surface areas of the top and bottom profiles, normalized by the initial excess surface area, as a function of dimensionless time, $\gamma t/(h_0\eta)$, for three holes of different initial radii, $r_0 = 2.3\,\mu$m, $4.2\,\mu$m, and $6.2\,\mu$m on the same film. The trends are consistent with the intuitive expectations illustrated in Fig. 1(c), and the theoretical curves are in excellent agreement with the experimental data, which validates the hydrodynamic model. We further see that

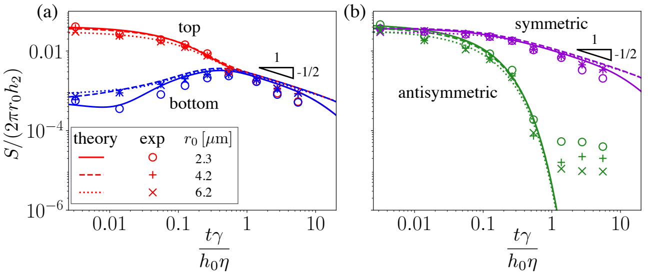

Figure 5. Dimensionless excess surface area as a function of dimensionless time. The experimental data for three different holes are shown with different marker symbols, as indicated. The corresponding theoretical data are shown with different line styles, as indicated. (a) The top and bottom interfacial profiles. (b) The symmetric and antisymmetric modes. The slope-triangles indicate power-law exponents.

the top interface, which has an initially high excess surface area, exchanges energy with the bottom one, causing the excess surface area of the latter to initially increase. This happens through viscous vertical flow, a process that continues until the formation of a mirror-symmetric interfacial profile on the bottom of the film, at $\gamma t/(h_0\eta) \sim 0.5$, after which the excess surface areas of both interfaces are equal. At later times, the surface areas decrease following a power law $S \sim t^{-1/2}$ because of the self-similar properties of the heat-like equation that governs the symmetric mode.

With the modal decomposition above, one can also define and plot the symmetric and antisymmetric surface areas, $S_{\rm sym}$ and $S_{\rm anti}$ respectively, as functions of the dimensionless time (see Fig. 5(b)). The two modes relax with different dynamics. The symmetric mode exhibits a longterm $S_{\rm sym} \sim t^{-1/2}$ scaling, as a result of lateral flow. In contrast, the vertical flow in the antisymmetric mode dissipates energy much more quickly, with a typical time scale $\sim \eta h_0/\gamma$, that is identified as being the symmetrization time scale. The experiments reveal that this symmetrization time scale does not depend on the initial radius of the hole, and is set solely by the dynamics of the slowest relaxation mode, *i.e.* the Fourier-Bessel mode k at which $\lambda_{\rm anti}(k)$ is minimal (see Fig. 3).

It is interesting to note that in real space the governing equation of the antisymmetric mode is $\frac{1}{6}\eta h_0^3\partial_t\nabla^2 h_{\rm anti} = \gamma h_{\rm anti}$, in the long-wave limit. Upon taking the Laplacian of this expression, we recover on the right-hand-side the Laplace pressure difference $\delta P = \gamma\nabla^2 h_{\rm anti}$ across the film. Then, the mid-plane line $H = h_{\rm anti}/2$ follows the equation $\frac{1}{3}\eta h_0^3\,\nabla^4\partial_t H = \delta P$. This equation corresponds to the torque balance in the liquid film [15, 25, 26], and is the viscous analogue of the Föppl-von Kármán equation for an incompressible elastic membrane in pure bending, where the bending modulus is replaced by $\eta h_0^3/3$, and the deflection field is replaced by the deflection rate $\partial_t H$.

In conclusion, we have reported on the symmetrization dynamics of cylindrical holes in free-standing thin viscous polymer films. The topographies of both interfaces of the films were measured using AFM at various times, to track the evolution of the films while they were annealed above their glass-transition temperature. The films were found to undergo a rapid symmetrization process in order to equilibrate the Laplace pressures of the two liquid-air interfaces. This process transfers excess surface energy between the two interfaces, and eventually results in mirror-symmetric profiles on both sides of the film. A full-Stokes flow linear hydrodynamic model was developed to rationalize the observations. The model revealed the important roles of two modes, that differ by their symmetry with respect to the mid-plane of the film. The antisymmetric mode is associated with vertical flow, driven by the pressure gradient across the film, and exhibits faster dynamics than the symmetric mode, associated with lateral flow. The vertical symmetrization was found to occur on a universal time scale $\eta h_0/\gamma$, while the symmetric mode dominates at later times. Surprisingly, the evolutions of the interfacial profiles, when decomposed into the symmetric and anti-symmetric components are found to obey power laws, with the decrease in surface area of the symmetric mode scaling as $t^{-1/2}$, analogous to the heat equation.

We gratefully acknowledge financial support by the Natural Science and Engineering Research Council of Canada. We thank Hendrik Meyer for valuable discussions, and Paul Fowler for help with preliminary experiments.

---

[1] A. Oron, S. H. Davis, and S. G. Bankoff, Rev. Mod. Phys. **69**, 931 (1997).

[2] R. V. Craster and O. K. Matar, Rev. Mod. Phys. **81**, 1131 (2009).

[3] M. Tanaka and E. Sackmann, Nature **437**, 656 (2005).

[4] Y. Couder, J. Chomaz, and M. Rabaud, Physica D **37**, 384 (1989).

[5] M. A. Rutgers, X. Wu, R. Bhagavatula, A. A. Petersen, and W. Goldburg, Phys. Fluids **8**, 2847 (1996).

[6] A. Aradian, E. Raphaël, and P.-G. de Gennes, EPL **55**, 834 (2001).

[7] D. Georgiev and P. Vorobieff, Rev. Sci. Instrum. **73**, 1177 (2002).

[8] M.-J. Huang, C.-Y. Wen, I.-C. Lee, and C.-H. Tsai, Phys. Fluids **16**, 3975 (2004).

[9] J. Seiwert, M. Monloubou, B. Dollet, and I. Cantat, Phys. Rev. Lett. **111**, 094501 (2013).

[10] R. Stannarius, C. Bohley, and A. Eremin, Phys. Rev. Lett. **97**, 097802 (2006).

[11] K. Harth, A. Eremin, and R. Stannarius, Soft Matter **7**, 2858 (2011).

[12] A. Eremin, S. Baumgarten, K. Harth, R. Stannarius, Z. H. Nguyen, A. Goldfain, C. S. Park, J. E. Maclennan, M. A. Glaser, and N. A. Clark, Phys. Rev. Lett. **107**, 268301 (2011).

[13] E. Villermaux, Annu. Rev. Fluid Mech. **39**, 419 (2007).

[14] J. Nie, Z. Wang, Z. Ren, S. Li, X. Chen, and Z. L. Wang, Nat. Commun. **10**, 2264 (2019).

[15] P. D. Howell, Eur. J. Appl. Math. **7**, 321 (1996).

[16] N. M. Ribe, J. Fluid Mech. **457**, 255 (2002).

[17] G. I. Taylor, in *Applied Mechanics* (Springer, 1969) pp. 382–388.

[18] G. Debrégeas, P.-G. de Gennes, and F. Brochard-Wyart, Science **279**, 1704 (1998).

[19] R. da Silveira, S. Chaïeb, and L. Mahadevan, Science **287**, 1468 (2000).

[20] A. Boudaoud and S. Chaïeb, Phys. Rev. E **64**, 050601 (2001).

[21] N. M. Ribe, Phys. Rev. E **68**, 036305 (2003).

[22] M. A. Biot, Geol. Soc. Am. Bull. **72**, 1595 (1961).

[23] L. Guillou-Frottier, J. Buttles, and P. Olson, EPSL **133**, 19 (1995).

[24] J. R. Pearson, *Mechanics of Polymer Processing* (Springer, 1985).

[25] G. Pfingstag, B. Audoly, and A. Boudaoud, J. Fluid Mech. **683**, 112 (2011).

[26] S. Srinivasan, Z. Wei, and L. Mahadevan, Phys. Rev. Fluids **2**, 074103 (2017).

[27] E. Ruckenstein and R. K. Jain, J. Chem. Soc., Faraday Trans. 2 **70**, 132 (1974).

[28] M. Prévost and D. Gallez, J. Chem. Phys. **84**, 4043 (1986).

[29] T. Erneux and S. H. Davis, Phys. Fluid A **5**, 1117 (1993).

[30] D. Vaynblat, J. R. Lister, and T. P. Witelski, Phys. Fluids **13**, 1130 (2001).

[31] O. K. Matar, Phys. Fluids **14**, 4216 (2002).

[32] S. S. Thete, C. Anthony, P. Doshi, M. T. Harris, and O. A. Basaran, Phys. Fluids **28**, 092101 (2016).

[33] M. Ilton, C. DiMaria, and K. Dalnoki-Veress, Phys. Rev. Lett. **117**, 257801 (2016).

[34] A. Choudhury, V. K. Paidi, S. K. Kalpathy, and H. N. Dixit, (2019), arXiv:1902.11018 [physics.flu-dyn].

[35] M. Ilton, M. M. P. Couchman, C. Gerbelot, M. Benzaquen, P. D. Fowler, H. A. Stone, E. Raphaël, K. Dalnoki-Veress, and T. Salez, Phys. Rev. Lett. **117**, 167801 (2016).

[36] M. Backholm, M. Benzaquen, T. Salez, E. Raphaël, and K. Dalnoki-Veress, Soft Matter **10**, 2550 (2014).

[37] G. Debrégeas, P. Martin, and F. Brochard-Wyart, Phys. Rev. Lett. **75**, 3886 (1995).

[38] K. Dalnoki-Veress, B. Nickel, and J. R. Dutcher, Phys. Rev. E **59**, 2153 (1999).

[39] C. B. Roth and J. R. Dutcher, J. Polym. Sci. B **44**, 3011 (2006).

[40] M. Benzaquen, T. Salez, and E. Raphaël, EPL **106**, 36003 (2014).

[41] A. Bach, K. Almdal, H. K. Rasmussed, and O. Hassager, Macromolecules **36**, 5174 (2003).

[42] J. D. Gaskill, *Linear Systems, Fourier Transforms, and Optics*, Vol. 576 (Wiley, 1978).

3.2 Paper II

Asymptotic regimes in elastohydrodynamic and stochastic leveling on a viscous film

Christian Pedersen, John F. Niven, Thomas Salez, Kari Dalnoki-Veress, and Andreas Carlson, *Physical Review Fluids*, 4:123003, 2019.

This paper was motivated by theoretical work and numerical simulations done by our collaborators Dr. Andreas Carlson and Christian Pedersen. The project studied the bending-dominated spreading of a viscous liquid perturbation on a film of the same liquid, that is then capped by a rigid thin film. The perturbation was made by placing a micrometer diameter polystyrene fibre onto a thin film of the same polymer, and then capping it with a film of rigid polysulfone (PSU). When the sample is annealed above $T_{\mathrm{g,\,PS}}$ but below $T_{\mathrm{g,\,PSU}}$, the bending energy of the PSU film drives the fluid perturbation to spread and level with time, thus causing the rigid sheet to flatten. The bending-driven flow in this system differs from the flows discussed in Paper I, which were entirely driven by surface tension.

Theoretical predictions suggested that the scaling of perturbation size depends on the the ratio of the perturbation height to the thickness of the prewet fluid layer, with scaling changing from $t^{2/17}$ for relatively large perturbations, to $t^{1/6}$ for small perturbations. Since the perturbation height changes with time, the theory predicts a sample initially in the large perturbation regime will eventually crossover to the other scaling regime as it flattens. The experiments described above show agreement with the $t^{2/17}$ scaling predicted for large perturbations, but were unable to access the small perturbation regime.

The theory was developed by Christian Pedersen and Dr. Andreas Carlson with input from Dr. Thomas Salez, and numerical simulations were done by Christian Pedersen. I designed the experiment in collaboration with Dr. Dalnoki-Veress, performed all experiments, wrote the MATLAB code to perform image analysis, wrote the experimental section of the manuscript, and assisted with editing subsequent versions of the manuscript.

PHYSICAL REVIEW FLUIDS **4**, 124003 (2019)

Asymptotic regimes in elastohydrodynamic and stochastic leveling on a viscous film

Christian Pedersen,[1] John F. Niven,[2] Thomas Salez,[3,4]
Kari Dalnoki-Veress,[2] and Andreas Carlson[1,*]

[1] *Mechanics Division, Department of Mathematics, University of Oslo, 0316 Oslo, Norway*
[2] *Department of Physics and Astronomy, McMaster University, 1280 Main Street West, Hamilton, Ontario L8S 4M1, Canada*
[3] *Univ. Bordeaux, CNRS, LOMA, UMR 5798, F-33405 Talence, France*
[4] *Global Station for Soft Matter, Global Institution for Collaborative Research and Education, Hokkaido University, Sapporo, Hokkaido 060-0808, Japan*

(Received 21 February 2019; published 19 December 2019)

An elastic sheet that deforms near a solid substrate in a viscous fluid is a situation relevant to various dynamical processes in biology, geophysics, and engineering. Here, we study the relaxation dynamics of an elastic plate resting on a thin viscous film that is supported by a solid substrate. By combining scaling analysis, numerical simulations, and experiments, we identify asymptotic regimes for the elastohydrodynamic leveling of a surface perturbation of the form of a bump, when the flow is driven by either the elastic bending of the plate or thermal fluctuations. In both cases, two distinct regimes are identified when the bump height is either much larger or much smaller than the thickness of the prewetted viscous film. Our analysis reveals a distinct crossover between the similarity exponents with the ratio of the perturbation height to the film height.

DOI: 10.1103/PhysRevFluids.4.124003

I. INTRODUCTION

The motion of an elastic sheet supported by a thin layer of viscous fluid is a phenomenon that manifests itself in processes spanning wide ranges of time and length scales, from, e.g., magmatic intrusion in the Earth's crust [1,2], to fracturing and crack formation in glaciers [3], to pumping in the digestive and arterial systems [4–6], or the construction of two-dimensional (2D) crystals for electronic engineering [7]. Elastohydrodynamic flows have been studied in model geometries in order to understand their generic features and the inherent coupling between the driving force from the elastic deformations of the material and the viscous friction force resisting motion [8–16].

The investigation of an initially flat elastic membrane that is subsequently subjected to an applied deformation has helped disclose how system size, magnitude, and direction of elastic deformations [17] and spatial confinement [18,19] affect the membrane dynamics. When a membrane, resting on a fluid, is either compressed or stretched it can generate wrinkles, where the spatiotemporal dynamics of these folds couple to the fluid flow [18–21]. Wrinkles can be avoided by a slow out-of-plane deformation of an elastic plate by means of injecting additional fluid into the thin prewetted film, which leads to a peeling front driven by bending [22,23]. As the fluid blister grows in size, stretching of the plate generates a tension that starts to dominate over bending. Once the blister is larger than the elasto-gravity length [8], the peeling dynamics again alter character as gravity starts to dominate, giving three distinct regimes for the propagating front [22]. If the supporting film is

---

[*] acarlson@math.uio.no

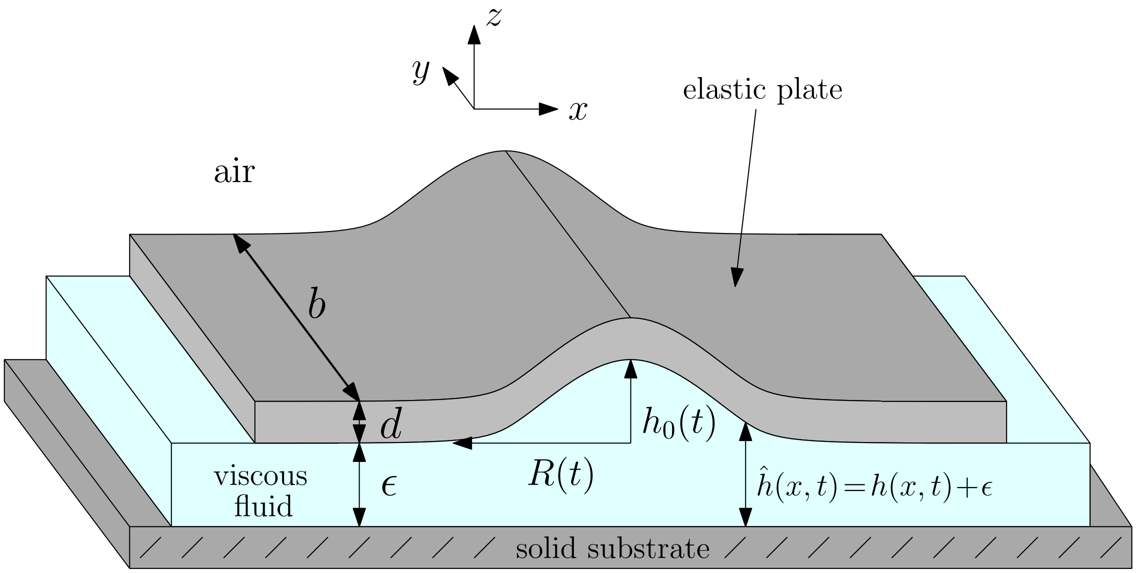

FIG. 1. Schematic of the system we are studying, where an elastic plate is supported by a viscous film on a solid substrate, surrounded by ambient air. The elastic plate has a thickness d and a width b. Initially, the overall profile presents a localized bump, whose profile is invariant in the y direction, i.e., quasi two dimensional. Far away from the perturbation, the viscous film has a constant thickness ϵ. In the bump region, the height profiles $\hat{h}(x,t)$ and $h(x,t) = \hat{h}(x,t) - \epsilon$ of the viscous film and the bump, respectively, vary with the horizontal position x and time t, and remain symmetric about $x = 0$. At $x = 0$, we define the characteristic height $h(x = 0, t) = h_0(t)$ of the bump and its typical radius $R(t)$, with initial values given as $h_0(t = 0) = h_\mathrm{i}$ and $R(t = 0) = R_\mathrm{i}$.

instead of nanoscopic thickness, elastic bending generates a restoring force trying to oppose the van der Waals force that pulls the plate towards the wall and can lead to an elastohydrodynamic touchdown [24] similar to the dewetting of a liquid film [25]. One way to approach a theoretical description of elastohydrodynamics is to solve the Navier-Stokes equations for the fluid flow using boundary conditions at the elastic interface given by the solution of the Föppl-von Kármán equation [26], using, e.g., the immersed-boundary method [27]. Viscous flow in thin films can be described by the lubrication theory [28] that has been widely used to study different elastohydrodynamic flow phenomena [8,22–24,26,29]. However, not much is known about how elastohydrodynamic flows are affected by the ratio between the geometric parameters that characterize the system as it undergoes large changes while the driving force remain the same.

For instance, when an elastic sheet deforms onto a wall prewetted by a thin viscous film, the dynamics of the advancing front is dictated by the local curvature of the interface [16,22]. This elastohydrodynamic relaxation is reminiscent of capillary spreading of a viscous drop onto a solid substrate [30–33]. Similar to capillary flows, elastohydrodynamic relaxation processes are not only limited to very thin prewetted films. In fact, an elastic sheet with zero spontaneous curvature but with an initial shape of a bump (Fig. 1) with a height much larger than the prewetted viscous film will relax towards a flat equilibrium state. Inevitably, the system must then crossover from a situation where the bump height is larger than the prewetted film height to a situation where instead the prewetted film becomes thicker than the bump. Here we investigate how the elastohydrodynamic leveling changes with the ratio between the bump height and the prewetted film thickness. In particular, are there different asymptotic regimes, and how does the system transition from one to another? At the nanoscale, thermal fluctuations are expected to contribute and may even dominate the dynamics [29,34–37], which we quantify in the leveling dynamics. To answer these questions, we combine numerical solutions of a mathematical model based on the lubrication theory [28] with scaling analysis and experiments.

II. MATHEMATICAL MODEL AND NUMERICAL PROCEDURE

We consider the system depicted in Fig. 1, where we focus on a system where any influence of gravity can be neglected, i.e., the bump height is smaller than the elasto-gravity length [8]. The film height is defined as $\hat{h}(x,t) = h(x,t) + \epsilon$, where $h(x,t)$ is the bump height measured from the height ϵ of the pre-wetted layer. Only situations where the bump height $h(x,t)$ is small compared with its horizontal extent and where the film slopes are small, i.e., $\partial\hat{h}(x,t)/\partial x \ll 1$, are considered. We describe the viscous flow between the plate and the solid substrate using lubrication theory [28]. When the initial deflection h_i of the elastic plate is small compared with its thickness d, we can neglect stretching and the pressure reduces to $p(x,t) = B\partial^4\hat{h}(x,t)/\partial x^4$, where $B = Ed^3/[12(1-\nu^2)]$ is the bending rigidity of the plate, E is the Young's modulus, and ν is Poisson's ratio [38]. In addition, the system is a spatially unconfined elastic sheet with the two lateral boundaries being free to move relative to the underlying fluid. Thus, the in-plane compression is suppressed, and bending stresses dominate the relaxation process regardless of the ratio d/h_i. By assuming incompressible flow and imposing no-slip conditions at the two solid substrates, and considering a one-dimensional geometry as there are no variations along the y direction, one obtains the governing equation for the evolution of the height profile (see, e.g., Ref. [8]),

$$\frac{\partial\hat{h}(x,t)}{\partial t} = \frac{\partial}{\partial x}\left[\frac{B}{12\mu}\hat{h}^3(x,t)\frac{\partial^5\hat{h}(x,t)}{\partial x^5} + \Gamma\hat{h}^{3/2}(x,t)\eta(x,t)\right], \tag{1}$$

where μ is the fluid's dynamic viscosity. At small scales, thermal fluctuations can also influence the dynamics, which is described by the last term of Eq. (1). This term mimics the stress generated by thermal fluctuations, originates from an additional symmetric random stress term in the Navier-Stokes equations, and is obtained by an integration in the z direction (for details see Refs. [29,39–41]). The noise term $\eta(x,t)$ is multiplied by a prefactor $\Gamma = \sqrt{k_\mathrm{B}T_\mathrm{A}/(6\mu b)}$ where k_B is the Boltzmann constant, T_A is the ambient temperature, b is the width of the plate along the y direction, and $\eta(x,t)$ is modeled as a spatiotemporal Gaussian white noise such that $\langle\eta(x,t)\rangle = 0$ and $\langle\eta(x,t)\eta(x',t')\rangle = \delta(x-x')\delta(t-t')$, where the $\langle\,\rangle$ symbols indicate average quantities. We nondimensionalize Eq. (1) by using $X = x/R_\mathrm{i}$, $\hat{H}(X,T) = \hat{h}(x,t)/h_\mathrm{i}$, $T = tBh_\mathrm{i}^3/(12\mu R_\mathrm{i}^6)$, and $\Theta(X,T) = \eta(x,t)[12\mu R_\mathrm{i}^7/(Bh_\mathrm{i}^3)]^{1/2}$. When $\Gamma = 0$, this nondimensionalization procedure gives us a parameter-free partial differential equation for $\hat{H}(X,T)$. When $\Gamma > 0$, the nondimensional number $N = [2k_\mathrm{B}T_\mathrm{A}R_\mathrm{i}^3/(Bh_\mathrm{i}^2 b)]^{1/2}$ appears as a prefactor in front of the stochastic term, and N^2 measures the ratio between thermal and bending energies. For the macroscopic system provided in our experiment and described in detail below, i.e., $T_A = 300$ K, $h_\mathrm{i} = 2.5\ \mu$m, $R_\mathrm{i} = 20\ \mu$m, $\mu = 10^4$ Pa s, and $B = 1.3 \times 10^{-12}$ N m we get the noise prefactor $\Gamma = 2.5 \times 10^{-13}$ m s$^{-1/2}$ and the energy ratio $N = 1.75 \times 10^{-6}$ which is well within the elastic-bending-dominated regime. However, a transition from a dominant elastohydrodynamic leveling to a dominant stochastic leveling would occur for a system with temperature $T_\mathrm{A} = 300$ K, membrane perturbation height $h_\mathrm{i} = 10$ nm, and radius $R_\mathrm{i} = 5\ \mu$m for a bending modulus B in the range of 10–100 $k_\mathrm{B}T_\mathrm{A}$ where $k_\mathrm{B}T_\mathrm{A} = 4 \times 10^{-21}$ N m, which corresponds to N in the range 0–8 [29].

We solve the dimensionless version of Eq. (1) numerically by using a finite element method, and we split it into three coupled equations for the bump profile $H(X,T) = \hat{H}(X,T) - \epsilon/h_\mathrm{i}$, the linearized curvature $\partial^2H(X,T)/\partial X^2$, and the bending pressure $\partial^4H(X,T)/\partial X^4$. These fields are discretized with linear elements and solved by using Newton's method from the FEniCS library [42]. For the deterministic case $N = 0$, an adaptive time-stepping routine has been used with an upper time-step limit of $\Delta T = 0.001$ and a discretization in space $\Delta X \in [0.001; 0.01]$. For the stochastic case $N > 0$, we have used a constant time step $\Delta T = 0.001$, together with a discretization in space $\Delta X = 0.0025$. At $T = 0$ we impose the initial condition $H(X, T = 0) = 1 - \tanh(50X^2)$. We further impose the following boundary conditions at the boundary $\partial\Omega$ of the numerical domain: $H(X \in \partial\Omega, T) = H(X \in \partial\Omega, 0)$, $\partial^2H(X \in \partial\Omega, T)/\partial X^2 = 0$, and $\partial^4H(X \in \partial\Omega, T)/\partial X^4 = 0$. The noise $\Theta(X,T)$ is introduced independently at each discrete position and time step by using the "random" class with the "randn" Gaussian subclass from the NUMPY library [43], with zero mean and a variance $1/(\Delta X\,\Delta T)$. We avoid negative values of $\hat{H}(X,T)$ (that might occur in the stochastic case due to the fluctuations), by imposing that, when $\hat{H}(X,T) < 10^{-6}$, it is put back to 10^{-6} as in Refs. [34,36]. To verify the predictions of Eq. (1), we construct an experimental setup which is described in the following section.

III. EXPERIMENTAL PROCEDURE

The experimental setup is composed of a fiber of polystyrene (PS) with a glass-transition temperature $T_{\mathrm{g,\,PS}} \approx 100\,^{\circ}\mathrm{C}$ deposited on a film of the same polymer supported on a silicon (Si) substrate. These samples are capped by a thin sheet of polysulfone (PSU) with $T_{\mathrm{g,\,PSU}} \approx 180\,^{\circ}\mathrm{C}$. Sample preparation is carried out as follows: PS fibers (with number-averaged molecular weight $M_{\mathrm{n}} = 15.8$ kg/mol and polydispersity index PDI = 1.05, Polymer Source Inc., Canada) are pulled from the melt at 175 °C by using a glass rod. Thin PS films are spin casted from a toluene solution onto 10×10 mm^2 Si substrates, leading to a thickness of 25 to 380 nm, as measured by using ellipsometry (Accurion, EP3). The films are annealed at 110 °C for at least 12 hours in vacuum to remove residual solvent and relax residual stresses. The PS fibers are then transferred onto the PS films and the ensemble is heated briefly above $T_{\mathrm{g,\,PS}}$. The heating allows the PS to flow, thereby resulting in a bump. Thin PSU films ($M_{\mathrm{n}} \approx 22$ kg/mol, Sigma-Aldrich) are prepared by spin casting from a cyclohexanone solution onto freshly cleaved mica substrates (Ted Pella, USA). The PSU films have a thickness of ≈160 nm, as measured by using ellipsometry, and are annealed in vacuum at 200 °C for at least 12 hours. The PSU films are floated on water and then transferred onto a supporting apparatus (described previously [44]), held only by the film edges. These freestanding films can be relaxed to an unstrained state, ensuring no in-plane tension. The PSU films are finally transferred onto the PS sample. The part of the PSU film at the edges of the Si wafer was then removed by using a scalpel blade prior to annealing. This was done to ensure slippage at the boundary between the PSU film and liquid PS layer, thus rendering the relaxation bending-dominated, as discussed above.

After preparation, the samples were annealed on a hotstage (Linkam, UK) at 130 °C, which is above $T_{\mathrm{g,\,PS}}$ but below $T_{\mathrm{g,\,PSU}}$. Hence, the PS becomes a viscous liquid while the capping PSU film remains an elastic solid, thus realizing the system illustrated in Fig. 1. The height profile is imaged during annealing by using optical microscopy with a red laser line filter ($\lambda = 632.8$ nm, Newport, USA), which creates interference fringes in the region of the bump, as shown in Fig. 2(a), due to the light that is reflected from the Si substrate. It is clear from these fringes that the initial fiber and resulting flow are one dimensional over length scales that are many times the width of the perturbation itself. Each interference fringe corresponds to a change in height of $\lambda/(4n)$, where $n \approx 1.57$ is the average index of refraction of the two polymers that make up the sample ($n_{\mathrm{PS}} = 1.53$ and $n_{\mathrm{PSU}} = 1.61$). This allows the bump profile $h(x,t)$ to be reconstructed by fitting a polynomial to the fringe data, as shown in Fig. 2(b). Such profiles can then be used to track the leveling dynamics, and to extract in particular the evolution of the height $h_0(t)$ of the bump with time for various initial geometries.

IV. RESULTS

A. Elastohydrodynamic leveling

We first start by investigating the elastohydrodynamic leveling in the absence of thermal fluctuations ($N = 0$). In Fig. 3 we show the numerical solutions of the dimensionless version of Eq. (1) for $N = 0$ and we can see that the aspect ratio h_{i}/ϵ controls both the timescale for leveling and the detailed features of the height profile. The smaller h_{i}/ϵ, the faster the dimensionless leveling process. Also, the dip created near the advancing front of the perturbation is enhanced both in magnitude and lateral extent for smaller h_{i}/ϵ. We remark that, for each initial aspect ratio, there is a transition period of a few numerical time steps preceding the onset of the leveling process. This part of the data is not included in Fig. 4 because it is considered to depend on the initial condition, but does not

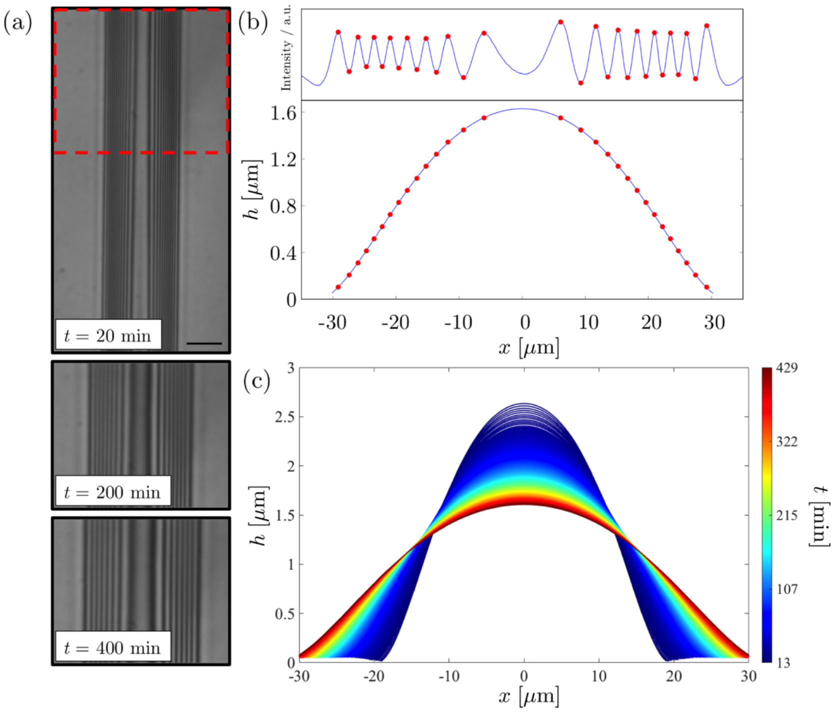

FIG. 2. (a) Typical optical microscopy images showing the temporal evolution of the interference fringes due to the liquid bump capped by the elastic plate (20 μm scale bar). The image at 20 minutes is uncropped, showing the invariance in the y direction, while the later images are cropped at the red box. (b) Intensity profile (averaged along the y direction) of the bump at a given time t, and corresponding reconstructed bump profile at 400 minutes. (c) Temporal evolution of the bump profile.

influence the later dynamics. For $h_\mathrm{i}/\epsilon = 43$, the numerical height profiles are further compared with our experiments, which are found to be in good agreement. We recall here that the elastic plate is floating on the liquid film and has edges that are free to move. Therefore, the pressure contribution from bending still largely dominates any contribution from stretching and Eq. (1) is still valid.

We now turn to a scaling analysis of Eq. (1) for $N = 0$. When $h_0(t)/\epsilon \ll 1$, the equation can be linearized and reduces to $12\mu\partial h/\partial t = B\epsilon^3\partial^6 h/\partial x^6$ as $\hat{h}(x,t) = h(x,t) + \epsilon$ and we deduce the long-term scaling for the temporal evolution of the horizontal length of the bump: $R(t) \sim [B\epsilon^3 t/(12\mu)]^{1/6}$. Since there is area conservation in the (x,z) plane, we assume $R(t)h_0(t)$ to be constant, that is evaluated to $R_\mathrm{i}h_\mathrm{i}$ at $t = 0$. By combining these scaling relations we get for $h_0(t)/\epsilon \ll 1$,

$$\frac{h_0(t)}{\epsilon} \sim \left(\frac{\tau}{t}\right)^{1/6}, \tag{2}$$

where $\tau = 12\mu h_\mathrm{i}^6 R_\mathrm{i}^6/(B\epsilon^9)$ is the characteristic timescale for the bending-driven leveling dynamics. Because we operate within the regime where bending dominates over stretching, a similar result is obtained by considering the force balance between the viscous and bending forces [18]. Also, if we include isotropic stretching due to clamped boundaries, a similar scaling law appears, but now with an additional logarithmic term, $R(t) \sim [t/\ln(t)]^{1/6}$ [19]. However, when $h_0(t)/\epsilon \gg 1$ we must match the curvature of a traveling-wave solution localized near the advancing front with the quasistatic solution to obtain the correct scaling [22], i.e., constant pressure in the bump, leading to [29]

$$\frac{h_0(t)}{\epsilon} \sim \left(\frac{\tau}{t}\right)^{2/17}. \tag{3}$$

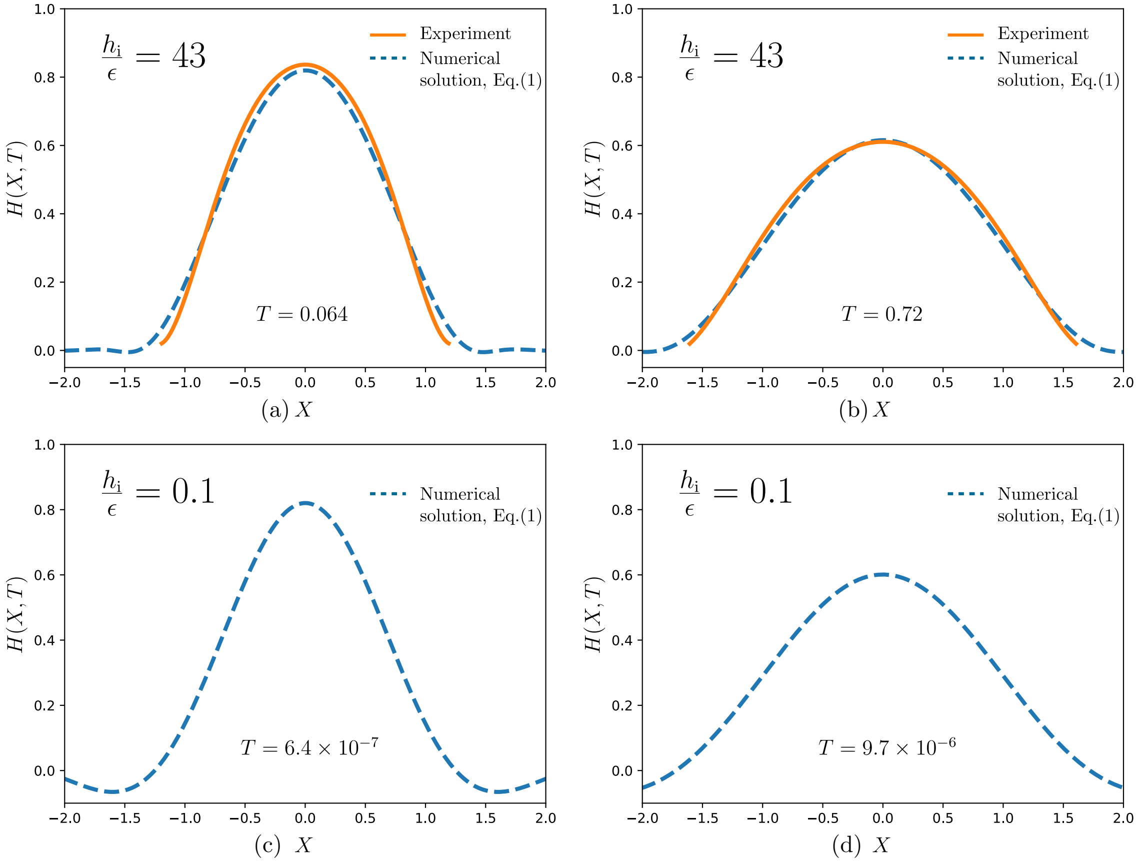

FIG. 3. (a), (b) Bump-height profiles for an initial aspect ratio $h_i/\epsilon = 43$, from a numerical solution of Eq. (1) and an experiment at two dimensionless times T as indicated, which correspond respectively to $t = 37$ min and $t = 416$ min. The geometrical parameters are $h_i = 2.9$ μm, $R_i = 16.5$ μm, and $\epsilon = 67$ nm. To account for the experimental uncertainties in the geometrical parameters, the experimental time t is divided by a free-fitting factor $\alpha = 0.13$. Note that, specifically for these figures, the initial condition for the numerical solution was fixed by a curve fitting of the actual experimental profile at $t = 13$ min. (c), (d) Bump-height profiles for an initial aspect ratio $h_i/\epsilon = 0.1$ from a numerical solution of Eq. (1) at two dimensionless times T, as indicated, chosen so that the central heights $H(X = 0, T)$ match those in the top row.

By balancing the two asymptotic predictions above, we expect the crossover between them to occur around $t/\tau \approx 1$. In addition, these asymptotic regimes suggest that $h_0(t)/\epsilon$ is essentially a function of t/τ only, independent of the value of h_i/ϵ.

To test our scaling predictions, we compute numerical solutions of the dimensionless version of Eq. (1) for $N = 0$, with $h_i/\epsilon \in [10^{-2}, 10^3]$, and extract $h_0(t)/\epsilon$ as a function of t/τ. These numerical results are plotted in Fig. 4 and compared with the experimental data. For each sample, the experimental data are matched to the numerical data through one fitting parameter α in front of the timescale τ. The values of the fluid viscosity and elastic Young's modulus are highly sensitive to the temperature in the experiments, and we estimate them to be $\mu \approx 10^4$ Pa s [45,46] and $E \approx 2.6$ GPa [47], respectively. Since all experiments were carried out at the same temperature and with the same polymer, sample-to-sample variations in τ result only from uncertainties in the geometrical parameters h_i, R_i, d, and ϵ. The α values obtained are 0.13, 0.7, and 1.3 for the three samples and each of these values are reasonably close to unity. More importantly, the sample-to-sample variations in α do not exceed a factor of ten, which is well within the expected relative error arising from the high sensitivity of τ to the geometrical parameters. The general agreement between the experimental data and the numerical predictions is good, over about five

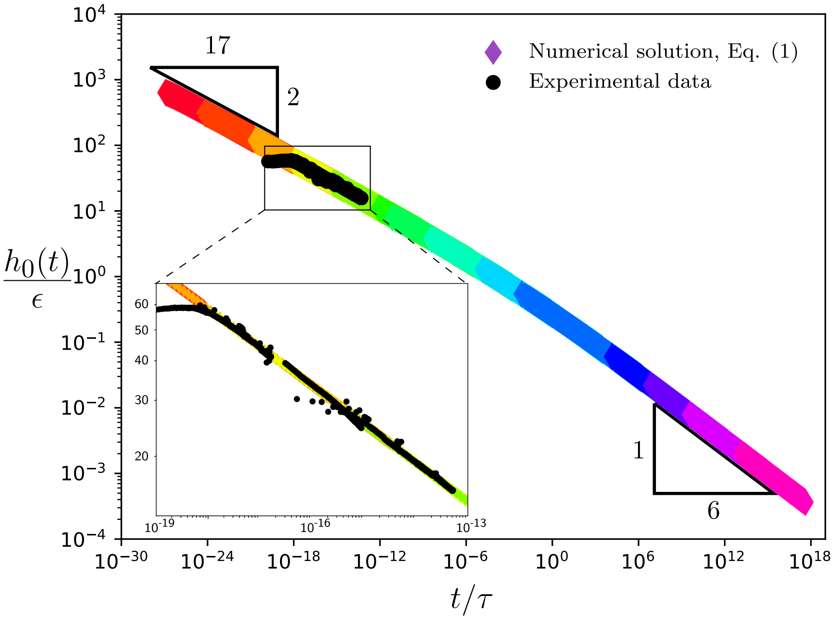

FIG. 4. Nondimensional bump height as a function of dimensionless time in the bending case, for various initial values of $h_\mathrm{i}/\epsilon \in [10^{-2}; 10^3]$. The colored diamond-shaped markers are rescaled data points from the numerical solutions of the dimensionless version of Eq. (1) with $N = 0$, and the black circle-shaped markers are scaled experimental data points. The exponents of the two asymptotic regimes of Eqs. (2) and (3) are indicated with triangles. The inset provides a zoom in the region containing the experimental data for the three samples, with initial aspect ratios $h_\mathrm{i}/\epsilon = 30, 43, 56$, corresponding respectively to $\epsilon = 50, 67, 26$ nm; $h_\mathrm{i} = 1.52, 2.9, 1.48$ μm; and $R_\mathrm{i} = 9.6, 16.5, 9.9$ μm. The uncertainties in all experimental length scales are about 5%. To compensate for those, the characteristic time τ for each sample is multiplied by a free-fitting factor $\alpha = 0.7, 0.13$, and 1.3, respectively.

orders of magnitude in t/τ. The systematic early time tail in the experimental data might be attributed to the initial compressive thermal stresses in the elastic layer, which arise due to the rapid heating of the samples from room temperature to $T = 130\,^\circ$C, which relax prior to leveling and the time needed for the initial shape to enter the asymptotic regime.

The master curve in Fig. 4 confirms that $h_0(t)/\epsilon$ is a function of t/τ. Furthermore, the two scaling regimes predicted above are indeed present, with prefactors close to unity, and the crossover between the two being located near $t/\tau \approx 1$ as predicted. Any bump that initially starts in a thin prewetted film regime $h_0(t)/\epsilon \gg 1$ will eventually cross over to a thick-film regime $h_0(t)/\epsilon \ll 1$, with the corresponding power laws in time. As a final remark, a similar combination (not included here) of numerical simulations and scaling analysis can be performed for an axisymmetric geometry, leading to $h_0(t) \sim t^{-2/11}$ for $h_\mathrm{i}/\epsilon \gg 1$, and $h_0(t) \sim t^{-1/3}$ for $h_\mathrm{i}/\epsilon \ll 1$.

B. Stochastic leveling

Next we investigate the leveling process when it is dominated by thermal fluctuations ($N > 0$). As shown in Fig. 5, the numerical solutions suggest that the aspect ratio h_i/ϵ is again essential, because it sets the timescale for leveling where the smaller h_i/ϵ, the faster the dimensionless leveling process. Moreover, by comparison with the deterministic ($N = 0$) case in Fig. 3, the stochastic ($N > 0$) profiles exhibit spatiotemporal fluctuations and adopt different average shapes and leveling dynamics.

To go further, we propose a scaling analysis of Eq. (1), inspired by Ref. [32]. We consider specifically the $N \gg 1$ limit, for which the thermal fluctuations are the dominant driving contribution to the dynamics and we assume that we can neglect the bending term so that Eq. (1) reduces

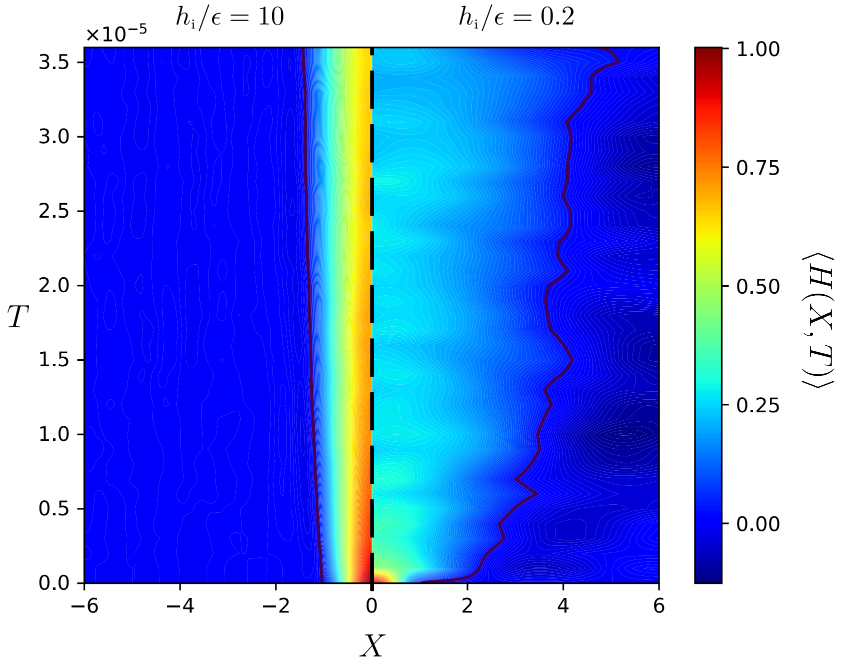

FIG. 5. Contour plot of the dimensionless bump-height profile $\langle H(X,T)\rangle$ as a function of both the dimensionless position X and time T, as obtained from numerical solutions of the dimensionless version (see text) of Eq. (1), with $N = 5$, and for $h_i/\epsilon = 10$ (left) or $h_i/\epsilon = 0.2$ (right). The thick solid lines indicate $\langle H(X,T)\rangle = 0.03$ as an arbitrary reference.

to $\partial h/\partial t = \Gamma\partial[(\epsilon + h)^{3/2}\eta]/\partial x$. We consider the average quantities $\langle h_0(t)\rangle$ and $\langle R(t)\rangle$, where we invoke the $\sim(tx)^{-1/2}$ scaling [34] for the root mean square value of the averaged noise over a space interval x and a time interval t. By assuming that the average area conservation in the (x, z) plane can be expressed as $\langle h_0(t)\rangle\langle R(t)\rangle \sim h_i R_i$, we get

$$\frac{\langle h_0(t)\rangle}{\epsilon}\left[1 + \frac{\langle h_0(t)\rangle}{\epsilon}\right]^3 \sim \frac{\tau_\Gamma}{t}, \tag{4}$$

where $\tau_\Gamma = 6\mu h_i^3 R_i^3 b/(k_B T_A \epsilon^4)$ is the characteristic timescale for the stochastic leveling dynamics. Interestingly, Eq. (4) describes a complete crossover between two asymptotic regimes in the stochastic leveling dynamics: for $\langle h_0(t)\rangle/\epsilon \gg 1$, we obtain $\langle h_0(t)\rangle/\epsilon \sim (\tau_\Gamma/t)^{1/4}$, and thus we recover $\langle h_0(t)\rangle \sim t^{-1/4}$ [34], while for $\langle h_0(t)\rangle/\epsilon \ll 1$, we get $\langle h_0(t)\rangle/\epsilon \sim \tau_\Gamma/t$. We expect the crossover between the two asymptotic regimes to occur around $\langle h_0(t)\rangle/\epsilon \approx 1$, i.e., around $t/\tau \approx 1/8$.

To test the prediction in Eq. (4), we compute the numerical solution of the dimensionless version of Eq. (1) for $5 \leqslant N \leqslant 8$, with $h_i/\epsilon \in [10^{-1}, 10^2]$. By averaging over a minimum of 30 realizations, we can extract $\langle h_0(t)\rangle/\epsilon$ as a function of t/τ_Γ, and the results are plotted in Fig. 6. The data from the numerical solutions are in good agreement with Eq. (4) for all $\langle h_0(t)\rangle/\epsilon$ and with no adjustable parameters. Our results highlight that Eq. (4) gives an accurate prediction of the stochastic leveling dynamics and show that the missing prefactor is close to unity. Finally, in order to further highlight the underlying self-similarity associated with each of the two asymptotic regimes, the insets of Fig. 6 show the corresponding bump-height profiles rescaled according to Eq. (4). In each asymptotic regime the height profiles collapse onto a universal shape which confirms the overall self-similarity in the leveling dynamics.

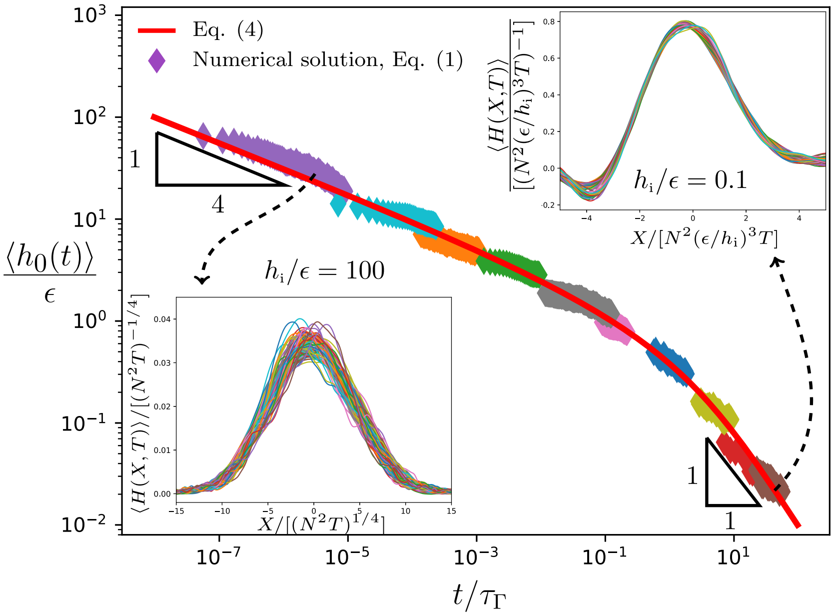

FIG. 6. Nondimensional bump height as a function of dimensionless time in the stochastic leveling dynamics, for different initial values of $h_\mathrm{i}/\epsilon \in [10^{-1}, 10^2]$. The colored diamond-shaped markers are rescaled data points from the numerical solutions of Eq. (1) with $5 \leqslant N \leqslant 8$. Each data set is an average from a minimum of 30 numerical solutions. The solid red line corresponds to Eq. (4) with a prefactor of order unity. The insets show rescaled bump-height profiles for $h_\mathrm{i}/\epsilon = 100$ with $T \in [1, 10] \times 10^{-3}$ (lower left) and for $h_\mathrm{i}/\epsilon = 0.1$ with $T \in [4, 4.6] \times 10^{-3}$ (upper right).

V. CONCLUSION

We have described the elastohydrodynamic and stochastic leveling of an elastic plate placed atop a viscous film. By combining numerical solutions, scaling analysis, and experiments, we identified various canonical regimes. Our results highlight the importance of the driving mechanism, either by elastic bending of the plate or by thermal fluctuations, and the influence of the aspect ratio of bump height to film height. For each of these two driving mechanisms, a crossover between two distinct asymptotic regimes is controlled by the aspect ratio. These findings can be helpful to explain elastohydrodynamic leveling dynamics found in biological, engineering, or geological processes.

ACKNOWLEDGMENTS

The financial support by the Research Council of Norway (project grant 263056), the Natural Sciences and Engineering Research Council of Canada, and the Joliot Chair of ESPCI Paris is gratefully acknowledged. The authors also thank Tak Shing Chan, Miroslav Kuchta, Corentin Mailliet, René Ledesma-Alonso, Maxence Arutkin, Elie Raphaël, Howard Stone, Pauline Olive, Katelyn Dixon, Paul Fowler, Mark Ilton and David Dean for interesting discussions and preliminary works in different geometries.

---

[1] N. J. Balmforth, R. V. Craster, and A. C. Rust, Instability in flow through elastic conduits and volcanic tremor, J. Fluid Mech. **527**, 353 (2005).
[2] C. Michaut, Dynamics of magmatic intrusions in the upper crust: Theory and applications to laccoliths on Earth and the Moon, J. Geophys. Res. **116**, B05205 (2011).

[3] T. V. Ball and J. A. Neufeld, Static and dynamic fluid-driven fracturing of adhered elastica, Phys. Rev. Fluids **3**, 074101 (2018).

[4] L. E. Bilston, D. F. Fletcher, A. R. Brodbelt, and M. A. Stoodley, Arterial pulsation-driven cerebrospinal fluid flow in the perivascular space: A computational model, Comput. Methods Biomech. Biomed. Eng. **6**, 235 (2003).

[5] D. Takagi and N. J. Balmforth, Peristaltic pumping of viscous fluid in an elastic tube, J. Fluid Mech. **672**, 196 (2011).

[6] R. Borcia, M. Bestehorn, S. Uhlig, M. Gaudet, and H. Schenk, Liquid pumping induced by transverse forced vibrations of an elastic beam: A lubrication approach, Phys. Rev. Fluids **3**, 084202 (2018).

[7] D. A. Sanchez, Z. Dai, P. Wang, A. Cantu-Chavez, C. J. Brennan, R. Huang, and N. Lu, Mechanics of spontaneously formed nanoblisters trapped by transferred 2D crystals, Proc. Natl. Acad. Sci. USA **115**, 7884 (2018).

[8] A. E. Hosoi and L. Mahadevan, Peeling, Healing, and Bursting in a Lubricated Elastic Sheet, Phys. Rev. Lett. **93**, 137802 (2004).

[9] R. Huang and Z. Suo, Wrinkling of a compressed elastic film on a viscous layer, J. Appl. Phys. **91**, 1135 (2002).

[10] T. T. Al-Housseiny, I. C. Christov, and H. A. Stone, Two-Phase Fluid Displacement and Interfacial Instabilities Under Elastic Membranes, Phys. Rev. Lett. **111**, 034502 (2013).

[11] I. J. Hewitt, N. J. Balmforth, and J. R. De Bruyn, Elastic-plated gravity currents, Eur. J. Appl. Math. **26**, 1 (2015).

[12] A. Tulchinsky and A. D. Gat, Transient dynamics of an elastic Hele-Shaw cell due to external forces with application to impact mitigation, J. Fluid Mech. **800**, 517 (2016).

[13] S. B. Elbaz and A. D. Gat, Axial creeping flow in the gap between a rigid cylinder and a concentric elastic tube, J. Fluid Mech. **806**, 580 (2016).

[14] M. Arutkin, R. Ledesma-Alonso, T. Salez, and E. Raphaël, Elastohydrodynamic wake and wave resistance, J. Fluid Mech. **829**, 538 (2017).

[15] A. Juel, D. Pihler-Puzović, and M. Heil, Instabilities in blistering, Annu. Rev. Fluid Mech. **50**, 691 (2018).

[16] M. Rivetti, V. Bertin, T. Salez, C. Y. Hui, C. Linne, M. Arutkin, H. Wu, E. Raphaël, and O. Bäumchen, Elastocapillary levelling of thin viscous films on soft substrates, Phys. Rev. Fluids **2**, 094001 (2017).

[17] E. Cerda and L. Mahadevan, Geometry and Physics of Wrinkling, Phys. Rev. Lett. **90**, 074302 (2003).

[18] H. Vandeparre, S. Gabriele, F. Brau, C. Gay, K. K. Parker, and P. Damman, Hierarchical wrinkling patterns, Soft Matter **6**, 5751 (2010).

[19] O. Kodio, I. M. Griffiths, and D. Vella, Lubricated wrinkles: Imposed constraints affect the dynamics of wrinkle coarsening, Phys. Rev. Fluids **2**, 014202 (2017).

[20] R. Bernal, C. Tassius, F. Melo, and J. C. Géminard, Elastic response and wrinkling onset of curved elastic membranes subjected to indentation test, Eur. Phys. J. E **34**, 13 (2011).

[21] F. Box, D. O'Kiely, O. Kodio, M. Inizan, A. A. Castrejón-Pita, and D. Vella, Dynamics of wrinkling in ultrathin elastic sheets, Proc. Natl. Acad. Sci. USA **116**, 20875 (2019).

[22] J. R. Lister, G. G. Peng, and J. A. Neufeld, Viscous Control of Peeling an Elastic Sheet by Bending and Pulling, Phys. Rev. Lett. **111**, 154501 (2013).

[23] M. Berhanu, A. Guérin, S. C. du Pont, F. Raoult, R. Perrier, and C. Michaut, Uplift of an elastic membrane by a viscous flow, Phys. Rev. E **99**, 043102 (2019).

[24] A. Carlson and L. Mahadevan, Similarity and singularity in adhesive elastohydrodynamic touchdown, Phys. Fluids **28**, 011702 (2016).

[25] W. W. Zhang and J. R. Lister, Similarity solutions for van der Waals rupture of a thin film on a solid substrate, Phys. Fluids **11**, 2454 (1999).

[26] D. Pihler-Puzović, A. Juel, G. G. Peng, J. R. Lister, and M. Heil, Displacement flows under elastic membranes. Part 1. Experiments and direct numerical simulations, J. Fluid Mech. **784**, 487 (2015).

[27] M. Heil and A. L. Hazel, Fluid-structure interaction in internal physiological flows, Annu. Rev. Fluid Mech. **43**, 141 (2011).

[28] G. K. Batchelor, *An Introduction to Fluid Dynamics* (Cambridge University Press, New York, 2000).

[29] A. Carlson, Fluctuation assisted spreading of a fluid filled elastic blister, J. Fluid Mech. **846**, 1076 (2018).

[30] L. H. Tanner, The spreading of silicone oil drops on horizontal surfaces, J. Phys. D: Appl. Phys. **12**, 1473 (1979).

[31] P. G. De Gennes, Wetting: Statics and dynamics, Rev. Mod. Phys. **57**, 827 (1985).

[32] S. L. Cormier, J. D. McGraw, T. Salez, E. Raphaël, and K. Dalnoki-Veress, Beyond Tanner's Law: Crossover Between Spreading Regimes of a Viscous Droplet on an Identical Film, Phys. Rev. Lett. **109**, 154501 (2012).

[33] N. Bergemann, A. Juel, and M. Heil, Viscous drops on a layer of the same fluid: From sinking, wedging and spreading to their long-time evolution, J. Fluid Mech. **843**, 1 (2018).

[34] B. Davidovitch, E. Moro, and H. A. Stone, Spreading of Viscous Fluid Drops on a Solid Substrate Assisted by Thermal Fluctuations, Phys. Rev. Lett. **95**, 244505 (2005).

[35] V. Démery and D. S. Dean, Perturbative path-integral study of active- and passive-tracer diffusion in fluctuating fields, Phys. Rev. E **84**, 011148 (2011).

[36] S. Nesic, R. Cuerno, E. Moro, and L. Kondic, Fully nonlinear dynamics of stochastic thin-film dewetting, Phys. Rev. E **92**, 061002 (2015).

[37] S. Marbach, D. S. Dean, and L. Bocquet, Transport and dispersion across wiggling nanopores, Nat. Phys. **14**, 1108 (2018).

[38] L. D. Landau and E. M. Lifshitz, *Course of Theoretical Physics Vol 7: Theory and Elasticity* (Pergamon Press, Oxford, 1959).

[39] G. Grün, K. Mecke, and M. Rauscher, Thin-film flow influenced by thermal noise, J. Stat. Phys. **122**, 1261 (2006).

[40] M. A. Durán-Olivencia, R. S. Gvalani, S. Kalliadasis, and G. A. Pavliotis, Instability, rupture and fluctuations in thin liquid films: Theory and computations, J. Stat. Phys. **174**, 579 (2019).

[41] S. Nesic, R. Cuerno, E. Moro, and L. Kondic, Dynamics of thin fluid films controlled by thermal fluctuations, Eur. Phys. J. Spec. Top. **224**, 379 (2015).

[42] A. Logg, K. A. Mardal, and G. Wells, *Automated Solution of Differential Equations by the Finite Element Method: The FEniCS Book* (Springer Science & Business Media, Berlin, 2012), Vol. 84.

[43] T. Oliphant, *NumPy: A guide to NumPy* (Trelgol Publishing, 2006).

[44] R. D. Schulman, J. F. Niven, M. A. Hack, C. DiMaria, and K. Dalnoki-Veress, Liquid dewetting under a thin elastic film, Soft Matter **14**, 3557 (2018).

[45] J. D. McGraw, T. Salez, O. Bäumchen, E. Raphaël, and K. Dalnoki-Veress, Self-Similarity and Energy Dissipation in Stepped Polymer Films, Phys. Rev. Lett. **109**, 128303 (2012).

[46] M. Ilton, M. M. P. Couchman, C. Gerbelot, M. Benzaquen, P. D. Fowler, H. A. Stone, E. Raphaël, K. Dalnoki-Veress, and T. Salez, Capillary Leveling of Freestanding Liquid Nanofilms, Phys. Rev. Lett. **117**, 167801 (2016).

[47] *Springer Handbook of Condensed Matter and Materials Data*, edited by W. Martienssen and H. Warlimont (Springer, New York, 2005).

3.3 Paper III

The transition from local wrinkling to global buckling in thin free-standing bilayer films

John F. Niven, Gurkaran Chowdhry, James S. Sharp, and Kari Dalnoki-Veress. Submitted to *The European Physical Journal E*, October 2019. Manuscript ID: e190215.

This paper studied mechanical instabilities in free-standing bilayers consisting of a rigid PS film and a soft elastomeric substrate, Elastosil. The substrate was prestrained up to 25 % and then capped by the rigid film. Upon release of the strain the bilayer either underwent local wrinkling or global buckling, where the entire bilayer deformed out-of-plane. It was found that the phase boundary between the two instabilities depends both on the thickness ratio of the films and the pre-strain in the substrate. A simple model inspired by wrinkling theory for a semi-infinite substrate was developed to describe the phase boundary, and shows agreement with experiments. This result is of significance for the design of thin flexible electronics. A novel buckled delamination structure was also observed for very thin substrates.

I designed the experiment in collaboration with Dr. Dalnoki-Veress. I performed the majority of the wrinkling/buckling experiments with assistance from undergraduate student Gurkaran Chowdhry. The theoretical model was developed by Dr. Dalnoki-Veress with assistance from myself and Dr. James Sharp. I wrote the original version of the manuscript and contributed to editing subsequent versions.

EPJ manuscript No.
(will be inserted by the editor)

The transition from local wrinkling to global buckling in thin free-standing bilayer films

John F. Niven[1], Gurkaran Chowdhry[1], James S. Sharp[2], and Kari Dalnoki-Veress[1,3,a]

[1] Department of Physics & Astronomy, McMaster University, Hamilton, Ontario, L8S 4M1, Canada
[2] School of Physics and Astronomy, University of Nottingham, University Park, Nottingham, NG7 2RD, UK
[3] UMR CNRS Gulliver 7083, ESPCI Paris, PSL Research University, 10 rue Vauquelin, 75005 Paris, France

January 29, 2020

Abstract Periodic wrinkling of a rigid capping layer on a deformable substrate provides a useful method for templating surface topography for a variety of novel applications. Many experiments have studied wrinkle formation during the compression of a rigid film on a relatively soft pre-strained elastic substrate, and most have focused on the regime where the substrate thickness can be considered semi-infinite relative to that of the film. As the relative thickness of the substrate is decreased, the bending stiffness of the film dominates, causing the bilayer to transition from local wrinkling to a global buckling instability. In this work optical microscopy was used to study the critical parameters that determine the transition between local wrinkling and global buckling of free-standing bilayer films consisting of a thin rigid polymer capping layer on a pre-strained elastomeric substrate. The thickness ratio of the film and substrate as well as the pre-strain were controlled and used to create a buckling phase diagram which describes the behaviour of the system as the ratio of the thickness of the substrate is decreased. A simple force balance model was developed to understand the thickness and strain dependences of the wrinkling and buckling modes, with excellent quantitative agreement being obtained with experiments using only independently measured material parameters.

1 Introduction

Wrinkling and buckling of thin films have been thoroughly investigated for a variety of applications such as small-scale surface patterning [1–3], biomedical devices [4], and flexible electronics [5]. One way to achieve surface patterns is by capping a soft, stretchable substrate, such as an elastomer (elastic modulus $E_\mathrm{s} \sim$ MPa) with a relatively thin rigid layer, such as a metallic or polymeric film ($E_\mathrm{f} \sim$ GPa). If the rigid layer becomes sufficiently compressed it can buckle locally out of plane with a sinusoidal wrinkling pattern in order to accommodate its excess surface area relative to the compressed substrate. Compression can be achieved through either differential thermal expansion [6], chemical swelling [7–9], or by mechanically pre-straining the substrate prior to capping with the rigid film [10–13].

Mechanically induced buckling, shown schematically in fig. 1, is most relevant for biomedical devices and flexible and wearable electronics applications, where the use of high temperatures or chemical swelling should be avoided [5,14,15]. In these systems it is critical to understand how mechanical instabilities and failure modes depend on the geometry of the bilayer and the material properties of the individual layers. Most experiments to date have focused on macroscopic samples, where the thickness of the substrate, H, is taken to be infinite relative to the thickness of the capping film, h. Following release of the pre-strain, these systems can form either 1D or 2D wrinkling patterns [13]. At higher strains, localization features such as folds and creases [3,16–18], period doubling [19], or delaminations can occur. In the latter case, voids have been shown to form between the film and substrate [20–22]. In this semi-infinite regime, the wavelength of wrinkling, λ, can be calculated using a force balance between the bending of the capping film and the deformation of the substrate [10]. This force balance results in a wrinkle wavelength:

$$\lambda = 2\pi h \left(\frac{\bar{E}_\mathrm{f}}{3\bar{E}_\mathrm{s}}\right)^{1/3}, \tag{1}$$

where $\bar{E}_i = E_i/(1-\nu_i^2)$ is the plane strain modulus of layer i, with E_i the Young's modulus and ν_i the Poisson's ratio, where subscript $i = f$ or s refers to the capping film or substrate, respectively. This wavelength is linearly dependent on the thickness of the capping film, while being independent of the substrate thickness. This relationship has been proven exhaustively by experiments [1,10] and allows wrinkling in the semi-infinite regime to be used as a method for measuring the moduli of thin rigid films [11,23–25]. There is also a critical pre-strain, $\epsilon_{\mathrm{c},\infty}$, required for wrinkling in the semi-infinite regime, which is

---

[a] e-mail: `dalnoki@mcmaster.ca`

dependent only on the ratio of the moduli of the materials:

$$\epsilon_{c,\infty} = \frac{1}{4}\left(\frac{3\bar{E}_s}{\bar{E}_f}\right)^{2/3} . \tag{2}$$

Below this critical pre-strain the capping film remains flat upon compression. For typical elastomer/polymer material pairs this critical pre-strain is on the order of 0.5 % [3,21].

When considering applications such as flexible electronics or biomedical applications, technology continues to push for ever smaller structures and feature sizes, requiring bilayer films in which the thickness of the substrate can no longer be considered semi-infinite. In this finite-substrate regime it has been suggested both theoretically [26–28] and experimentally [29] that wrinkling wavelengths can deviate from those predicted by eq. 1, and that this could affect device performance. Crucially, when the bending stiffness of the capping film becomes dominant, the entire bilayer film could undergo global buckling on a length scale similar to the total sample length, as shown schematically in fig. 1(b), similar to observations in refs. [30] and [31]. The critical conditions that separate local wrinkling and global buckling in bilayer films have been studied both theoretically and experimentally in the context of flexible electronics using macroscopic samples [26,27,32]. These works have developed theories to predict the type of instability observed, and have predicted that the critical pre-strain required for wrinkling increases as the relative thickness of the substrate is decreased, although experimental results are limited.

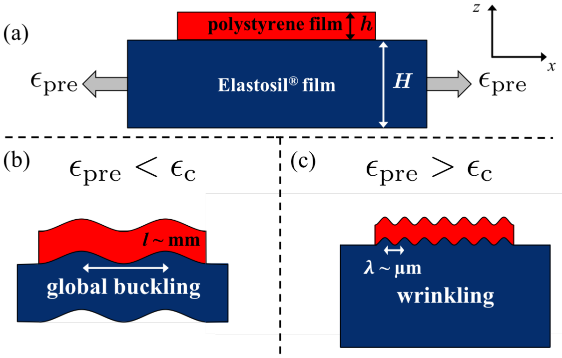

Figure 1. (a) Side view schematic of an elastomeric film pre-strained by an amount ϵ_{pre} and capped by a thin polystyrene film. (b) Below a critical pre-strain the bilayer will undergo buckling. (c) Above the critical pre-strain the rigid film will wrinkle.

In this work we present a novel experiment to study the critical geometrical parameters which separate local wrinkling and global buckling in thin free-standing bilayer films. The use of a free-standing geometry means that the entire bilayer sample is able to deform out of plane, allowing for global buckling to occur. By varying the thickness ratio of the capping film and substrate, h/H, and the substrate pre-strain, ϵ_{pre}, the wrinkling to global-buckling phase-space can be mapped out. We also present a model that has been adapted from the semi-infinite theory in order to produce a simple description of the transition between wrinkling and global buckling which is in good quantitative agreement with experiments.

2 Experimental Methods

Bilayer films were prepared on a biaxial straining apparatus shown schematically in fig. 2 and described previously [33,34]. The apparatus consisted of a 258 ± 2 μm thick Elastosil® sheet (Wacker Chemie AG, Poisson's ratio for the substrate is taken to be $\nu_s = 0.5$ making the reasonable assumption that the elastomer is incompressible, $E_s = 1.11 \pm 0.06$ MPa [35]) cut into a rounded "plus" shape, with a 1 cm diameter hole in the middle. This shape was chosen to ensure nearly uniform biaxial strain at the centre of the hole where the bilayer sample is placed. Each arm of the film was clamped to a post and attached to crossed optical rails using translation stages. The hole was covered with a second Elastosil film (the "substrate" of the bilayer) with thicknesses of H = {20.9 ± 0.4 (measured here), 51 ± 1, 104 ± 2, 213 ± 7, or 258 ± 2} μm [35]. Samples with intermediate substrate thickness were made by stacking Elastosil sheets with good adhesion between the films – sufficient that the films remained in good contact when strained. The 0 % strain value was calibrated before each experiment by adjusting each post until the point just before the Elastosil sheet begins to wrinkle. The substrate was then strained biaxially by moving two of the translation stages in opposite directions (the high-strain direction) while leaving the perpendicular direction fixed. The applied pre-strain was measured optically using $\epsilon_{\mathrm{pre}} = (d_f - d_i)/d_i$, where d_i and d_f are the initial and final distances between two defects in the film surface aligned parallel to the strain direction, respectively. The posts perpendicular to the applied strain were not adjusted, meaning that the strain in the perpendicular direction is zero. We note that while there is no strain in the perpendicular direction, there is a tensile stress induced through Poisson's ratio which is smaller than that induced in the high-strain direction.

Films of polystyrene (PS, with weight average molecular weight M_w = 183 kg mol^{-1} and polydispersity index, PDI = 1.06, Polymer Source Canada, Poisson's ratio $\nu_f = 0.33$ [36] and modulus E_f = 3.3 GPa [36]) with thickness values ranging from $h \approx 80 - 1900$ nm were prepared by spin coating from dilute toluene solution onto freshly cleaved mica substrates and their thickness measured using ellipsometry (Accurion, EP3). We note that the modulus of PS at these thicknesses should remain at the bulk value [24]. All films were annealed in vacuum at 140 °C for a minimum of several hours to relax the polymer chains and remove any residual solvent. The films were then cut into ∼3 mm × 3 mm pieces using a scalpel and floated off the mica and onto the surface of an ultrapure water bath (18.2 MΩ·cm, Pall, Cascada, LS). A piece of the PS film was then floated back onto the mica

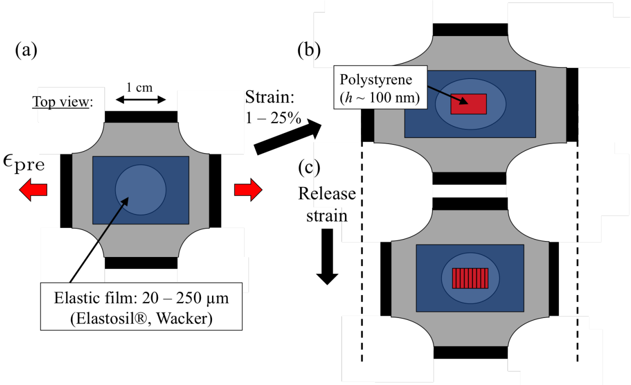

Figure 2. (a) Top view schematic of the experimental straining setup showing the rounded plus sign 250 μm Elastosil film with a hole in the middle. The hole is covered with a second free-standing Elastosil film of varying thickness, which acts as the substrate. (b) The substrate is strained biaxially and capped with a thin PS film, forming a bilayer. (c) As strain is released and the bilayer is compressed, it can either wrinkle or buckle.

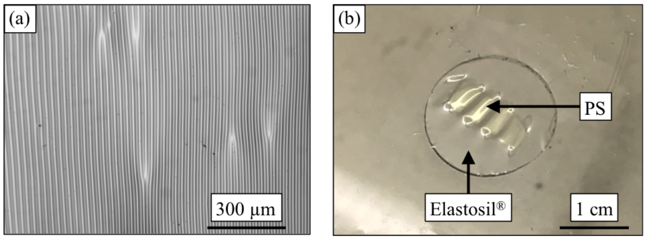

Figure 3. (a) Optical microscopy image of wrinkles in a PS/Elastosil bilayer. The wrinkling wavelength varies between 1 - 100 μm depending on the capping film thickness. (b) Optical image of a buckled bilayer film with a length scale ~mm.

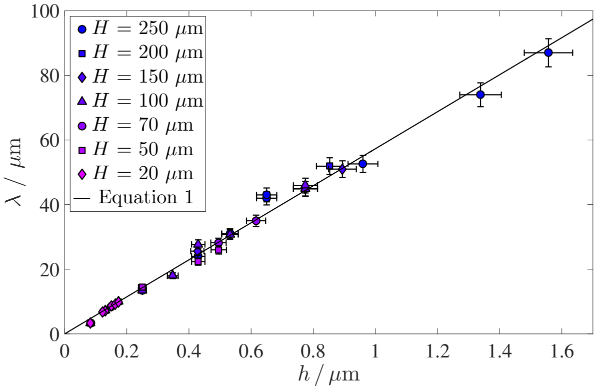

Figure 4. Wrinkling wavelength, λ, as a function of the capping film thickness, h, for a range of substrate thicknesses, H, for pre-strains up to 25 % and $3.4\times10^{-4} < h/H < 8.7\times10^{-3}$. The solid line corresponds to the semi-infinite theory, eq. 1, with no fitting parameters.

substrate, and brought into contact with the Elastosil substrate. The strong adhesion between the PS and Elastosil means that the mica substrate can be removed, resulting in a free-standing PS/Elastosil bilayer. Any remaining water is gently wicked away at the edge of the sample. The pre-strain is then slowly released by moving the translation stages, and the bilayer film can be observed using optical microscopy as the capping film is compressed by the relaxing substrate. An important feature to note with this setup is that the bilayer film is free-standing in the region of the hole, so the entire film is free to deform out of plane of the compression.

3 Results and Discussion

Wrinkling was observed in this system with wavelengths ranging between 1 μm and 100 μm (as shown in fig. 3(a)), as measured using optical microscopy. Figure 4 shows the measured wavelengths as a function of the rigid capping film thickness, h, for substrate thicknesses ranging from $H = 20$ μm to 250 μm for strains up to 25 %, as well as a line corresponding to the semi-infinite model, eq. 1. We can see that, even with different substrate film thicknesses, the data is in excellent agreement with the semi-infinite model with no fitting parameters in the value of the slope, only independently measured moduli and Poisson's ratios of the capping film and elastic substrate. This result indicates that, provided that wrinkling is observed, for these materials at pre-strains between 1 – 25 %, the semi-infinite model is valid for $3.4\times10^{-4} < h/H < 8.7\times10^{-3}$.

For a given pair of materials, the semi-infinite wrinkling regime exists for low thickness ratios, $h/H \approx 1\times10^{-3}$, and above the critical strain. At a fixed pre-stain, as h/H is increased there is a critical value at which the observed instability upon release of the strain changes from local wrinkling, as seen in fig. 3(a), to global buckling instability (shown in fig. 3(b)), with a length scale on the order of the total sample length.

In order to obtain a quantitative understanding of the critical conditions that separate local wrinkling and global buckling in this system, we develop a simple model beginning with a force balance between the bending of the rigid capping film and the deformation of the substrate [37]. Similar derivations have been shown in the literature previously, but here we present the derivation alongside that for buckling for completeness [10,38,39]. The force balance in the bilayer can be written in the form:

$$\bar{E}_{\rm f} I_{\rm f} z'''' + \bar{E}_{\rm s}\frac{wq}{2}z + F_{\rm w}z'' = 0, \tag{3}$$

where the first term considers the bending of the PS film, the second describes the forces in the substrate and the final term deals with the in-plane forces in the PS film that are generated by the release of the pre-strain in the substrate.

The deformation of the top surface of the bilayer is given by:

$$z(x) = A\sin qx, \tag{4}$$

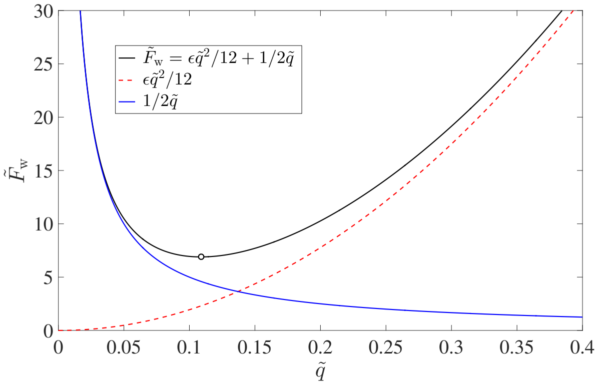

Figure 5. Plot of eq. 6 showing the non-dimensional force, $\tilde{F}_\mathrm{w}$, required for wrinkling as a function of the non-dimensional wavenumber $\tilde{q} = qh$, shown in black. The dashed red line and the blue line represent the first and second term on the RHS of eq. 6. The black circle shows the minimum's force required for wrinkling, $\tilde{F}_\mathrm{w,\ c}$.

where $q = 2\pi/\lambda$ is the wavenumber. Primes in eq. 3 denote derivatives with respect to the in-plane direction x, $I_\mathrm{f} = wh^3/12$ is the inertial moment of the capping film of thickness h and width w, and F_w is the force applied to the capping film which causes wrinkling. Differentiating eq. 4 and substituting into eq. 3 gives:

$$\frac{F_\mathrm{w}}{w} = \frac{\bar{E}_\mathrm{f} h^3 q^2}{12} + \frac{\bar{E}_\mathrm{s}}{2q}. \tag{5}$$

This equation can be simplified by non-dimensionalizing as follows: $\tilde{F}_\mathrm{w} \equiv \frac{F_\mathrm{w}}{wh\bar{E}_\mathrm{s}}$, $\tilde{\lambda} \equiv \frac{\lambda}{h}$, $\tilde{q} \equiv qh$, $\tilde{H} \equiv \frac{H}{h}$, $\gamma \equiv \frac{\bar{E}_\mathrm{f}}{\bar{E}_\mathrm{s}}$, which results in the following condition for wrinkling:

$$\tilde{F}_\mathrm{w} = \frac{\gamma\tilde{q}^2}{12} + \frac{1}{2\tilde{q}}. \tag{6}$$

Equation 6 can be minimized to get the relevant critical values for wrinkling:

$$\tilde{q}_\mathrm{c} = \left(\frac{3}{\gamma}\right)^{1/3}, \tag{7}$$

$$\tilde{\lambda}_\mathrm{c} = 2\pi\left(\frac{\gamma}{3}\right)^{1/3}, \tag{8}$$

$$\text{and } \tilde{F}_\mathrm{w,c} = \frac{3}{4}\left(\frac{\gamma}{3}\right)^{1/3}. \tag{9}$$

Figure 5 shows a plot of the critical force required for wrinkling, eq. 6, including the two terms, as a function of $\tilde{q}$. The critical force for wrinkling is shown as a circle.

The criterion for wrinkling is simply that the pre-strain in the substrate is such that the force applied to the capping film, F_pre, is enough to overcome the critical force $F_\mathrm{w,c}$. If there is not sufficient force on the capping film then the bilayer can only buckle or remain flat. As the strain is relaxed, the force due to the pre-strain increases slowly and reaches a maximum when the substrate pre-strain in the region outside of the capping film is a minimum. Thus the wrinkling criterion now becomes $F_\mathrm{pre} = F_\mathrm{w,c}$. The maximum force resulting from the initial pre-strain (i.e. when there is full relaxation of the uncapped region of the substrate) is given by $F_\mathrm{pre} = \epsilon_\mathrm{pre} wH\bar{E}_\mathrm{s}$, since $\epsilon = \frac{\sigma}{\bar{E}_s} = \frac{F}{Hw\bar{E}_s}$. Therefore: $F_\mathrm{pre} = \epsilon_\mathrm{pre} wH\bar{E}_\mathrm{s} = F_\mathrm{w,c} = \tilde{F}_\mathrm{w,c} wh\bar{E}_\mathrm{s}$, which results in:

$$h = \frac{4}{3}\cdot\left(\frac{3\bar{E}_\mathrm{s}}{\bar{E}_\mathrm{f}}\right)^{1/3}\epsilon_\mathrm{pre} H. \tag{10}$$

Instead of taking the maximum force as resulting from the applied pre-strain alone, we recognize that even with zero applied pre-strain the act of transferring the PS capping film onto the free-standing substrate membrane causes it to deform, which induces an additional pre-strain that remains after the bilayer is formed. To test this, a bilayer was made with “0 %” applied strain using the same calibration technique as all other experiments. When compressed, the sample had regions of clear wrinkling throughout, which is only possible if there was indeed a small pre-strain induced from the sample preparation process. Additionally, there is some uncertainty in the true “0 %” pre-strain value because the boundary between a tensile strain and compressive strain was determined by the appearance of small wrinkles in the substrate by eye. If we assume that this induced deformation is consistent between experiments, the total strain in the substrate is then: $\epsilon_\mathrm{total} = \epsilon_\mathrm{pre} + \epsilon_0$, where ϵ_0 is a small additional pre-strain resulting from the transfer of the PS film. It then follows that $F_\mathrm{pre} = (\epsilon_\mathrm{pre} + \epsilon_0)wHE_\mathrm{s}$. Balancing this with the force required for wrinkling gives the following criterion for wrinkling:

$$h = \frac{4}{3}\cdot\left(\frac{3\bar{E}_\mathrm{s}}{\bar{E}_\mathrm{f}}\right)^{1/3}(\epsilon_\mathrm{pre} + \epsilon_0)\,H. \tag{11}$$

Experiments were carried out for various substrate and capping film thickness and at various pre-strain values. The experimental strain offset was measured to be $\epsilon_0 = 2.3$ %. Figure 6 shows the phase diagram of wrinkling and buckling at a fixed applied pre-strain value of 3 % (total pre-strain of 5.3 %) for various capping film and substrate thicknesses. Wrinkles dominate at low values of h/H (the semi-infinite regime), and buckles become dominant for higher values of h/H. There is a clear linear transition between wrinkling and buckling, with the straight line corresponding to eq. 11. This plot shows excellent agreement between the data and theory given that there are no fitting parameters, only material properties.

Equation 11 can be rewritten instead as the critical pre-strain required for wrinkling:

$$\epsilon_\mathrm{pre} + \epsilon_0 = \frac{3}{4}\cdot\left(\frac{\bar{E}_\mathrm{f}}{3\bar{E}_\mathrm{s}}\right)^{1/3}\cdot\frac{h}{H}, \tag{12}$$

which deviates from the critical value in the semi-infinite regime, eq. 2, in that the finite regime value depends inversely on the substrate thickness. We note the slope of

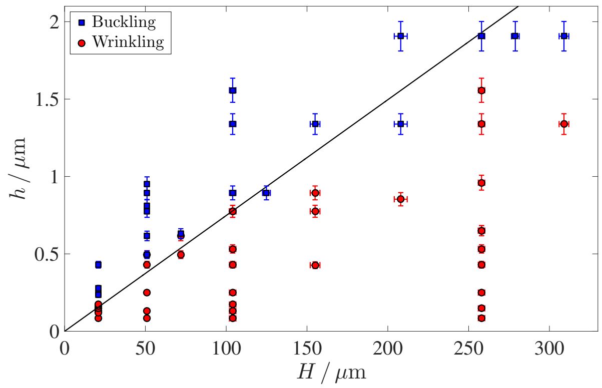

Figure 6. Phase diagram of wrinkling (red circles) and buckling (blue squares) for various substrate and cap thickness at a fixed value of $\epsilon_{\rm pre} = 3$ % (total pre-strain of $\epsilon_{\rm pre} + \epsilon_0 = 5.3$ %). The solid line corresponds to the theoretical transition between wrinkling and buckling, eq. 11, with no fitting parameters.

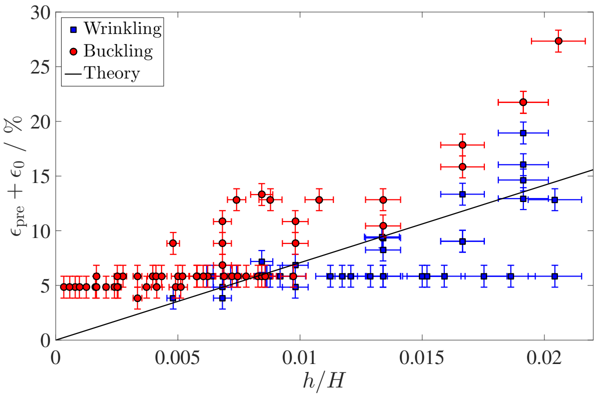

Figure 7. Phase diagram of wrinkling (red circles) and buckling (blue squares) for various film thickness ratios, h/H, as a function of the full applied pre-strain $\epsilon_{\rm pre} + \epsilon_0$. The solid line corresponds to the theoretical transition between wrinkling and buckling, eq. 12, with no fitting parameters.

eq. 12 is similar to the theory presented in ref. [32], which uses a more complex energy balance to find the transition between pure local wrinkling and a mixed local/global buckling mode, however the slope predicted in that work is higher and does not agree well with the experimental slope measured here.

Figure 7 shows the wrinkling and buckling phase diagram now with total pre-strain on the vertical axis and film thickness ratio h/H on the horizontal axis. It is clear from this plot that for larger values of h/H the system can be made to transition from buckling to wrinkling by increasing the pre-strain in the substrate, which increases the compressive force applied to the capping films. The solid line corresponds to eq. 12 and contains no fitting parameters. As this equation describes the transition from wrinkling to buckling in the bilayer samples, all data points below the line should correspond to samples that have buckled and those above the line to wrinkled samples. As the figure shows, there is excellent agreement between the theory and the experimental data for a wide range of thickness ratios and pre-strain values. There is significant uncertainty at low strains near the transition because samples would often show partial wrinkling, where only some of the area had wrinkled, which made distinguishing between the two regimes difficult. At pre-strains above 20 % delaminations were found to become dominant as the buckling energy of the capping film overcame the adhesion energy between the films. This regime was not the focus of this study.

4 Observed Delamination Morphologies

While the delamination regime is beyond the scope of this manuscript, it is worth noting some of the morphologies that were observed, even if the results presented are merely observational. It was found that interesting morphologies could be observed for high pre-strains in the semi-infinite regime, which included creases, folds, period doubling, and delamination. Novel post-delamination buckling morphologies have also been found under certain conditions, including “varicose” or “bubble” blisters [40, 41], and “telephone cord” blisters [42–44]. To study the effect of high strain in the finite substrate regime, bilayers with thickness ratios of order 1 were made using a different elastomeric film, Elastollan TPU 1185A (BASF). Elastollan films were prepared by spin coating from dilute cyclohexanone solution with thicknesses of ∼1 μm. An Elastollan film was transferred onto the straining setup and strained biaxially by 15 %. The film was then capped with a 500 nm thick PS film as before. Upon compression, large scale global buckling of the entire bilayer was observed first (fig. 1a). On further compression the PS film delaminated from the substrate, with delaminations forming across the entire width of the sample perpendicular to the compression axis. The delaminations were observed both optically and using atomic force microscopy (AFM) to scan the PS/air and Elastollan/air interfaces. Prior to taking AFM scans, the sample was transferred to a thin stainless steel washer. Elastollan is adhesive enough that the film remained in good contact with the washer without losing strain, and the washer is thin enough that the sample can simply be flipped in order to image both interfaces. A scan of the two interfaces shows that the delamination ridge is only present at the PS/air interface, meaning there is a void between the two films.

Due to the Poisson’s ratio of the pre-strained elastomer there is also an initial tension in the elastic film orthogonal to the pre-strain direction, which cannot be relaxed while the film and substrate remain in good contact [34]. However, as the delaminations grow, contact is lost between the two films, and the substrate is now free to relax its excess length along the delaminated regime while remaining in contact along the edges. This geometry results in an instability with a periodic structure along the length of the

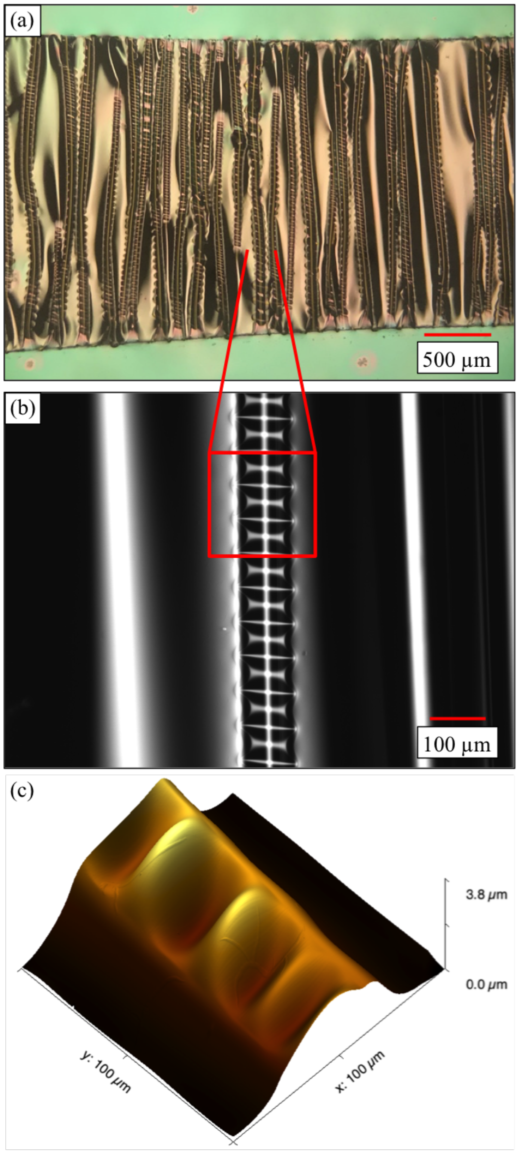

Figure 8. (a) Optical microscopy image showing "zipper" delaminations in a bilayer consisting of a 1 μm Elastollan film capped with a 500 nm PS film. (b) Zoomed in optical microscopy image in reflection mode showing the periodic structure of a zipper delamination. (c) AFM image of the Elastollan/air interface of a "zipper" delamination showing the periodic structure

delamination, seen optically in fig. 8(a) and (b). The structure was studied in more detail using AFM (fig. 8(c)) and showed that the periodic pattern is caused by wrinkling in the elastomer layer, while the PS film remains in its one-dimensional delaminated structure without buckling significantly in the perpendicular direction. The observed pattern is reminiscent of the "bubble" delaminations seen previously [40,41], and provides a novel technique for templating free-standing films.

5 Conclusions

In conclusion, we have observed the transition between wrinkling and buckling in free-standing rigid/elastic bilayer films for which the substrate thickness cannot be taken as semi-infinite. We have shown that the critical pre-strain for wrinkling depends on film/substrate thickness ratio, h/H. A simple force balance model was used to predict the critical criteria required for wrinkling, which matches well with the experimental data using only independently measured material parameters. This model deviates from semi-infinite theory in that it has a dependence on the substrate thickness. These results provide experimental insights into design considerations for flexible electronics and other applications with thin elastic substrates.

Financial support was provided by the National Sciences and Engineering Research Council (NSERC). The authors thank Wacker Chemie AG for donating the Elastosil® material. JSS would like to acknowledge the support of the University of Nottingham's International Collaboration Fund.

Author contribution statement

JN and KDV designed the research project, JN and GC performed all experiments and analyzed the data, JN, JS and KDV developed the theoretical model, JN wrote the first draft of the manuscript, and all authors edited the manuscript to generate a final version and contributed to the discussion throughout the entire process of the research.

References

1. J. Genzer, J. Groenewold, Soft Matter **2**, 310 (2006)
2. A. Chiche, C.M. Stafford, J.T. Cabral, Soft Matter **4**, 2360 (2008)
3. Y.C. Chen, A.J. Crosby, Adv. Mater. **26**, 5626 (2014)
4. Y. Liu, M. Pharr, G.A. Salvatore, ACS Nano **11**, 9614 (2017)
5. J.A. Rogers, T. Someya, Y. Huang, Science **327**, 1603 (2010)
6. N. Bowden, S. Brittain, A.G. Evans, J.W. Hutchinson, G.M. Whitesides, Nature **393**, 146 (1998)
7. E.P. Chan, A.J. Crosby, Soft Matter **2**, 324 (2006)
8. E.P. Chan, A.J. Crosby, Adv. Mater. **18**, 3238 (2006)
9. D. Breid, A.J. Crosby, Soft Matter **7**, 4490 (2011)
10. A.L. Volynskii, S. Bazhenov, O.V. Lebedeva, N.F. Bakeev, J. Mater. Sci. **35**, 547 (2000)
11. C.M. Stafford, C. Harrison, K.L. Beers, A. Karim, E.J. Amis, M.R. VanLandingham, H.C. Kim, W. Volksen, R.D. Miller, E.E. Simonyi, Nat. Mater. **3**, 545 (2004)
12. K. Efimenko, M. Rackaitis, E. Manias, A. Vaziri, L. Mahadevan, J. Genzer, Nat. Mater. **4**, 293 (2005)
13. P.C. Lin, S. Yang, Appl. Phys. Lett. **90**, 241903 (2007)
14. Y. Sun, V. Kumar, I. Adesida, J. Rogers, Advanced Materials **18**, 2857 (2006)

15. M. Kaltenbrunner, T. Sekitani, J. Reeder, T. Yokota, K. Kuribara, T. Tokuhara, M. Drack, R. Schwödiauer, I. Graz, S. Bauer-Gogonea et al., Nature **499**, 458 EP (2013)
16. L. Pocivavsek, R. Dellsy, S. Johnson, B. Lin, K.Y.C. Lee, E. Cerda, Science **320**, 912 (2008)
17. F. Brau, P. Damman, H. Diamant, T.A. Witten, Soft Matter **9**, 8177 (2013)
18. Q. Wang, X. Zhao, Sci. Rep. **5**, 8887 (2015)
19. F. Brau, H. Vandeparre, A. Sabbah, C. Poulard, A. Boudaoud, P. Damman, Nat. Phys. **7**, 56 (2010)
20. H. Mei, R. Huang, J.Y. Chung, C.M. Stafford, H.H. Yu, Appl. Phys. Lett. **90**, 151902 (2007)
21. Y. Ebata, A.B. Croll, A.J. Crosby, Soft Matter **8**, 9086 (2012)
22. A.J. Nolte, J. Young Chung, C.S. Davis, C.M. Stafford, Soft Matter **13**, 7930 (2017)
23. C.M. Stafford, S. Guo, C. Harrison, M.Y.M. Chiang, Rev. Sci. Instrum. **76**, 062207 (2005)
24. C.M. Stafford, B.D. Vogt, C. Harrison, D. Julthongpiput, R. Hunag, Macromolecules **38**, 5095 (2006)
25. J.Y. Chung, A.J. Nolte, C.M. Stafford, Adv. Mater. **23**, 349 (2011)
26. S. Wang, J. Song, D.H. Kim, Y. Huang, J.A. Rogers, Appl. Phys. Lett. **93**, 023126 (2008)
27. Y. Ma, Y. Xue, K.I. Jang, X. Feng, J.A. Rogers, Y. Huang, Proc. Royal Soc. A **472**, 20160339 (2016)
28. X. Meng, G. Liu, Z. Wang, S. Wang, Appl. Math. Mech. **38**, 469 (2017)
29. D.C. Hyun, U. Jeong, J. Appl. Polym. Sci. **112**, 2683 (2009)
30. A. Takei, F. Brau, B. Roman, J. Bico, Europhys. Lett. **96**, 64001 (2011)
31. A. Concha, J.W. McIver, P. Mellado, D. Clarke, O. Tchernyshyov, R.L. Leheny, Phys. Rev. E **75**, 016609 (2007)
32. Y. Ma, K.I. Jang, L. Wang, H.N. Jung, J.W. Kwak, Y. Xue, H. Chen, Y. Yang, D. Shi, X. Feng et al., Adv. Funct. Mater. **26**, 5345 (2016)
33. B. Davis-Purcell, P. Soulard, T. Salez, E. Raphaël, K. Dalnoki-Veress, Eur. Phys. J. E **41**, 36 (2018)
34. R.D. Schulman, J.F. Niven, M.A. Hack, C. DiMaria, K. Dalnoki-Veress, Soft Matter **14**, 3557 (2018)
35. J.C. Ono-dit Biot, M. Trejo, E. Loukiantcheko, M. Lauch, E. Raphaël, K. Dalnoki-Veress, T. Salez, Phys. Rev. Fluids **4**, 014808 (2019)
36. J. Brandup, E. Immergut, G. EA, eds., *Polymer Handbook*, Vol. 49, 4th edn. (Wiley and Sons, New York, 1999)
37. L.D. Landau, E.M. Liftshitz, *Theory of Elasticity*, 3rd edn. (Butterworth-Heinemann, New York, USA, 1986)
38. M. Biot, Journal of Applied Mechanics p. A1 (1937)
39. H. Allen, *Analysis and Design of Structural Sandwich Panels*, 1st edn. (Pergamon, 1969)
40. M. George, C. Coupeau, J. Colin, F. Cleymand, J. Grilhé, Philos. Mag. A **82**, 633 (2002)
41. B. Audoly, B. Roman, A. Pocheau, Eur. Phys. J. B **27**, 7 (2002)
42. B. Audoly, Phys. Rev. Lett. **83**, 4124 (1999)
43. M.W. Moon, K.R. Lee, K. Oh, J. Hutchinson, Acta Mater. **52**, 3151 (2004)
44. Y. Ni, S. Yu, H. Jiang, L. He, Nat. Commun. **8**, 14138 (2017)

Chapter 4

Conclusions

The work presented in this thesis focused on viscous and elastic thin polymer films in unstable configurations. The systems studied involved the vertical symmetrization and viscous flow of a thin free-standing polymer film with initially asymmetric interfaces, fluid perturbations driven to flow by the bending energy of a rigid membrane, and mechanical instabilities in free-standing bilayers of a thin rigid film and soft elastomeric substrate.

In Paper I, a novel atomic force microscopy technique was developed to study flow in free-standing films. A nano-scale film was prepared with micrometer diameter holes partially through the film, meaning that the top interface had high excess surface area while the bottom interface had zero excess surface area. Since flow in this system is driven purely by surface tension, the system flowed to decrease its excess surface area, thus decreasing its excess surface energy. By tracking the surface profiles it was therefore possible to track the total free energy of the system as it evolved. It was shown that at early times the film flowed vertically to symmetrize the Laplace pressure at the two interfaces. This result is unique, because typically in thin film flow experiments it is assumed that flow horizontal to the plane of the film dominates vertical flows (the lubrication approximation), which is clearly untrue at early times in this system. During the symmetrization process there is an exchange of free energy between the two interfaces, with the excess surface energy of the bottom actually increasing while it forms a second, symmetric hole. However, throughout the symmetrization process the total excess surface energy of the system decreased. A hydrodynamic model was developed by collaborators which showed excellent agreement the experiments.

In Paper II, the viscous flow of a 2D perturbation on thin polymer film was coupled with the bending energy of a rigid capping layer. In this system flow was no longer driven by reducing the excess surface area of the perturbation, but by minimizing the bending energy of the capping film. In order to reduce the bending energy, the fluid perturbation spread and flattened with time. The surface profiles were measured as a function of time using an optical interferometry technique, which allowed for the height and width of the profile to be tracked as a function of time. It was found that the height and width evolved with self-similar $t^{2/17}$ behaviour, which matched theoretical predictions.

In Paper III, a free-standing bilayer system consisting of a rigid polymer film and soft pre-strained elastomeric substrate was used to study the transition between local wrinkling and global buckling. It was shown that the type of instability observed in the system depended strongly on the relative thickness of the two films, the modulus ratio, and the pre-strain in the substrate. A simple theory based on the critical compressive force required for wrinkling was developed, and showed quantitative agreement with the experimental results. This work provides important insights for the design of applications based on rigid film/elastomeric substrate bilayers.

There are various extensions to this work, some of which are currently undergoing preliminary investigations. Following Paper I, the ability to using atomic force microscopy to simultaneously study the two interfaces of the same free-standing polymer film provides an opportunity to perform several unique experiments. For example, a follow-up study could be done to confirm the viscosity and thickness dependence of the symmetrization time predicted by the theory. It would also be of interest to study the evolution of holes in free-standing films for which the polymer molecules were confined. Despite significant effort to do this, the thin films required were found to be extremely prone to rupture, and the surface profile becomes difficult to resolve using AFM as the hole depth decreases, making measurements difficult. With the addition of a full theory of the symmetrization process, it is now possible that enough information could be extracted at early times to show confinement effects, such as through a significant change in the rate of symmetrization with decreasing film thickness, which would suggest a change in the capillary velocity of the film, and thus a change in viscosity, upon confinement.

A logical follow-up to Paper II would be studying the scaling regime in which the height of the perturbation was small in comparison with the pre-wet film thickness. On the opposite length scale, the experimental contribution of thermal fluctuations could be studied. Also, continuing the study of interactions between fluids and thin polymer films, a thin rigid film on a viscous substrate can wrinkle when the system is heated due to a compressive strain generated in the film due to differences in thermal expansion coefficients of the film and fluid. An interesting result occurs if a sample is prepared in a similar way to that presented in Paper II, in which a fluid hemicylinder on a silicon substrate is capped by a rigid thin film, but without the presence of a prewet fluid layer. In this case, the capping film is pinned at the edges of the cylinder, and if compression of the rigid film becomes sufficient, buckling instabilities can occur in the capping layer. The curvature in the region of the cylinder means that sinusoidal wrinkling is not necessarily the lowest energy state. Preliminary experiments have shown a range of possible patterns, including wrinkling, with the wavevector aligned parallel to the fibre axis, a dimpled pattern, and a "zig-zag" pattern. The type of patter observed depends strongly on the thickness of the capping film and the curvature of the cylinder. Finite element modelling and molecular dynamics simulations of this system are currently being preformed by Dr. Teng Zhang at the University of Syracuse, and preliminary results show good qualitative agreement with experiments.

As shown with the "zipper" delaminations in Paper III, there is the potential for further study of high strain elastic instabilities in bilayer systems for which the capping film thickness and substrate thickness become comparable. These novel structures could be of interesting for applications such as flexible electronic devices and surface patterning.

As has been shown through this thesis, thin polymer films, either glassy or in the melt, are an excellent experimental tool to study the physics of surface tension, viscosity, and elasticity, or their interplay.

Other Contributions

Paper AI

Liquid dewetting under a thin elastic film

Rafael D. Schulman, John F. Niven, Michiel A. Hack, Christian DiMaria and Kari Dalnoki-Veress, *Soft Matter*, **14** 3557–3562 (2018).

This project investigated the dewetting of thin polystyrene films that were capped by strained elastomer sheets. The tension in the elastomer caused the dewing ridge to flatten and widen relative to that of an uncapped film, resulting in a decreasing dewetting speed with increasing tension. Anisotropic tension in the elastomer was found to lead to non-circular dewetting regions. Dewetting was also studied in a free-standing geometry, where a PS film was capped at each surface by strained elastomer films. When the films were strained at 90° relative to one another, it was found that square dewetting regions formed.

These experiments were developed by Christian DiMaria and Dr. Rafael Schulman under the supervision of Dr. Kari Dalnoki-Veress, with preliminary data collected by Michiel Hack. The majority of data collection and analysis was done by Dr. Rafael Schulman. I was involved with performing atomic force microscopy measurements of the dewetted holes throughout the project. Special care was required to use AFM with these samples because of the strong adhesion between the elastomeric film and AFM tip in comparison with a glassy surface, and because the freestanding elastomeric samples were sensitive to vibrations. I also provided input and editorial assistance throughout the manuscript preparation process.

Bibliography

[1] G.-J. N. Wang, A. Gasperini, and Z. Bao. Stretchable polymer semiconductors for plastic electronics. *Advanced Electronic Materials*, 4(2):1700429, 2018.

[2] T. P. Russell and Y. Chai. 50th anniversary perspective: Putting the squeeze on polymers: A perspective on polymer thin films and interfaces. *Macromolecules*, 50(12):4597–4609, 2017.

[3] J. A. Forrest, K. Dalnoki-Veress, J. R. Stevens, and J. R. Dutcher. Effect of free surfaces on the glass transition temperature of thin polymer films. *Phys. Rev. Lett.*, 77:2002–2005, 1996.

[4] J. A. Forrest, K. Dalnoki-Veress, and J. R. Dutcher. Interface and chain confinement effects on the glass transition temperature of thin polymer films. *Phys. Rev. E*, 56:5705–5716, 1997.

[5] H. Bodiguel and C. Fretigny. Reduced viscosity in thin polymer films. *Phys. Rev. Lett.*, 97:266105, 2006.

[6] Z. Fakhraai and J. A. Forrest. Measuring the surface dynamics of glassy polymers. *Science*, 319(5863):600–604, 2008.

[7] T. Salez, J. Salez, K. Dalnoki-Veress, E. Raphaël, and J. A. Forrest. Cooperative strings and glassy interfaces. *Proc. Natl. Acad. Sci. U.S.A*, 112(27):8227–8231, 2015.

[8] J. M. Torres, C. M. Stafford, and B. D. Vogt. Impact of molecular mass on the elastic modulus of thin polystyrene films. *Polymer*, 51(18):4211–4217, 2010.

[9] M. Ilton, M. M. P. Couchman, C. Gerbelot, M. Benzaquen, P. D. Fowler, H. A. Stone, E. Raphaël, K. Dalnoki-Veress, and T. Salez. Capillary leveling of free-standing liquid nanofilms. *Phys. Rev. Lett.*, 117:167801, 2016.

[10] E. P. Chan and A. J. Crosby. Fabricating microlens arrays by surface wrinkling. *Adv. Mater.*, 18(24):3238–3242, 2006.

[11] D. P. Holmes and A.J. Crosby. Snapping surfaces. *Advanced Materials*, 19(21):3589–3593, 2007.

[12] D. J. Lipomi, B. C.-K. Tee, M. Vosgueritchian, and Z. Bao. Stretchable organic solar cells. *Adv. Mater.*, 23(15):1771–1775, 2011.

[13] C. S. Davis and A. J. Crosby. Mechanics of wrinkled surface adhesion. *Soft Matter*, 7:5373–5381, 2011.

[14] D.-Y. Khang, H. Jiang, Y. Huang, and J. A. Rogers. A stretchable form of single-crystal silicon for high-performance electronics on rubber substrates. *Science*, 311(5758):208–212, 2006.

[15] J. A. Rogers, T. Someya, and Y. Huang. Materials and mechanics for stretchable electronics. *Science*, 327(5973):1603–1607, 2010.

[16] M. Kaltenbrunner, T. Sekitani, J. Reeder, T. Yokota, K. Kuribara, T. Tokuhara, M. Drack, R. Schwödiauer, I. Graz, S. Bauer-Gogonea, S. Bauer, and T. Someya. An ultra-lightweight design for imperceptible plastic electronics. *Nature*, 499:458–463, 2013.

[17] T. Yokota, P. Zalar, M. Kaltenbrunner, H. Jinno, N. Matsuhisa, H. Kitanosako, Y. Tachibana, W. Yukita, M. Koizumi, and T. Someya. Ultraflexible organic photonic skin. *Sci. Adv.*, 2(4), 2016.

[18] M. Heil and A. L. Hazel. Fluid-structure interaction in internal physiological flows. *Annu. Rev. Fluid Mech.*, 43(1):141–162, 2011.

[19] N. J. Balmforth, R. V. Craster, and A. C. Rust. Instability in flow through elastic conduits and volcanic tremor. *J. Fluid Mech.*, 527:353–377, 2005.

[20] M. Boncheva and G. M. Whitesides. Making things by self-assembly. *MRS Bull.*, 30(10):736–742, 2005.

[21] C. Py, P. Reverdy, L. Doppler, J. Bico, B. Roman, and C. N. Baroud. Capillary origami: Spontaneous wrapping of a droplet with an elastic sheet. *Phys. Rev. Lett.*, 98:156103, 2007.

[22] S. H. Tawfick, J. Bico, and S. Barcelo. Three-dimensional lithography by elasto-capillary engineering of filamentary materials. *MRS Bull.*, 41(2):108–114, 2016.

[23] J. Genzer and J. Groenewold. Soft matter with hard skin: From skin wrinkles to templating and material characterization. *Soft Matter*, 2(4):310, 2006.

[24] H. Kim, S.-M. Park, and W. D. Hinsberg. Block copolymer based nanostructures: Materials, processes, and applications to electronics. *Chem. Rev.*, 110(1):146–177, 2010.

[25] M. Rubenstein and R. H. Colby. *Polymer Physics.* Oxford University Press, 2003.

[26] M. G. Dunbar, B. M. Novak, and K. Schmidt-Rohr. Trans content in atactic polystyrene estimated by double-quantum solid-state NMR. *Solid State Nucl. Magn. Reson.*, 12(2):119–137, 1998.

[27] J. P. Cotton, D. Decker, H. Benoit, B. Farnoux, J. Higgins, G. Jannink, R. Ober, C. Picot, and J. des Cloizeaux. Conformation of polymer chain in the bulk. *Macromolecules*, 7(6):863–872, 1974.

[28] K. Dalnoki-Veress, J. A. Forrest, C. Murray, C. Gigault, and J. R. Dutcher. Molecular weight dependence of reductions in the glass transition temperature of thin, freely standing polymer films. *Phys. Rev. E*, 63:031801, 2001.

[29] R. A. L. Jones. *Soft condensed matter.* Oxford University Press, 2002.

[30] C. Donati, J. F. Douglas, W. Kob, S. J. Plimpton, P. H. Poole, and S. C. Glotzer. Stringlike cooperative motion in a supercooled liquid. *Phys. Rev. Lett.*, 80:2338–2341, 1998.

[31] M. Doi and S. F. Edwards. Dynamics of concentrated polymer systems. Part 1. Brownian motion in the equilibrium state. *J. Chem. Soc., Faraday Trans. 2*, 74:1789–1801, 1978.

[32] P. G. de Gennes. Reptation of a polymer chain in the presence of fixed obstacles. *J. Chem. Phys.*, 55(2):572–579, 1971.

[33] S. T. Milner and T. C. B. McLeish. Reptation and contour-length fluctuations in melts of linear polymers. *Phys. Rev. Lett.*, 81:725–728, 1998.

[34] R. H. Colby, L. J. Fetters, and W. W. Graessley. The melt viscosity-molecular weight relationship for linear polymers. *Macromolecules*, 20(9):2226–2237, 1987.

[35] L. J. Fetters, D. J. Lohse, S. T. Milner, and W. W. Graessley. Packing length influence in linear polymer melts on the entanglement, critical, and reptation molecular weights. *Macromolecules*, 32(20):6847–6851, 1999.

[36] J. D. McGraw, T. Salez, O. Bäumchen, E. Raphaël, and K. Dalnoki-Veress. Self-similarity and energy dissipation in stepped polymer films. *Phys. Rev. Lett.*, 109:128303, 2012.

[37] J. E. Marks, editor. *Physical Properties of Polymers Handbook*. American Institute of Physics, 1996.

[38] A. Marchand, J. H. Weijs, J. H. Snoeijer, and B. Andreotti. Why is surface tension a force parallel to the interface? *Am. J. Phys.*, 79(10):999–1008, 2011.

[39] P. de Gennes, F. Brochard-Wyart, and D. Quèrè. *Capillarity and Wetting Phenomena: Drops, Bubbles, Pearls, Waves*, volume 1. Springer, 2003.

[40] J. N. Isrealachvili. *Intermolecular and Surface Forces*. Academic Press, 3rd edition, 2011.

[41] G. T. Dee and B. B. Sauer. The molecular weight and temperature dependence of polymer surface tension: Comparison of experiment with interface gradient theory. *J. Colloid Interface Sci.*, 152(1):85–103, 1992.

[42] G. T. Dee and B. B. Sauer. The surface tension of polymer liquids. *Macromol. Symp.*, 139(1):115–123, 1999.

[43] S. Wu. Surface and interfacial tensions of polymer melts. ii. poly(methyl methacrylate), poly(n-butyl methacrylate), and polystyrene. *J. Phys. Chem.*, 74(3):632–638, 1970.

[44] D. G. Legrand and G. L. Gaines. The molecular weight dependence of polymer surface tension. *J. Colloid Interface Sci.*, 31(2):162–167, 1969.

[45] K. Jacobs, S. Herminghaus, and K. R. Mecke. Thin liquid polymer films rupture via defects. *Langmuir*, 14(4):965–969, 1998.

[46] A. Oron, S. H. Davis, and S. G. Bankoff. Long-scale evolution of thin liquid films. *Rev. Mod. Phys.*, 69:931–980, 1997.

[47] T. Salez, J. D. McGraw, O. Bäumchen, K. Dalnoki-Veress, and E. Raphaël. Capillary-driven flow induced by a stepped perturbation atop a viscous film. *Phys. Fluids*, 24(10):102111, 2012.

[48] M. Ilton, T. Salez, P. D. Fowler, M. Rivetti, M. Aly, M. Benzaquen, J. D. McGraw, E. Raphaël, K. Dalnoki-Veress, and O. Bäumchen. Adsorption-induced slip inhibition for polymer melts on ideal substrates. *Nat. Commun.*, 9(1):1172, 2018.

[49] P. G. de Gennes. Wetting: statics and dynamics. *Rev. Mod. Phys.*, 57:827–863, 1985.

[50] D. Bonn, J. Eggers, J. Indekeu, J. Meunier, and E. Rolley. Wetting and spreading. *Rev. Mod. Phys.*, 81(2):739–805, 2009.

[51] G. Reiter. Dewetting of thin polymer films. *Phys. Rev. Lett.*, 68:75–78, 1992.

[52] C. Redon, F. Brochard-Wyart, and F. Rondelez. Dynamics of dewetting. *Phys. Rev. Lett.*, 66:715–718, 1991.

[53] M. P. Brenner and D. Gueyffier. On the bursting of viscous films. *Phys. Fluids*, 11(3):737–739, 1999.

[54] F. E. C. Culick. Comments on a ruptured soap film. *J. Appl. Phys.*, 31(6):1128–1129, 1960.

[55] G. Debrégeas, P. Martin, and F. Brochard-Wyart. Viscous bursting of suspended films. *Phys. Rev. Lett.*, 75:3886–3889, 1995.

[56] K. Dalnoki-Veress, B. G. Nickel, and J. R. Dutcher. Hole formation and growth in freely standing polystyrene films. *Phys. Rev. E*, 59(2):2153–2156, 1999.

[57] C. B. Roth and J. R. Dutcher. Hole growth as a microrheological probe to measure the viscosity of polymers confined to thin films. *J. Poly. Sci. B*, 44(20):3011–3021, 2006.

[58] C. B. Roth and J. R. Dutcher. Hole growth in freely standing polystyrene films probed using a differential pressure experiment. *Phys. Rev. E*, 72:021803, 2005.

[59] E. Ruckenstein and R. K. Jain. Spontaneous rupture of thin liquid films. *J. Chem. Soc., Faraday Trans. 2*, 70:132–147, 1974.

[60] J. M. Rathfon, R. W. Cohn, A. J. Crosby, and G. N. Tew. Hole nucleation and growth in free-standing polystyrene ultrathin films. *Macromolecules*, 44(1):134–139, 2011.

[61] J. H. Xavier, Y. Pu, C. Li, M. H. Rafailovich, and J. Sokolov. Transition of linear to exponential hole growth modes in thin free-standing polymer films. *Macromolecules*, 37(4):1470–1475, 2004.

[62] M. Backholm, M. Benzaquen, T. Salez, E. Raphaël, and K. Dalnoki-Veress. Capillary levelling of a cylindrical hole in a viscous film. *Soft Matter*, 10:2550–2558, 2014.

[63] J. D. McGraw, N. M. Jago, and K. Dalnoki-Veress. Capillary levelling as a probe of thin film polymer rheology. *Soft Matter*, 7:7832–7838, 2011.

[64] M. Benzaquen, P. Fowler, L. Jubin, T. Salez, K. Dalnoki-Veress, and E. Raphaël. Approach to universal self-similar attractor for the levelling of thin liquid films. *Soft Matter*, 10:8608–8614, 2014.

[65] O. Bäumchen, M. Benzaquen, T. Salez, J. D. McGraw, M. Backholm, P. Fowler, E. Raphaël, and K. Dalnoki-Veress. Relaxation and intermediate asymptotics of a rectangular trench in a viscous film. *Phys. Rev. E*, 88(3):035001, 2013.

[66] J. D. McGraw, T. Salez, O. Bäumchen, E. Raphaël, and K. Dalnoki-Veress. Capillary leveling of stepped films with inhomogeneous molecular mobility. *Soft Matter*, 9:8297, 2013.

[67] Y. Chai, T. Salez, J. D. McGraw, M. Benzaquen, K. Dalnoki-Veress, E. Raphaël, and J. A. Forrest. A direct quantitative measure of surface mobility in a glassy polymer. *Science*, 343(6174):994–999, 2014.

[68] M. Rivetti, V. Bertin, T. Salez, C.-Y. Hui, C. Linne, M. Arutkin, H. Wu, E. Raphaël, and O. Bäumchen. Elastocapillary levelling of thin viscous films on soft substrates. *Phys. Rev. Fluids*, 2(9):094001, 2017.

[69] L. H. Tanner. The spreading of silicone oil drops on horizontal surfaces. *J. Phys. D*, 12(9):1473, 1979.

[70] A. M. Cazabat and M. A. Cohen Stuart. Dynamics of wetting: effects of surface roughness. *J. Phys. Chem.*, 90(22):5845–5849, 1986.

[71] J.-D. Chen and N. Wada. Wetting dynamics of the edge of a spreading drop. *Phys. Rev. Lett.*, 62:3050–3053, 1989.

[72] B. Davidovitch, E. Moro, and H. A. Stone. Spreading of viscous fluid drops on a solid substrate assisted by thermal fluctuations. *Phys. Rev. Lett.*, 95(24):244505, 2005.

[73] S. Nesic, R. Cuerno, E. Moro, and L. Kondic. Dynamics of thin fluid films controlled by thermal fluctuations. *Eur. Phys. J. Special Topics*, 224(2):379–387, 2015.

[74] L. D. Landau and E. M. Lifshitz. *Theory of Elasticity*, volume 7. Pergamon Press, 1970.

[75] S. P. Timoshenko and S. Woinowsky-Krieger. *Theory of plates and shells.* McGraw-Hill, 2nd edition, 1959.

[76] E. J. Kramer and L. L. Berger. Fundamental processes of craze growth and fracture. In H.-H. Kausch, editor, *Crazing in Polymers*, volume 2, pages 1–68, Berlin, Heidelberg, 1990. Springer Berlin Heidelberg.

[77] J. G. Drobny. *Handbook of Thermoplastic Elastomers*. Plastics Design Library. William Andrew Publishing, Norwich, NY, 2007.

[78] J. Bico, E. Reyssat, and B. Roman. Elastocapillarity: When surface tension deforms elastic solids. *Annu. Rev. Fluid Mech.*, 50(1):629–659, 2018.

[79] B. Roman and J. Bico. Elasto-capillarity: deforming an elastic structure with a liquid droplet. *J. Phys. Condens. Matter*, 22(49):493101, 2010.

[80] R. Pericet-Cámara, A. Best, H.-J. Butt, and E. Bonaccurso. Effect of capillary pressure and surface tension on the deformation of elastic surfaces by sessile liquid microdrops: An experimental investigation. *Langmuir*, 24(19):10565–10568, 2008.

[81] P. Martin and F. Brochard-Wyart. Dewetting at soft interfaces. *Phys. Rev. Lett.*, 80:3296–3299, 1998.

[82] R. D. Schulman, J. F. Niven, M. A. Hack, C. DiMaria, and K. Dalnoki-Veress. Liquid dewetting under a thin elastic film. *Soft Matter*, 14(18):3557–3562, 2018.

[83] R. D. Schulman and K. Dalnoki-Veress. Liquid droplets on a highly deformable membrane. *Phys. Rev. Lett.*, 115(20):206101, 2015.

[84] R. D. Schulman, R. Ledesma-Alonso, T. Salez, E. Raphaël, and K. Dalnoki-Veress. Liquid droplets act as "compass needles" for the stresses in a deformable membrane. *Phys. Rev. Lett.*, 118(19):198002, 2017.

[85] J. Bico, B. Roman, L. Moulin, and A. Boudaoud. Elastocapillary coalescence in wet hair. *Nature*, 432(7018):690–690, 2004.

[86] D. Chandra and S. Yang. Capillary-force-induced clustering of micropillar arrays: Is it caused by isolated capillary bridges or by the lateral capillary meniscus interaction force? *Langmuir*, 25(18):10430–10434, 2009.

[87] M. Mastrangeli, S. Abbasi, C. Varel, C. Van Hoof, J.-P. Celis, and K. F. Böhringer. Self-assembly from milli- to nanoscales: methods and applications. *J. Micromech. Microeng.*, 19(8):83001–83001, 2009.

[88] A. Fortais, R. D. Schulman, and K. Dalnoki-Veress. Liquid droplets on a free-standing glassy membrane: Deformation through the glass transition. *Eur. Phys. J. E*, 40(7), 2017.

[89] Q. Xu, K. E. Jensen, R. Boltyanskiy, R. Sarfati, R. W. Style, and E. R. Dufresne. Direct measurement of strain-dependent solid surface stress. *Nat. Commun.*, 8(1), 2017.

[90] J. Chopin, D. Vella, and A. Boudaoud. The liquid blister test. *Proc. R. Soc. A*, 464(2099):2887–2906, 2008.

[91] D. Takagi and N. J. Balmforth. Peristaltic pumping of viscous fluid in an elastic tube. *J. Fluid Mech.*, 672:196–218, 2011.

[92] E. Cerda and L. Mahadevan. Geometry and physics of wrinkling. *Phys. Rev. Lett.*, 90:074302, 2003.

[93] J. Yin, Z. Cao, C. Li, I. Sheinman, and X. Chen. Stress-driven buckling patterns in spheroidal core/shell structures. *Proc. Natl. Acad. Sci. U.S.A*, 105(49):19132–19135, 2008.

[94] P. J. Hudleston and S. H. Treagus. Information from folds: A review. *J. Struct. Geol.*, 32(12):2042–2071, 2010.

[95] R. Toro. On the possible shapes of the brain. *Evol. Biol.*, 39(4):600–612, 2012.

[96] P. Ball. Engineering shark skin and other solutions. *Nature*, 400(6744):507–509, 1999.

[97] X. Pu, G. Li, and H. Huang. Preparation, anti-biofouling and drag-reduction properties of a biomimetic shark skin surface. *Biol. Open*, 5(4):389–396, 2016.

[98] F. Brau, P. Damman, H. Diamant, and T. A. Witten. Wrinkle to fold transition: influence of the substrate response. *Soft Matter*, 9:8177–8186, 2013.

[99] H. G. Allen. *Analysis and Design of Structural Sandwich Panels*. Pergamon, 1st edition, 1969.

[100] A. Chiche, C. M. Stafford, and J. T. Cabral. Complex micropatterning of periodic structures on elastomeric surfaces. *Soft Matter*, 4(12):2360, 2008.

[101] Y. Liu, M. Pharr, and G. A. Salvatore. Lab-on-skin: A review of flexible and stretchable electronics for wearable health monitoring. *ACS Nano*, 11(10):9614–9635, 2017.

[102] C. M. Stafford, C. Harrison, K. L. Beers, A. Karim, E. J. Amis, M. R. VanLandingham, H.-C. Kim, W. Volksen, R. D. Miller, and E. E. Simonyi. A buckling-based metrology for measuring the elastic moduli of polymeric thin films. *Nat. Mater.*, 3(8):545–550, 2004.

[103] C. M. Stafford, S. Guo, C. Harrison, and M. Y. M. Chiang. Combinatorial and high-throughput measurements of the modulus of thin polymer films. *Rev. Sci. Instrum.*, 76(6):062207, 2005.

[104] C. M. Stafford, B. D. Vogt, C. Harrison, D. Julthongpiput, and R. Hunag. Elastic moduli of ultrathin amorphous polymer films. *Macromolecules*, 38:5095–5099, 2006.

[105] E. P. Chan and A. J. Crosby. Spontaneous formation of stable aligned wrinkling patterns. *Soft Matter*, 2:324–328, 2006.

[106] H. Vandeparre, S. Gabriele, F. Brau, C. Gay, K. K. Parker, and P. Damman. Hierarchical wrinkling patterns. *Soft Matter*, 6(22):5751, 2010.

[107] D. Breid and A. J. Crosby. Effect of stress state on wrinkle morphology. *Soft Matter*, 7(9):4490, 2011.

[108] E. P. Chan, S. Kundu, Q. Lin, and C. M. Stafford. Quantifying the stress relaxation modulus of polymer thin films via thermal wrinkling. *ACS Appl. Mater. Interfaces*, 3(2):331–338, 2011.

[109] J. Y. Chung, A. J. Nolte, and C. M. Stafford. Surface wrinkling: A versatile platform for measuring thin-film properties. *Adv. Mater.*, 23:349–368, 2011.

[110] Y.-C. Chen and A. J. Crosby. High aspect ratio wrinkles via substrate prestretch. *Adv. Mater.*, 26:5626–5631, 2014.

[111] N. Bowden, S. Brittain, A. G. Evans, J. W. Hutchinson, and G. M. Whitesides. Spontaneous formation of ordered structures in thin films of metals supported on an elastomeric polymer. *Nature*, 393(6681):146–149, 1998.

[112] A. L. Volynskii, S. Bazhenov, O. V. Lebedeva, and N. F. Bakeev. Mechanical buckling instability of thin coatings deposited on soft polymer substrates. *J. Mater. Sci.*, 35:547–554, 2000.

[113] K. Efimenko, M. Rackaitis, E. Manias, A. Vaziri, L. Mahadevan, and J. Genzer. Nested self-similar wrinkling patterns in skins. *Nat. Mater.*, 4(4):293–297, 2005.

[114] P.-C. Lin and S. Yang. Spontaneous formation of one-dimensional ripples in transit to highly ordered two-dimensional herringbone structures through sequential and unequal biaxial mechanical stretching. *Appl. Phys. Lett.*, 90(24):241903, 2007.

[115] M. A. Biot. Bending of an infinite beam on an elastic foundation. *J. Appl. Mech.*, (203):1–7, 1937.

[116] Y. Ebata, A. B. Croll, and A. J. Crosby. Wrinkling and strain localizations in polymer thin films. *Soft Matter*, 8:9086–9091, 2012.

[117] E. P. Chan, K. A. Page, S. H. Im, D. L. Patton, R. Huang, and C. M. Stafford. Viscoelastic properties of confined polymer films measured via thermal wrinkling. *Soft Matter*, 5(23):4638, 2009.

[118] B. Li, Y.-P. Cao, X.-Q. Feng, and H. Gao. Mechanics of morphological instabilities and surface wrinkling in soft materials: a review. *Soft Matter*, 8(21):5728, 2012.

[119] Q. Wang and X. Zhao. A three-dimensional phase diagram of growth-induced surface instabilities. *Sci. Rep.*, 5(1):8887, 2015.

[120] L. Pocivavsek, R. Dellsy, S. Johnson, B. Lin, K. Y. C. Lee, and E. Cerda. Stress and fold localization in thin elastic membranes. *Science*, 320:912–916, 2008.

[121] F. Brau, H. Vandeparre, A. Sabbah, C. Poulard, A. Boudaoud, and P. Damman. Multiple-length-scale elastic instability mimics parametric resonance of nonlinear oscillators. *Nat. Phys.*, 7(1):56–60, 2010.

[122] C. Cao, H. F. Chan, J. Zang, K. W. Leong, and X. Zhao. Harnessing localized ridges for high-aspect-ratio hierarchical patterns with dynamic tunability and multifunctionality. *Adv. Mater.*, 26(11):1763–1770, 2014.

[123] D. Vella, J. Bico, A. Boudaoud, B. Roman, and P. M. Reis. The macroscopic delamination of thin films from elastic substrates. *Proc. Natl. Acad. Sci. U.S.A*, 106(27):10901–10906, 2009.

[124] A. J. Nolte, J. Young Chung, C. S. Davis, and C. M. Stafford. Wrinkling-to-delamination transition in thin polymer films on compliant substrates. *Soft Matter*, 13(43):7930–7937, 2017.

[125] S. Wang, J. Song, D.-H. Kim, Y. Huang, and J. A. Rogers. Local versus global buckling of thin films on elastomeric substrates. *Appl. Phys. Lett.*, 93(2):023126, 2008.

[126] Y. Ma, K.-I. Jang, L. Wang, H. N. Jung, J. W. Kwak, Y. Xue, H. Chen, Y. Yang, D. Shi, X. Feng, J. A. Rogers, and Y. Huang. Design of strain-limiting substrate materials for stretchable and flexible electronics. *Adv. Funct. Mater.*, 26(29):5345–5351, 2016.

[127] X. Meng, G. Liu, Z. Wang, and S. Wang. Analytical study of wrinkling in thin-film-on-elastomer system with finite substrate thickness. *Appl. Math. Mech.*, 38(4):469–478, 2017.

[128] D. C. Hyun and U. Jeong. Substrate thickness: An effective control parameter for polymer thin film buckling on PDMS substrates. *J. Appl. Polym. Sci.*, 112(5):2683–2690, 2009.

[129] Y. Ma, Y. Xue, K.-I. Jang, X. Feng, J. A. Rogers, and Y. Huang. Wrinkling of a stiff thin film bonded to a pre-strained, compliant substrate with finite thickness. *Proc. Royal Soc. A*, 472(2192):20160339, 2016.

[130] J. Brandup, E. H. Immergut, and Grulke E. A., editors. *Polymer Handbook*, volume 49. Wiley and Sons, New York, 4th edition, 1999.

[131] R. K. Bay and A. J. Crosby. Uniaxial extension of ultrathin freestanding polymer films. *ACS Macro Lett.*, 8(9):1080–1085, 2019.

[132] J.-C. Ono-dit Biot, M. Trejo, E. Loukiantcheko, M. Lauch, E. Raphaël, K. Dalnoki-Veress, and T. Salez. Hydroelastic wake on a thin elastic sheet floating on water. *Phys. Rev. Fluids*, 4:014808, 2019.

[133] L. E. Scriven. Physics and applications of dip coating and spin coating. *MRS Proc.*, 121:717, 1988.

[134] C. M. Stafford, K. E. Roskov, T. H. Epps, and M. J. Fasolka. Generating thickness gradients of thin polymer films via flow coating. *Rev. Sci. Instrum.*, 77(2):023908, 2006.

[135] D. B. Hall, P. Underhill, and J. M. Torkelson. Spin coating of thin and ultrathin polymer films. *Polym. Eng. Sci.*, 38(12):2039–2045, 1998.

[136] H. G. Tompkins and E. A. Irene. *Handbook of Ellipsometry.* William Andrew Publishing, Norwich, NY, 2005.

[137] O. S. Heavens. Optical properties of thin films. *Rep. Prog. Phys.*, 23(1), 1960.

[138] S. L. Cormier, J. D. McGraw, T. Salez, E. Raphaël, and K. Dalnoki-Veress. Beyond Tanner's law: Crossover between spreading regimes of a viscous droplet on an identical film. *Phys. Rev. Lett.*, 109(15):154501, 2012.

[139] F. J. Giessibl. Advances in atomic force microscopy. *Rev. Mod. Phys.*, 75:949–983, 2003.